Conditions for the existence of backward surface magnetostatic waves in a ferrite–insulator–metal structure

V. I. Zubkov and V. I. Shcheglov

Institute of Radio Engineering and Electronics, Russian Academy of Sciences, Fryazino
(Submitted December 10, 1996; resubmitted March 13, 1998)
Pis'ma Zh. Tekh. Fiz. **24**, 1–7 (July 12, 1998)

A theoretical analysis is made of the dispersion of surface magnetostatic waves (SMSWs) at different frequencies propagating in ferrite–insulator–metal (FIM) structures magnetized by a uniform magnetic field. It is established that depending on the ratio between the thicknesses of the ferrite and insulating layers in FIM structures, backward SMSWs exist in different frequency ranges and have different wave numbers and directions of propagation. The conditions for which backward SMSWs may be observed directly in FIM structures are determined. © *1998 American Institute of Physics.* [S1063-7850(98)00107-4]

Studies of the dispersion of forward and backward surface magnetostatic waves (SMSWs) in ferrite–insulator–metal (FIM) structures are of great interest because of their possible applications for analog processing of information in the microwave range (see Ref. 1 and the literature cited therein). The numerous studies on the dispersion of SMSWs in FIM structures with specific parameters[1–6] create the impression that the problem of the existence of backward SM-SWs in FIM structures has been well studied. However, the absence of direct experimental evidence of their existence[4–6] is incomprehensible. Some possible reasons for this are suggested below.

We shall consider an infinite FIM structure in the yz plane, consisting of a ferrite film of thickness d magnetized to saturation and an ideal conducting metal layer, separated by an insulating layer (in magnetostatics, a vacuum layer) of thickness s (subsequently, this layer is simply denoted by s). The $x=0$ plane is the surface of the ferrite film closest to the metal layer. The magnetizing field H_0 is directed along the z axis. In this FIM structure an SMSW propagates with the frequency ω and wave vector $\mathbf{k}$, whose group velocity $\mathbf{v}_g$ is directed at the angles of φ and ψ to the y axis.

The dispersion relation for the SMSW in the FIM structure is written in the form:[7]

$$[\beta - 2\mu\alpha \coth(\alpha kd)] + (\beta + 2 - 2p\nu \cos \varphi)$$
$$\times \exp(-2ks) = 0, \qquad (1)$$

where $\alpha = [\mu^{-1} \sin^2 \varphi + \cos^2 \varphi]^{1/2}$; $\beta = (\nu^2 - \mu^2 + \mu)\cos^2 \varphi - \mu - 1$; $\mu = 1 + \Omega_H(\Omega_H^2 - \Omega^2)^{-1}$; $\nu = \Omega(\Omega_H^2 - \Omega^2)^{-1}$; $\Omega = \omega(4\pi|\gamma|M_0)^{-1}$; $\Omega_H = H_0(4\pi M_0)^{-1}$; $4\pi M_0$ is the saturation magnetization of the ferrite film, γ is the electron gyromagnetic ratio, and $p = \pm 1$. Only SMSWs propagating in the $x=0$ plane of the FIM structure ($p=1$) can be both forward and backward waves.[1–3]

The dispersion relation (1) is considered to be the dispersion law $\Omega_s(k)$ for given parameters φ, d, s, and Ω_H and is used to determine the type of SMSW (forward or backward).[1–5] The form of the dispersion law $\Omega_s(k)$ depends on the ratio between d and s and does not vary qualitatively

with varying Ω_H, whereas the angle φ is considered to be a free parameter which is defined by the antenna exciting the SMSW ($\varphi = \varphi_0$) (Refs. 1–6). Below we determine the relationship between the frequency range of existence, the wave numbers, and directions of propagation of backward SMSWs, and we show that the type of wave cannot be accurately determined merely using the dispersion law.

It is known[1–3,5] that SMSWs exist in a frequency range between a lower limit Ω_l and an upper limit $\Omega_u(s,\varphi)$ and in a range of angles φ bounded by the "cutoff" angles $\pm \varphi_c(s)$. We then have $\Omega_u(\infty,0) < \Omega_u(s,\varphi) < \Omega_u(0,0)$ and $\varphi_c(s) < \varphi_c(0)$, where $\Omega_u(\infty,0)$ and $\Omega_u(0,0)$ and $\varphi_c(\infty)$ and $\varphi_c(0)$ are the upper frequencies and cutoff angles for a SMSW in the ferrite film ($s=\infty$) and in the ferrite–metal structure ($s=0$):

$$\Omega_l = \sqrt{\Omega_H(\Omega_H + 1)}, \qquad (2)$$

$$\Omega_u(\infty,0) = \Omega_H + 0.5, \qquad (3)$$

$$\varphi_c(\infty) = \arccos\{[\Omega + \sqrt{\Omega^2 - \Omega_H(\Omega_H + 1)}](\Omega_H + 1)^{-1}\}, \qquad (4)$$

$$\Omega_u(0,0) = \Omega_H + 1, \qquad (5)$$

$$\varphi_c(0) = \arccos\sqrt{[\Omega^2 - \Omega_H(\Omega_H + 1)](\Omega_H + 1)^{-1}}. \qquad (6)$$

Figure 1 shows dispersion curves $\Omega_s(k_y, d)$ for a SMSW in an FIM structure with different values of s. It can be seen that there are three types of curves. First, in the frequency range $\Omega_u(\infty,0) < \Omega < \Omega_u(0,0)$ the functions $\Omega_s(k_y d)$ for SMSWs in an FIM structure with small s ($0 < s \lesssim s_{b1}$) have a maximum at $kd = k_{max,s}d$ and tend to $\Omega_u(\infty,0)$ for $kd \rightarrow \infty$ (curves *2* and *3*). Each forward SMSW with $k < k_{max,s}$ corresponds to a backward SMSW with k in $k_{max,s} < k < \infty$. Second, in the frequency range $\Omega_l < \Omega < \Omega_u(\infty,0)$ the function $\Omega_s(k_y d)$ for an SMSW in a FIM structure with large s ($s \gtrsim s_{b1}$) has a maximum and a minimum (curves *4–7*). A backward SMSW exists for $s_{b1} < s < s_{b2}$ and in the frequency range $\delta\Omega(s,0) \ll \Omega_l$. The forward SMSWs have wave numbers k in the ranges $0 < k < k_{max,s}$ and $k_{min,s} < k < \infty$ while the backward SMSWs have wave numbers in the range
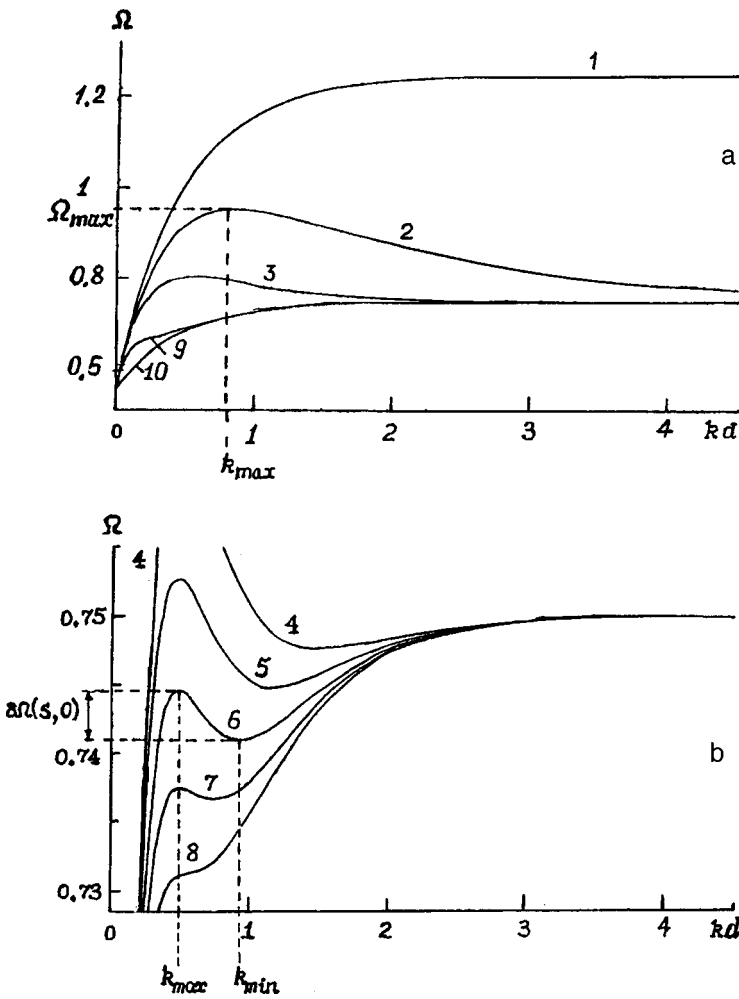
FIG. 1. Dispersion curves $\Omega_s(k_y d)$ for SMSWs in an FIM structure with different s for $\Omega_H = 0.25$ ($s_{b1} \approx \frac{4}{3}d$ and $s_{b2} \approx 2d$). Curves: *1*—$s = 0$; *2*—$s = \frac{1}{3}d$; *3*—$s = d$; *4*—$s = 1.467d$; *5*—$s = 1.6d$; *6*—$s = 1.733d$; *7*—$s = 1.867d$; *8*—$s = 2d$; *9*—$s = 4d$, and *10*—$s = \infty$. For curves *2* and *6* the points $k_{\max,s'}$, $k_{\min,s'}$, $\Omega_u(s,0)$, and $\delta\Omega_s$ are indicated.

$k_{\max,s} < k < k_{\min,s}$ (curves *4–7*). Third, the functions $\Omega_s(k_y d)$ for SMSWs in an FIM structure with $s_{b2} < s < \infty$ have a point of inflection (curve *8*), and only forward SMSWs could exist in such structures.

However, relation (1) defines the dispersion surface $\Omega_s(k_y, k_z)$ (k_y and k_z are the projections of the SMSW wave vector **k** on the *y* and *z* axes) and the dispersion law $\Omega_s(k_y)$ is its intersection with the plane $k_z = 0$ and does not give complete information, which is obtained by additionally studying its intersections with the planes $\Omega_i = \text{const}(k_y 0 k_z)$, i.e., the curves $k_z(k_y)$ (as for an SMSW in a ferrite film[8,9]). Figure 2 gives the curves $k_z(k_y)$ for an SMSW wave with the frequencies $\Omega = 0.608$, 0.695, 0.745, and 0.775 in an FIM structure with different *s*. In the ferrite film and the ferrite–metal structure the curves $k_z(k_y)$ resemble canonical hyperbolas[2,8,9] (curves *1* and *4*). We denote these as $qH(\infty)$ for $s = \infty$ and $qH(0)$ for $s = 0$. The direction of propagation of the SMSWs on the $k_y 0 k_z$ plane is given by a straight line emerging from the origin at the angle φ_0 (subsequently called the line of direction; when discussing Fig. 2 we shall draw this line mentally). For $|\varphi_0| < |\varphi_{c,s}|$ this line intersects $qH(\infty)$ and $qH(0)$ at a single point at which the projection of the group velocity on the direction of the phase velocity shows that the SMSWs in the ferrite film and in the ferrite–metal structure are forward waves. In the FIM structure the line of direction intersects the curves $k_z(k_y)$ at two or three

points. If these are numbered according to increasing k_y, forward SMSWs exist at the first and third points with backward SMSWs at the second.

It can be seen from the curves $k_z(k_y)$ (Fig. 2) that in FIM structures with different *s*, backward SMSWs in different frequency ranges propagate in different ranges of variation of the angle φ and have different wave numbers.

We shall analyze SMSWs in FIM structures with small *s* (the line of direction intersects the $k_z(k_y)$ curves at two points). In the frequency range between $\Omega_u(\infty,0)$ and $\Omega_u(0,0)$ backward SMSWs exist for angles φ between $-\varphi_c(0)$ and $+\varphi_c(0)$, since the curves $k_z(k_y)$ resemble non-canonical ellipses lying at $k_y > 0$ (dotted curve *2*) and the line of direction can only intersect these for $|\varphi_0| < |\varphi_c(0)|$. In the frequency range between Ω_l and $\Omega_u(\infty,0)$ backward SMSWs exist in the range of angles $|\varphi_c(\infty)| < |\varphi_0| < |\varphi_c(0)|$ since the curves $k_z(k_y)$ are strictly increasing functions (solid curves *2* and *3*) situated between $qH(0)$ and $qH(\infty)$, and the line of direction can only intersect them in this range of angles. The curves $k_z(k_y)$ at the point with the lowest value of k_y ($k_{y,\inf,s}$ for $k_z = 0$) are close to $qH(0)$; $k_{y,\inf,s}$ increases with increasing *s*.

We shall now analyze SMSWs in an FIM structure with large *s* (the line of direction intersects the curves $k_z(k_y)$ at three points) where two forward and one backward SMSW exist. In an FIM structure with $s_{b1} < s < s_{b2}$ the curves $k_z(k_y)$
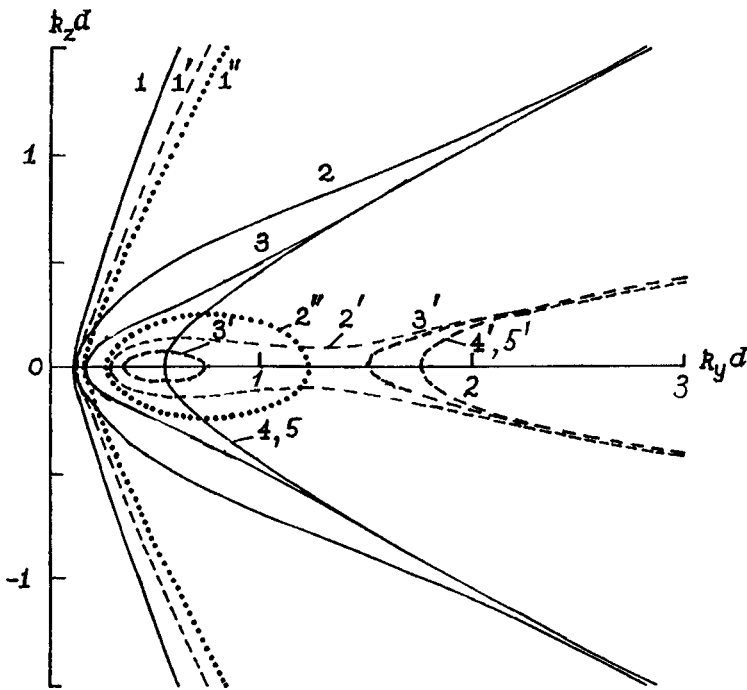
FIG. 2. Curves of $k_z(k_y)$ for SMSWs at frequencies $\Omega = 0.695$ (solid curves), 0.745 (dashed curves), and 0.775 (dotted curves) in an FIM structure with different s for $\Omega_H = 0.25$. Solid and dotted curves: *1—s=0; 2—s=d; 3—s=2d; 4—s=4d; 5—s=∞*. Dashed curves: *1—s=0; 2—s=1.533d; 3—s=$\frac{5}{3}$d; 4—s=4d*. At frequencies $\Omega = 0.695$ and 0.745 curves *5* differ little from curves *4*. At $\Omega = 0.775$ curves *3–5* do not exist.

either consist of two parts, one resembling an ellipse, the other resembling $qH(\infty)$ (dashed curve *3*) or they are continuous curves, having a maximum (for $k_y = k_{y,\max}$) and a minimum (for $k_y = k_{y,\min}$) (dashed curve *2*). We then find $k_{y,\max} < k_{y,\min} < k_{y,\inf,\infty}$ for the curve $qH(\infty)$. A backward SMSW and a second forward SMSW exist for angles φ_0 between $0°$ and $\pm\varphi_c(\infty)$ in the frequency range $\delta\Omega(s,\varphi)$, lying between Ω_l and $\Omega_u(\infty,0)$; for $s \geqslant s_{b1}$ this is around $\Omega_u(\infty,0)$. In an FIM structure with $s_{b2} < s < \infty$ the curves $k_z(k_y)$ are increasing functions exhibiting weakly defined convexity and concavity (curve *3*). A backward SMSW and a second forward SMSW exist in a narrow range of angles $|\varphi_{c0}| < |\varphi_0| < |\varphi_c(\infty)|$, where φ_{c0} is the angle of inclination of the line passing through the origin and the tip of the concavity. Their frequency range of existence $\delta\Omega(s,\varphi)$ lies between Ω_l and $\Omega_u(\infty,0)$ (for $s \to \infty$, around Ω_l).

On analyzing familiar experiments[1,4–6]) concerned exclusively with the study of SMSWs propagating only for $\varphi_0 = 0$, we see that the dispersion curves for the forward SMSWs in an FIM structure show good agreement with the theoretical ones. No backward SMSWs are observed; this is attributed to their high propagation losses (as a result of their low group velocity).

However, the group velocity of backward SMSWs with $\varphi_0 = 0$ is comparable with that of the forward SMSWs (Fig. 1). These backward SMSWs may be observed by using narrow-band converters to excite SMSWs with high wave numbers (Fig. 2) and then the only difficulties involved are measurements for small s, although ways of surmounting

these difficulties are known.[5,6] The group velocity of backward SMSWs with $|\varphi_c(\infty)| < |\varphi_0| < |\varphi_c(0)|$ is in fact lower than that of the forward SMSWs. These backward SMSWs may be observed if $|\varphi_0| \approx |\varphi_c(\infty)|$ holds and narrow-band converters are used.

In our opinion, the only reason backward SMSWs were not observed in Refs. 4 and 5 is because broad-band converters were used. In Ref. 6 backward SMSWs could have been excited but their role was not identified because this was not the purpose of the study.

[1] W. S. Ishak, Proc. IEEE **76**, 171 (1988).

[2] G. A. Vugal'ter, and I. A. Gilinskiĭ, Izv. Vyssh. Uchebn. Zaved. Radiofiz. **32**(10), 1187 (1989).

[3] Yu. I. Bespyatykh, A. V. Vashkovskiĭ, and V. I. Zubkov, Radiotekh. Elektron. **20**, 1003 (1975).

[4] O. S. Esikov, N. A. Toloknov, and Yu. K. Fetisov, Radiotekh. Elektron. **25**, 128 (1980).

[5] A. B. Valyavskiĭ, A. V. Vashkovskiĭ, A. V. Stal'makhov, and V. A. Tyulyukin, Radiotekh. Elektron. **33**, 1820 (1988).

[6] V. I. Zubkov, É. G. Lokk, and V. I. Shcheglov, Radiotekh. Elektron. **34**, 1381 (1989).

[7] A. V. Vashkovskiĭ, V. I. Zubkov, É. G. Lokk, and V. I. Shcheglov, Zh. Tekh. Fiz. **65**(8), 78 (1995) [Tech. Phys. **40**, 790 (1995)].

[8] V. I. Zubkov, É. G. Lokk, and V. I. Shcheglov, Radiotekh. Elektron. **35**, 1617 (1990).

[9] A. V. Vashkovskiĭ, V. I. Zubkov, É. G. Lokk, and V. I. Shcheglov, Radiotekh. Elektron. **40**, 950 (1995).

Translated by R. M. Durham

Films of *a*-Si:H doped with erbium from the metalorganic compound Er(HFA)$_3^*$DME, emitting at 1.54 μm

V. B. Voronkov, V. G. Golubev, N. I. Gorshkov, A. V. Medvedev, A. B. Pevtsov, D. N. Suglobov, and N. A. Feoktistov

A. F. Ioffe Physicotechnical Institute, Russian Academy of Sciences, St. Petersburg;
"V. G. Khlopin Radium Institute" Scientific-Industrial Organization, St. Petersburg
(Submitted December 22, 1997; resubmitted February 12, 1998)
Pis'ma Zh. Tekh. Fiz. **24**, 8–13 (July 12, 1998)

For the first time standard low-temperature (<300 °C) plasma-enhanced chemical vapor deposition technology has been used to obtain *a*-Si(Er):H films emitting at 1.54 μm at room temperature. The fluorine-containing metalorganic compound Er(HFA)$_3^*$DME, exhibiting enhanced volatility and fairly good thermal stability, was used for the first time as the Er source. The establishment of photoconduction in the synthesized samples indicates that they are of satisfactory electronic quality and potentially useful for developing light-emitting diodes at 1.54 μm. © *1998 American Institute of Physics.* [S1063-7850(98)00207-9]

Materials based on erbium-doped silicon are attracting interest primarily because of their potential usefulness for developing silicon optoelectronic devices emitting in the 1.5 μm range which coincides with the range of minimum optical losses in fiber-optic communication lines. Films of erbium-doped amorphous hydrogenated silicon (*a*-Si:H) exhibit an enhanced photoluminescence intensity at 1.54 μm relative to crystalline silicon together with weak thermal quenching.[1,2] Two basic methods are used to introduce Er into *a*-Si:H: 1) ion implantation[3] and 2) magnetron sputtering of a mosaic erbium–silicon or erbium–graphite target in a silane atmosphere.[1,4] In both cases, the synthesized films demonstrated photoluminescence in the 1.54 μm range both at liquid-nitrogen and room temperatures. A disadvantage of this method is the high concentration of intrinsic defects in the films, which hinders their subsequent use for the development of optoelectronics devices. In Refs. 5 and 6 Si(Er) films were synthesized using plasma enhanced chemical vapor deposition (PE CVD), a modified plasma-chemical vapor deposition technology which is usually used to obtain *a*-Si:H films. Erbium was introduced into the film from metalorganic compounds during the PE CVD process at $T = 430$ °C under cyclotron resonance conditions, which ensured epitaxial Si growth. In this case, the photoluminescence at 1.54 μm was recorded at liquid-helium temperatures.

The aim of the present study was to obtain *a*-Si(Er):H films using standard low-temperature (<300 °C) PE CVD technology[7] usually used to produce individual layers and multilayer "device-quality" *a*-Si:H structures for solar cells.

Particular attention was paid to the choice of metalorganic compound used to introduce the Er^{3+} ions into the film in a chemical environment suitable for converting erbium into an optically active center. It has been established[4–6] that O, N, and F impurities help to increase the 1.54 μm emission intensity in erbium-doped silicon. Moreover, a fluoride neighborhood for the erbium leads to smaller lattice distortions compared with an oxygen one.[8] We also note that like hydrogen, fluorine is widely used in amorphous silicon films

as a passivator for broken bonds,[9] which helps to suppress nonradiative recombination centers. In addition, the high electronegativity of fluorine compared with nitrogen and oxygen results in a stronger ligand field surrounding the Er^{3+} ion.

The metalorganic compounds most widely used to introduce rare-earth elements into semiconducting materials are β-diketonate complexes having the composition ML$_3$, where M is a rare-earth metal, L$=$(CH$_3$)$_3$CC(O)CHC(O)C(CH$_3$)$_3$, L$=$(CH$_3$)$_3$CC(O)CHC(O)(C$_3$F$_7$), and so on.[10,11] However, unsolvated β-diketonates of rare-earth elements are coordination-unsaturated compounds inclined to hydrolysis and thermolysis. In order to avoid this, the coordination vacancies must be blocked with suitable auxiliary ligands. Here, erbium was introduced from the complex Er(HFA)$_3^*$DME (Fig. 1), specially synthesized using a technique described in Ref. 12, where HFA$=$CF$_3$C(O)CHC(O)CF$_3$ (hexafluoroacetylacetone) and DME$=$CH$_3$OCH$_2$CH$_2$OCH$_3$ (1.2-dimethoxyethane). The auxiliary ligand in this compound is selected so that it expels coordinated water molecules from the complex which could cause high-temperature hydrolysis and which is also easily eliminated from the complex, without contaminating the growing film with impurity phases. In Ref. 13 the use of such compounds was demonstrated for the chemical vapor deposition of MF$_3$ films (M$=$Nd, Eu, Er). The Er(HFA)$_3^*$DME complex is converted to the gas phase at fairly low temperature (120–140 °C). At temperatures of 320–340 °C the metalorganic compound undergoes gas-phase thermal dissociation with the formation of an ErF$_3$ film.[13]

Amorphous *a*-Si(Er):H films were grown by rf dissociation of an argon–silane mixture in a glow discharge plasma. The parameters of the plasma-chemical process were as follows: silane content in argon, 10%; pressure, 0.1–0.2 Torr; frequency, 17 MHz; rf power, 0.03–0.1 W/cm^2; substrate temperature, 200–250 °C; and gas mixture flux, 5–10 sccm.

The erbium was introduced by sublimation of Er(HFA)$_3^*$DME powder. A 0.1 g weighed portion was placed
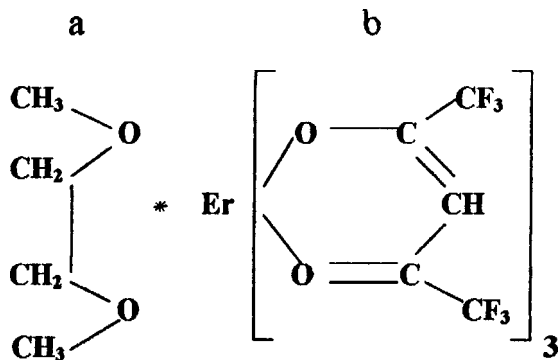
FIG. 1. Er(HFA)$_3^*$DME complex:
a—auxiliary ligand DME=CH$_3$OCH$_2$CH$_2$OCH$_3$;
b—principal ligand HFA=CF$_3$C(O)CHC(O)CF$_3$.

in a stainless steel boat positioned approximately 4 cm from the discharge gap where the substrate with the growing a-Si:H film was placed. The rate of sublimation of the metalorganic compound was varied by heating the boat from 25 to 200°. Fused quartz and crystalline silicon were employed as the substrates. The thickness of the films was determined in situ by laser interferometry and was 2000–3000 Å for different samples. The films were annealed at $T = 300$ °C at normal pressure in a pure nitrogen flux (50 sccm) for 15 min.

The concentration of impurities in the film was determined by SIMS and was 10^{19} cm^{-3} for erbium, 2×10^{20} cm^{-3} for fluorine, and 10^{20} cm^{-3} for oxygen, with a fairly uniform distribution over sample thickness. The conductivity of the films was at most 10^{-10} S cm^{-1} and the photoconductivity was around 10^{-7} S cm^{-1}.

The photoluminescence of the films was measured using an automated KSVU-23 system. The detector was a cooled germanium photodiode. The photoluminescence was excited using the 4880 Å Ar$^+$ laser line at 40 mW.

Photoluminescence spectra at room and liquid-nitrogen temperatures are shown in Fig. 2. At low temperature the spectrum exhibits two bands. The first is a narrow line (full
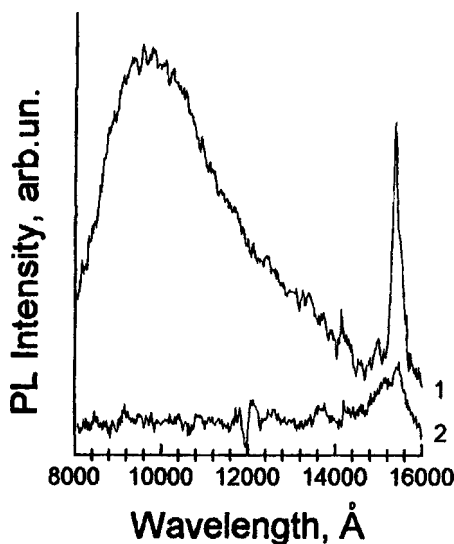
width at half maximum ≈ 7 meV) centered at $\lambda = 1.54$ μm, which is attributed to the $^4I_{13/2} \rightarrow {}^4I_{15/2}$ intracenter transition of the Er^{3+} ion. At room temperature the line shows appreciable broadening in the short-wavelength direction and its intensity drops approximately fourfold. Measurements of the photoluminescence intensity as a function of the excitation power showed that this dependence is linear up to ≈ 200 mW, and then the signal saturates. The second, broad band near 1 μm reflects the well-known ''tail–tail'' transitions in undoped a-Si:H (Ref. 4). However, the elongation of this line in the long-wavelength direction may evidence the presence of an appreciable concentration of oxygen in the samples.[14] As was to be expected, this line undergoes strong thermal quenching caused by a thermally activated transition of nonequilibrium carriers to nonradiative states.

To sum up, standard low-temperature (< 300 °C) PE CVD technology has been used to obtain a-Si(Er):H films emitting in the 1.54 μm range at room temperature. A fluorine-containing metalorganic compound Er(HFA)$_3^*$DME possessing enhanced volatility and fairly good thermal stability was used for the first time as an Er source. This compound had been used previously[13] to obtain films of pure erbium fluoride. The observation of photoconduction in the synthesized samples indicates that they are of satisfactory electronic quality and potentially useful for the development of 1.54 μm light-emitting diodes.

[1] M. S. Bresler, O. V. Gusev, V. Kh. Kudoyarova, A. N. Kuznetsov, P. E. Pak, E. I. Terukov, I. N. Yassievich, B. P. Zakharchenya, W. Fuhs, and A. Sturm, Appl. Phys. Lett. **67**, 3599 (1995).

[2] E. I. Terukov, V. Kh. Kudoyarova, M. M. Mezdrogina, V. G. Golubev, A. Sturm, and W. Fuhs, Fiz. Tekh. Poluprovodn. **30**, 820 (1996) [Semiconductors **30**, 440 (1996)].

[3] J. H. Shin, R. Serna, G. H. van den Hoven, A. Polman, W. G. J. M. van Sark, and A. M. Vredenberg, Appl. Phys. Lett. **68**, 997 (1996).

[4] A. R. Zanatta, L. A. O. Nunes, and L. R. Tessler, Appl. Phys. Lett. **70**, 511 (1997).

[5] J. L. Rogers, P. S. Andry, W. J. Varhue, E. Adams, M. Lavoie, and P. B. Klein, J. Appl. Phys. **78**, 6241 (1995).

[6] P. S. Andry, W. J. Varhue, F. Lapido, K. Ahmed, P. B. Klein, P. Hengenhold, and J. Hunter, J. Appl. Phys. **80**, 551 (1996).

[7] *The Physics of Hydrogenated Amorphous Silicon* (Topics in Applied Physics, Vols. 55–56), edited by J. D. Joannopoulos and G. Lucovsky (Springer-Verlag, Berlin, 1984; Mir, Moscow, 1987), Part 1, p. 363.

[8] W.-X. Ni, K. B. Joelsson, C.-X. Du, I. A. Buyanova, G. Pozina, W. M. Chen, G. V. Hansson, B. Monemar, J. Cardenas, and B. G. Svensson, Appl. Phys. Lett. **70**, 3383 (1997).

[9] A. Madan, in *The Physics of Hydrogenated Amorphous Silicon* (Topics in Applied Physics, Vols. 55–56), edited by J. D. Joannopoulos and G. Lucovsky (Springer-Verlag, Berlin, 1984; Mir, Moscow, 1987), Part 1, p. 310.

[10] M. Morse, B. Zheng, J. Palm, X. Duan, and L. C. Kimerling, Mater. Res. Soc. Symp. Proc. **422**, 41 (1996).

[11] A. J. Kenyon, P. F. Trwoga, M. Federighi, and C. W. Pitt, Mater. Res. Soc. Symp. Proc. **358**, 117 (1995).

[12] N. P. Grebenshchikov, G. V. Sidorenko, and D. N. Suglobov, Radiokhimiya **32**(3), 14 (1990).

[13] N. I. Gorshkov, D. N. Suglobov, and G. V. Sidorenko, Radiokhimiya **37**(3), 196 (1995).

[14] R. Street, Adv. Phys. **30**, 593 (1981).

Translated by R. M. Durham

FIG. 2. Photoluminescence spectra of a-Si(Er):H films at liquid-nitrogen (*1*) and room (*2*) temperatures.

Formation of a cathode crater in a low-voltage cold-cathode vacuum arc

M. K. Marakhtanov and A. M. Marakhtanov

N. E. Bauman State Technical University, Moscow
(Submitted October 7, 1997)
Pis'ma Zh. Tekh. Fiz. **24**, 14–19 (July 12, 1998)

The cathode crater in a low-voltage cold-cathode vacuum arc is planar. The area of the crater and the density of the current flowing through it depend on the thermal and electrical properties of the cathode metal. © *1998 American Institute of Physics.* [S1063-7850(98)00307-3]

Experiments were carried out to establish the dimensions and shape of the craters left by a low-voltage cold-cathode vacuum arc. The density of the current flowing through the crater was determined for Zn, Al, Cu, Fe, Ti, and Cr cathodes at voltages of 16.7–36 V and arc currents of 42–121 A, depending on the material. The experiments were carried out using the Bulat-6 industrial vacuum-arc evaporation system at an argon pressure of 0.04 Pa in the vacuum chamber. The cathodes were in the shape of truncated cones with base diameters of 56 and 60 mm and a height of 40 mm. The arc burns on the surface of the smaller base, over which the cathode spot moves causing cathode sputtering. The opposite base was water-cooled and the inner wall of the vacuum chamber served as the anode.

The entire sputtered surface of the spent cathode was covered with craters. The outline of the crater was bounded by folds of solidified metal. Two groups of craters whose sizes differ by a factor of ten are clearly distinguishable. The large cathode craters *1* are distributed fairly sparsely while the small cathode craters *2* completely cover the sputtered surface (Fig. 1). For the measurements we used a NEOPHOT 21 microscope, Carl Zeiss, Jena (crater depth and $\times 180$ photographs), an MIM-7 metallurgical microscope (depth and diameter of craters), and an MBS-9 laboratory microscope (diameter and distance between craters). Each dimension quoted here is the average of 25–50 measurements.

The diameter D of the cathode crater is assumed to be $0.5(D_{max}+D_{min})$. The crater depth h was determined by focusing the microscope objective first onto the tips of the folds bounding the crater (Fig. 1a) and then onto the crater floor (Fig. 1b). The crater depth was taken to be the difference between the readings of the micrometer used to move the objective. The accuracy of the measurements of h is ± 0.0025 mm. The true crater depth is less than h because the latter was measured from the tips of the folds, which protrude above the surface of the cathode. The average crater dimensions were $D = 0.498$, 0.264, 0.173, 0.183, 0.169, and 0.087 mm and $h = 0.043$, 0.017, 0.0185, 0.0157, 0.0082, and 0.0059 mm for Zn, Al, Cu, Fe, Ti, and Cr cathodes, respectively. The average cathode crater is planar since the ratio $h/D = 0.048 - 0.107$ is obtained for these metals.

It was previously established[1] that an arc moves over the cathode by replacing old craters with new ones, the average crater lifetime being finite at $T = 10^{-6} - 10^{-3}$ s. It is also known[2] that the entire arc current flows through the crater of

the cathode spot. The quantity of metal removed by the arc depends on the electric charge passing through the crater. Thus, the volume of a planar crater should increase over time T, mainly as a result of an increase in its area $\sim D^2$. We measure the diameter D left by the arc at the end of the
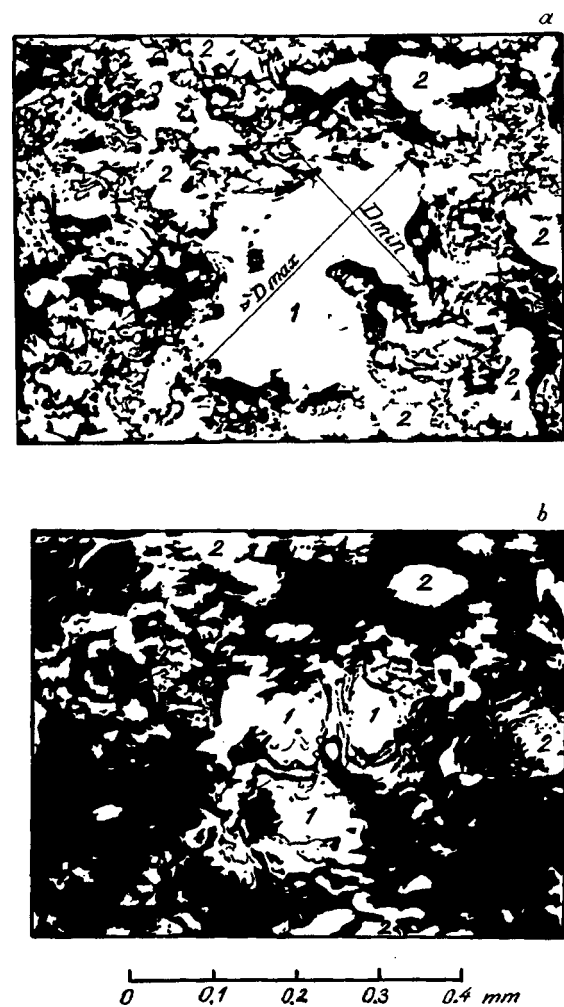

FIG. 1. Photomicrographs of the surface of an aluminum cathode, arc voltage 36 V, arc current 52 A; *1*—cathode crater, *2*—small cathode crater; objective focused onto the tips of the metal folds surrounding the crater *1* (a); objective focused onto the bottom of the cathode crater *1* (b); the black spots on the photographs correspond to protrusions at the cathode surface or its unfocused image; the white spots correspond to indentations or the bottom of the crater and small craters.
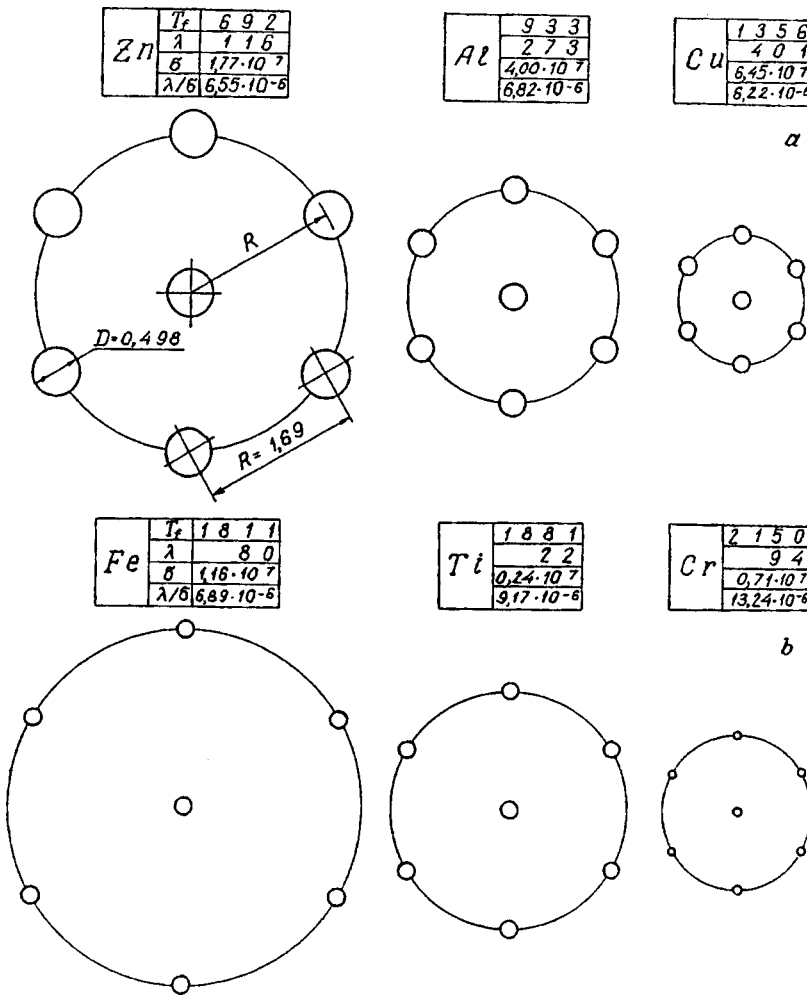
FIG. 2. Diagram of ''switching-thermal circle'' for cold metal cathodes: with high thermal conductivity $\lambda > 100$ (a) and low thermal conductivity, $\lambda < 100$ (b); the diameter D of the cathode crater and the distance R between neighboring craters vary, obeying an explicit dependence related to the thermal and electrical characteristics of the metal cathode.

period T. Thus, the ratio $j = I/D^2$ is equal to the minimum current density in the cathode crater if we neglect any variation of the arc current I with time.

The current density j for which a crater can still exist is 0.19×10^9, 0.75×10^9, 3.51×10^9, 3.61×10^9, 3.33×10^9, and 12.29×10^9 A/m^2, for Zn, Al, Cu, Fe, Ti, and Cr, respectively. These values agree with the current densities of 3.4×10^9, 3.2×10^9, and 1.5×10^9 A/cm^2, which were observed in experiments using Ag, Cu, and Mo exploding wires, respectively.[3]

The maximum temperature of the cathode crater barely exceeds the boiling point T_b of the metal. Assuming that the current density of the thermionic emission from a boiling crater is $j_e = 1.2 \times 10^6 T_b^2 \exp\{-e\varphi/kT_b\}$, then we have $j_e = 1.3 \times 10^{-6}$ A/m^2 for a Zn cathode and $j_e = 3.9 \times 10^7$ A/m^2 for a Ti cathode. Here Zn has the boiling point $T_b = 1179$ K and work function $\varphi = 4.24$ V, while Ti has $T_b = 3560$ K and $\varphi = 3.95$ V. Given the obvious inequality $j_e \ll j$, the contribution of the thermionic emission from the cathode to the arc current can be neglected for all these metals.

The average distance between the craters is $R = 1.69$, 1.13, 0.69, 1.90, 1.27, and 0.84 mm for Zn, Al, Cu, Fe, Ti, and Cr, respectively. The ratio of this distance to the crater diameter is $R/D = 3.4$–10.4 for Zn–Fe, respectively. If the craters are positioned arbitrarily, separated by the same distance R, we obtain a ''switching-thermal circle'' system (Fig. 2). Here the cathode craters are shown as small circles of diameter D. We assume that after the arc has been quenched at the hot point of a disappearing crater, it enters the switching part of the period T. During the switching time, the arc systematically reappears and is quenched in several small cathode craters whose position gradually moves from the hot point of the disappearing crater to the cold boundary of the circle R. Here, at the cold surface of the cathode, the crater again acquires the normal size D.

The displacement of the crater over the cathode is caused by the thermal and electrical properties of the cathode. For Zn, Al, and Cu for which $\lambda > 100$ W·m^{-1}·K^{-1}, the dimensions D and R decrease as the cathode melting point T_f, K and the thermal conductivity λ increase (Fig. 2a). For Fe, Ti, and Cr we find $\lambda < 100$, and the dimensions D and R decrease as the ratio of the thermal and electrical conductivities λ/σ, W·Ω·K^{-1}, increases (Fig. 2b).

Almost the entire mass of the cathode may flow into the arc via a few large cathode craters. For example, the average crater on Ti has the mass $M = \rho \cdot D^2 \cdot h = 4540 \times (0.169 \times 10^{-3})^2 \times 0.0082 \times 10^{-3} = 0.11 \times 10^{-8}$ kg, where $\rho = 4540$ kg/m^3 is the Ti density. The average rate of sputtering of titanium in the arc was determined as $S = 4.42$

$\times 10^{-6}$ kg/s. If the rate S is constant in time, the mass M leaves the average crater in the time $t = M/S = 2.5 \times 10^{-4}$ s, which is approximately equal to the crater lifetime T (see above).

The physical quantities used were taken from Ref. 3.

To sum up, in a low-voltage cold-cathode vacuum arc the cathode crater has a planar profile with $h/D \lesssim 0.1$. The crater disappears when the density of the current flowing through its cross section is $(0.2-12) \times 10^{9}$ A/m^2 (Zn–Cr). The average crater diameter and the average distance between neighboring craters depend on the melting point, and also on the thermal and electrical conductivities of the cathode metal.

[1] I. G. Kesaev, *Cathode Processes in an Electric Arc* [in Russian], Nauka, Moscow, p. 6, 144.

[2] F. H. Webb, H. H. Hilton, P. H. Levine, and A. V. Tollestrup, *Exploding Wires*, Vol. 2, edited by W. G. Chace and H. K. Moore (Plenum Press, New York, 1962), p. 37–77.

[3] A. P. Babichev, N. A. Babushkina, A. M. Bratkovskiĭ *et al.*, in *Handbook of Physical Quantities*, edited by I. S. Grigor'ev and E. Z. Meĭlikhova [in Russian], Énergoatomizdat, Moscow (1991), 1232 pp.

Translated by R. M. Durham

Spontaneous formation of arrays of three-dimensional islands in epitaxial layers

V. G. Dubrovskiĭ, G. É. Cirlin, D. A. Bauman, V. V. Kozachek, and V. V. Mareev

Institute for Analytical Instrumentation, Russian Academy of Sciences, St. Petersburg;
Institute of High-Performance Computations and Databases, St. Petersburg
(Submitted December 19, 1997)

An analysis is made of a theoretical model of the formation of three-dimensional nanometer-size islands in molecular beam epitaxy. The kinetics of the self-organization processes are described using a lattice gas model of the adsorbate with self-consistent allowance for lateral interactions in the activation energies of the diffusion processes. It is shown that at below-critical temperatures in a certain range of thicknesses, decay of the spatially uniform state gives rise to arrays of three-dimensional nano-islands which do not participate in the coalescence process after growth has ceased. The average size of the islands, their geometric profile, and the spatial ordering depend strongly on the kinetic parameters of the model. © *1998 American Institute of Physics.* [S1063-7850(98)00407-8]

Studies of nanostructure formation processes in molecular beam epitaxy (MBE) and its modifications are of considerable interest from the fundamental viewpoint as well as for practical applications in microelectronics and optoelectronics.[1] One of the most promising methods of obtaining nanostructures is their direct formation as a result of surface self-organization effects in MBE growth. Requiring no pretreatment or aftergrowth surface treatment, this method can produce systems of three-dimensional, dislocation-free, nanometer-size islands (quantum dots) at a high surface density.[2] With a suitable choice of growth conditions, a reduction in the spread of island sizes as well as their spatial ordering are observed experimentally.[3] Despite the considerable success achieved in the equilibrium theory of nanostructure formation in heteroepitaxial systems,[4,5] Monte Carlo simulation,[6,7] and continuum models of diffusion instabilities in MBE,[6] the kinetic theory of self-organization effects in MBE has not been adequately developed. In particular, very few microscopic models are available to examine the relationship between the growth kinetics and the surface morphology, or the temperature dependence of the characteristics of these nanostructures.

Here we attempt to construct such a model by generalizing the model of the dynamics of a nonideal three-dimensional adsorbate.[8] The proposed model is used to make a numerical analysis of self-organization effects in an epitaxial layer, which result in the formation of ordered arrays of three-dimensional nano-islands.

The lattice gas model is used to describe the growth kinetics. The occupation numbers of the site $(l,\mathbf{R})$ in layer l with the discrete coordinate $\mathbf{R}$ in the substrate plane $n_l(\mathbf{R})$ are 0 or 1. The occupation number averaged over all microscopic states at time t gives the probability of observing an adatom at the site $(l,\mathbf{R})$ $\theta_l(\mathbf{R},t)=\langle n_l(\mathbf{R})\rangle_t$. The statistically averaged probability that the local height of the surface at point $\mathbf{R}$ is l monolayers at time t is given by

$$p_0(\mathbf{R},t)=\frac{1-\theta_1(\mathbf{R},t)}{1+\Sigma_{l=2}^{\infty}\theta_l(\mathbf{R},t)}, \tag{1}$$

$$p_l(\mathbf{R},t)=\frac{\theta_t(\mathbf{R},t)}{1+\Sigma_{l=2}^{\infty}\theta_l(\mathbf{R},t)}, \quad l\geq 1. \tag{2}$$

The three-dimensional surface of the epitaxial film is described by the function

$$h(\mathbf{R},t)=\sum_{l=0}^{\infty} lp_t(\mathbf{R},t). \tag{3}$$

The system of nonlinear rate equations proposed in Ref. 8 for $\theta_t(\mathbf{R},t)$ has the general form

$$\frac{\partial \theta_l(\mathbf{R},t)}{\partial t}=AD+M+P, \tag{4}$$

where the operators AD, M, and P describe adsorption–desorption processes, two-dimensional diffusion within layer l, and interlayer transitions in the three-dimensional lattice. We subsequently use the following explicit representations of the kinetic operators to make self-consistent allowance for the interaction between lattice gas particles

$$AD=\alpha_l J\sigma(1-\theta_l)\theta_{l-1}-\frac{\theta_l}{t_l^{\alpha}}\exp(-\phi_l^{\alpha}\theta_l), \tag{5}$$

$$M=\frac{1}{zt_l^D}\sum_{\mathbf{R'}}(\theta_l'\exp(-\phi_l^D\theta_l')(1-\theta_l)\theta_{l-1}-\theta_l$$
$$\times\exp(-\phi_l^D\theta_l)(1-\theta_l')\theta_{l-1}'), \tag{6}$$

$$P=\sum_{\mathbf{R'}}\left[\left(\frac{\theta_{l-1}'}{t_{l-1,l}}\exp(-\phi_{l-1}^P\theta_{l-1}')+\frac{\theta_{l+1}'}{t_{l+1,l}}\right.\right.$$
$$\times\exp(-\phi_{l+1}^P\theta_{l+1}')\bigg)(1-\theta_l)\theta_{l-1}-\theta_l$$
$$\times\exp(-\phi_l^P\theta_l)\left(\frac{(1-\theta_{l-1}')\theta_{l-2}'}{t_{l,l-1}}+\frac{(1-\theta_{l+1}')\theta_l'}{t_{l,l+1}}\right)\bigg], \tag{7}$$

where $\theta_l' \equiv \theta_l(\mathbf{R}')$, $\theta_l \equiv \theta_l(\mathbf{R})$, the time dependence is omitted to simplify the notation, and $\theta \equiv 1$ and $t_{0,1} = \infty$ in the absence of particle exchange between the epitaxial layer and the substrate. Summation is performed over all nearest neighbors in the two-dimensional lattice. In Eqs. (5)–(7) J is the particle flux density to the surface, σ is the area of the adsorption cell, α_l is the coefficient of adsorption at the surface of the $l-1$ layer, t_l^a, t_l^D, $t_{l-1,l}$ and $t_{l,l-1}$ are the characteristic lifetimes of an absorbed particle in layer l, diffusion in layer l, $l-1 \rightarrow l$ (upward "jumping") and $l \rightarrow l-1$ (downward "sliding") interlayer transitions for zero coating, and z is the coordination number of the two-dimensional lattice. The binding energies ϕ_l^a, ϕ_l^D, and ϕ_l^P expressed in units of $k_B T$ in self-consistent form allow for the influence of lateral interactions at desorption activation barriers, two-dimensional intralayer hopping diffusion, and interlayer transitions.[8,9] The Langmuir factors $(1 - \theta_l(\mathbf{R}))\theta_{l-1}(\mathbf{R})$ imply vacancy forbiddenness and overhanging layers, which is a normal assumption in the theory of MBE growth.[7] Expressions (5)–(7) are given for a homogeneous planar substrate.

A numerical analysis was made for a cubic mesh assuming a fixed quantity of material at the surface $AD = 0$, i.e., after the end of growth in the absence of desorption ($J = 0$, $t_l^a = \infty$). An analysis was made of the case of heteroepitaxy where the kinetic constants and interaction parameters were assumed to be the same in all layers from $l = 2$: $t_1^D \neq t_2^D = t_3^D = \ldots \equiv t_*^D$; $t_{12} \neq t_{21} = t_{23} = t_{32} = \ldots \equiv t_*^{\uparrow\downarrow}$; $\phi_1^P \neq \phi_2^P = \phi_3^P = \ldots \equiv \phi_*^P$; $\phi_1^D \neq \phi_2^D = \phi_3^D = \ldots \equiv \phi_*^D$. The initial state $\theta_l(0)$ with uniformly filled layers and thickness $\bar{h}(0)$, constant over the surface of the substrate and equal to the quantity of deposited material in one monolayer, was perturbed by a biperiodic perturbation given by

$$\theta_l(x,y,t=0) = \theta_l(0) + \gamma \min(1 - \theta_l(0), \theta_l(0))$$
$$\times \sin\left(\omega_x \frac{2\pi x}{L}\right)\sin\left(\omega_y \frac{2\pi y}{L}\right). \qquad (8)$$

The lattice period L in the plane of the substrate, the value of $\theta_l(0)$, and the perturbation amplitude γ were varied. The perturbation frequencies $\omega_x = \omega_y$ for given L were taken to be equal to the critical frequency at which the ground state with $\bar{h}(0) = $ const becomes unstable in the linear approximation at below-critical temperature ($\phi_*^D > 4$) (Refs. 8 and 9). The instability of the spatially periodic solution is caused by anomalous diffusion in the spinoidal region[10] where particle attraction predominates over the usual diffusion because the diffusion flux is directed along the density gradient of the lattice gas. Under these assumptions, the system of equations (4)–(7) for $\theta_l(\mathbf{R},t)$ was integrated numerically at each time step with periodic boundary conditions. Formulas (1)–(3) were then used to calculate the evolution of the surface morphology.

The results of the calculations show that for $\phi_*^D \geqslant 4.5$, regardless of the value of ϕ_*^P, the time ratio $t_*^{\uparrow\downarrow}/t_*^D$, and the parameters of the first layer in the range of thickness between 2 and 4 ML, the application of a weak critical-frequency perturbation causes the epitaxial layer to decay into a system of three-dimensional nano-islands. In this case, the geometry of the islands, their distribution over the surface of the substrate, and the spatial ordering depend strongly on the critical parameters. By varying the characteristics t_1^D, t_{12}, ϕ_1^D, and ϕ_1^P, we can model the formation of arrays of islands by the Volmer–Weber mechanism and by the Stranski–Krastanow
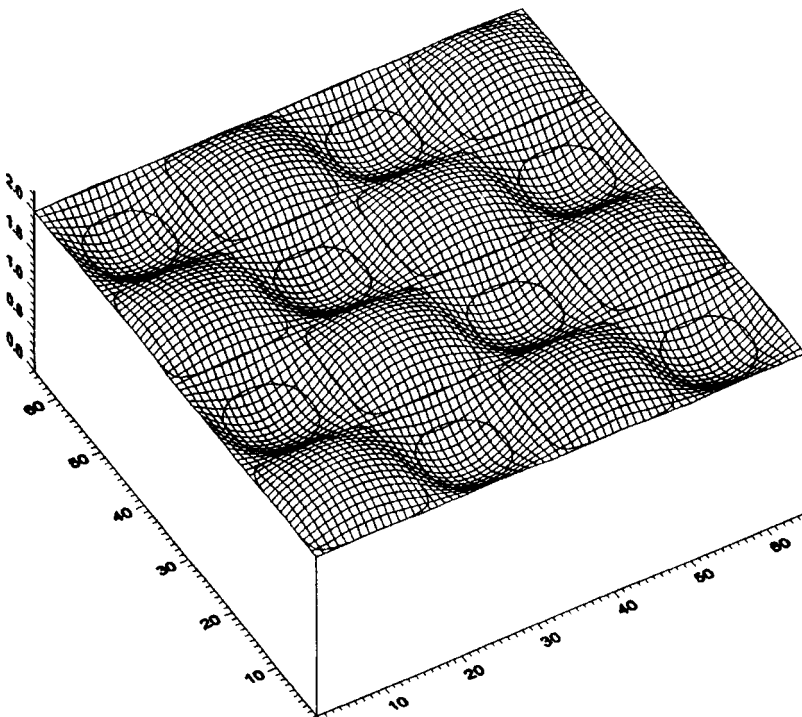

FIG. 1. Surface morphology with an average thickness of 2 ML, $\phi_*^D = 5$, $\phi_*^P = 3$, $t_*^{\uparrow\downarrow}/t_*^D = 800$, and time $t = 0.5 t_*^{\uparrow\downarrow}$. The numbers on the axes are in nanometers.
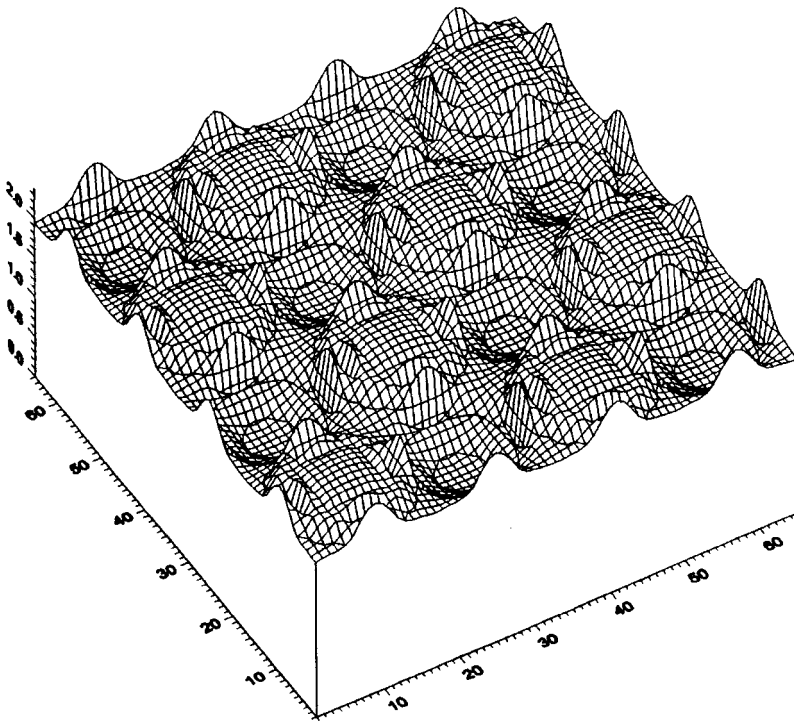
FIG. 2. As in Fig. 1 for $t = 2t_*^{\uparrow\downarrow}$ (quasi-steady-state surface structure).

mechanism.[3,5] Figures 1 and 2 show typical dynamic patterns of the formation of three-dimensional islands with the average thickness $\bar{h}(0) = 2$ ML. At the initial stage of decay, the surface morphology resembles nonlinear density oscillations. This is superseded by the formation of islands with clearly defined boundaries. The surface structure shown in Fig. 2 is stable for times exceeding its characteristic formation time in order of magnitude. Thus, we can talk of the formation of an ensemble of islands which do not take part in the coalescence process for a long time.[5] It should be noted that as the temperature increases ($4 \leqslant \phi_*^D \leqslant 4.5$) no islands with clearly defined boundaries are formed. A spatially ordered structure clearly does not form at above-critical temperatures ($\phi_*^D < 4$).

To sum up, the proposed model can in principle describe the dynamics of surface transformation for a fixed quantity of deposited material. The results show that in many cases, the influence of lateral interactions on the activation energy of elementary diffusion processes at the surface can give rise to stable arrays of three-dimensional nano-islands. The kinetics of the diffusion processes and the interaction constants strongly influence the surface morphology. However, the theory must be generalized to describe surface self-organization effects directly during the MBE growth process, to allow for adsorption and desorption, a two-component flux, and also to make systematic allowance for the lattice mismatch in the microscopic growth model.

[1] Y. Arakava and A. Yariv, IEEE J. Quantum Electron. **QE-22**, 1887 (1986).

[2] P. M. Petroff and G. Medeiros-Ribeiro, Mater. Res. Bull. **21**, 50 (1996).

[3] G. E. Cirlin, V. N. Petrov, A. O. Golubok, S. Ya. Tipissev, V. G. Dubrovskii, N. N. Ledentsov, and D. Bimberg, Surf. Sci. **377–379**, 895 (1997).

[4] J. Tersoff and R. M. Tromp, Phys. Rev. Lett. **70**, 2782 (1993).

[5] V. A. Shchukin, N. N. Ledentsov, P. S. Kop'ev, and D. Bimberg, Phys. Rev. Lett. **75**, 2968 (1995).

[6] M. Rost, P. Smilauer, and J. Krug, Surf. Sci. **369**, 393 (1996).

[7] A. L. Barabasi, Appl. Phys. Lett. **70**, 2565 (1997).

[8] G. V. Dubrovskiĭ, and V. V. Kozachek, Zh. Tekh. Fiz. **65**(4), 124 (1995) [Tech. Phys. **40**, 359 (1995)].

[9] V. G. Dubrovskii, G. E. Cirlin, D. A. Bauman, V. V. Kozachek, and V. V. Mareev, Vacuum, *in press*.

[10] S. A. Kukushkin and A. V. Osipov, Prog. Surf. Sci. **51**, 1 (1996).

Translated by R. M. Durham

Energy dissipation of mechanical oscillators induced by an electric field applied to the surface of an oscillating body

N. A. Vishnyakova, M. L. Gorodetskiĭ, V. P. Mitrofanov, and K. V. Tokmakov

M. V. Lomonosov State University, Moscow
(Submitted April 16, 1997; resubmitted December 22, 1997)
Pis'ma Zh. Tekh. Fiz. **24**, 27–33 (July 12, 1998)

Various factors influencing the damping of the torsional oscillations of a pendulum are discussed. Damping caused by dissipative surface diffusion processes or charge transfer of surface states is considered to be the most probable. © *1998 American Institute of Physics.*
[S1063-7850(98)00507-2]

The development of antennas to record gravitational radiation from cosmic sources has stimulated the fabrication of pendulum-type high-Q mechanical oscillators. It has been noted in various experimental studies that one of the sources of dissipation limiting the Q-factor of these systems is the action of external electric fields on the oscillating body.[1,2] The aim of the present paper is to study the damping of the mechanical oscillations of an oscillator when an electric field is created between the conducting surface of the oscillating body and the surface of a special electrode.

Most of the experiments were carried out using the pendulum shown schematically in Fig. 1. An aluminum disk 6 cm in diameter and weighing around 100 g was suspended by means of three 100 μm diameter tungsten wires. The resonant frequency of the torsional oscillations of this pendulum was around 1 Hz. The lower surface of the disk had radial protrusions at 2 mm intervals. An electric field was generated between the body of the pendulum and an electrode positioned beneath the disk, parallel to it. The electrodes were planar disks made of aluminum, brass, and silicon. The gap between the electrode and the pendulum could be varied between 0.2 and 2 mm. Torsional oscillations of the pendulum were excited by a resonant force generated by applying a periodic electric voltage to the auxiliary electrode and were recorded using a capacitive detector. The insertion losses were determined as the difference between the reciprocal Q factor of the pendulum oscillations measured with and without the electric field. The measurements were made in a special chamber in which either a controlled atmosphere or a vacuum was created.

The design of the pendulum and the electrode used to generate the field was dictated by the need to create a high electric field strength in the gap, without introducing any appreciable extra rigidity in the oscillatory system. This eliminated any dissipation of the pendulum mechanical energy as a result of Joule losses to the resistance in the voltage supply circuit, induced by an electric current flowing in this circuit as a result of a change in the capacitance between the field-generating electrode and the oscillating body. It also eliminated any dissipation as a result of coupling between the oscillator and the electrode, induced by the electric field.[2]

When an electric voltage was applied between the body of the pendulum and the lower electrode, the oscillations exhibited increased damping. This effect occurred when the pendulum was situated in vacuum and in a room atmosphere. In the second case, the damping was appreciably stronger. We stress that these are not losses caused by gas friction since the difference between the losses with and without the field was determined. Figure 2a gives the insertion losses Q_e^{-1} as a function of the voltage U applied between the body of the pendulum and the lower electrode, separated by a gap of 0.5 mm. The lower electrode was made of p-type silicon with a resistivity of 20 $\Omega \cdot$cm. The curves were obtained for different gas environments. Curve *1* was plotted using the results of measurements made in a dry nitrogen atmosphere. Within measurement error, this agrees with the similar dependence measured in vacuum at a pressure of 10^{-2} Torr. Curve *2* was obtained in a nitrogen atmosphere with a small quantity of water vapor while curve *3* was obtained in a room atmosphere with around 70% relative humidity. The hysteresis clearly observed in the moist atmosphere showed up less clearly in vacuum. Note that the character and magnitude of the effect did not depend on the polarity of the applied voltage. It is also interesting to note that if an ac electric field with a frequency of 300 Hz or higher was applied between the pendulum and the lower plate, no additional damping was observed within measurement error. It was also established that the introduced damping does not remain constant after the electric field is switched off. The nature of this change also depended on the state of the ambient atmosphere. Similar effects were observed for aluminum or brass lower electrodes. In this case, the effect also increased strongly with increasing atmospheric humidity, but this increase was between three and five times less than that for the silicon electrode under similar conditions.

Figure 2b gives the insertion losses Q_e^{-1} caused by the electric field as a function of the applied voltage when the conducting coating of the pendulum and the electrode were made of aluminum. The gap between the pendulum and the electrode was 2 mm. The pendulum was suspended by quartz threads and thus had a high intrinsic Q factor in the absence of an electric field.[1] The measurements were made in vacuum at a pressure of 10^{-4} Torr. The experimental depen-
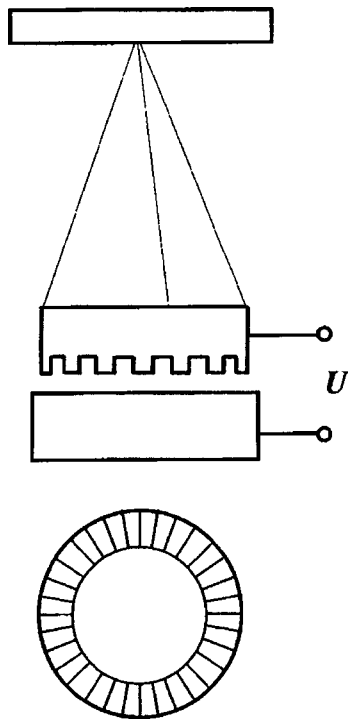
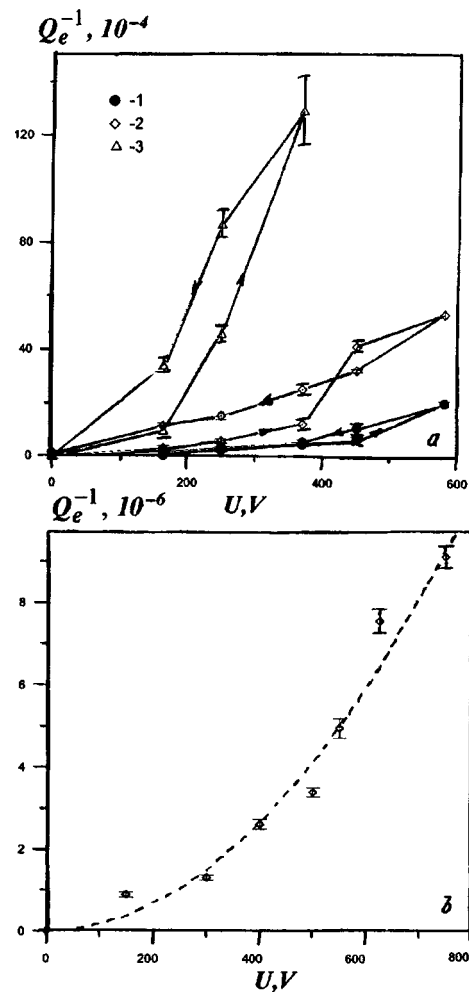FIG. 1. Schematic of pendulum and circuit used to apply the electric field.

FIG. 2. Electric-field-induced losses versus voltage applied between pendulum and electrode: a—when the electrode plate is made of silicon. The measurements were made for various compositions of the ambient gas: *1*—dry nitrogen, *2*—nitrogen containing a small amount of water vapor, *3*—air with $\approx 70\%$ humidity; b—for an aluminum-coated pendulum and electrode at a pressure of $\approx 10^{-4}$ Torr.

dence was accurately approximated by a quadratic function (shown by the dashed curve in Fig. 2b).

Another interesting effect deserves attention. In the experiments carried out at atmospheric pressure, additional damping of the pendulum was also observed in the absence of an external electric field, for example, if the field was applied for some time and then switched off or when the humidity of the ambient atmosphere changed drastically,

In general, the damping observed for these pendulums on application of an electric field can be attributed to various factors. For instance, the ponderomotive force acting on the pendulum alters the tension in the suspension wires. However, our experimental investigations showed that any change in the tension of the suspension wires in the absence of a field barely influences the Q factor of the pendulum. The absence of electric discharges in the interelectrode gap, which could also introduce additional losses in the pendulum oscillations, was monitored by measuring the noise in the voltage supply circuit. Discharges were accompanied by excess noise. The oscillations of the pendulum in an electric field are accompanied by induced currents on the lower electrode and the adjacent conducting surfaces. The damping caused by these induced currents depends on the bulk resistivity of the materials. Calculations showed that for these materials (silicon, aluminum, and brass) this damping is much less than that observed in these experiments. In addition, these processes should also be observed when an ac voltage is applied between the pendulum and the electrode, but in this case no additional damping of the pendulum oscillations was observed.

An analysis of these results suggests that the dissipation introduced into the mechanical oscillator by an electric field depends on the state of the surfaces of the oscillating body and the electrode between which the field is applied. It is known that the electrophysical state of the surface is determined to a considerable extent by the composition of the surrounding atmosphere and may vary substantially as a result of the adsorption of water molecules, for example.[3] It may be supposed that a possible mechanism for dissipation of the oscillator energy is surface diffusion of adsorbed atoms caused by spatial variation of the electric field. In particular, water molecules, having a high static dipole moment, can migrate under the action of a field gradient. In measurements of the electric-field-induced damping of the pendulum oscillations made in vacuum, diffusion processes at the surface make a smaller contribution to the dissipation. In this case, however, another loss mechanism may be observed as a result of the presence of localized surface states. The electric field applied to the surface varies under the pendulum oscillations, causing carriers to be transferred from the bulk to surface states and back, or from some surface states to others.

Depending on the magnitude of the applied voltage, the

thickness of the oxide layer, and the composition of the ambient gas atmosphere, charge may be transferred to surface states under the action of the electric field by different mechanisms: diffusion, tunneling, and hopping. The important thing is that all these processes are dissipative in these systems and are caused by oscillations of a body and are thus accompanied by scattering of the oscillator elastic energy. Note that surface diffusion processes are observed when the surfaces are examined with a scanning tunneling microscope where a strong electric field is created between the tip and the surface.[4] One of the quantities characterizing these surface processes is their relaxation time, which depends on the surface structure. For processes associated with slow surface states the relaxation time may be between tenths of a second and minutes.[5] When the electric field varies with a frequency around 1 Hz, which corresponds to the oscillation frequency of the pendulum, the surface states undergo relaxation. When the external electric field varies at higher frequencies, the carriers do not have time to be transferred to other surface states and thus the dissipation caused by these processes decreases. This can explain the absence of any mechanical reaction of the pendulum to an rf field. We can merely postulate that the change in the pendulum Q factor observed after switching off the external field is associated with the electric fields formed during adsorption but this loss mechanism remains unclear. Studies of the energy dissipation of mechanical oscillations induced by an electric field may provide additional information on the surface properties of a solid.

[1] V. B. Braginsky, V. P. Mitrofanov, and K. V. Tokmakov, Phys. Lett. A **218**, 164 (1996).
[2] V. B. Braginskiĭ, V. P. Mitrofanov, and V. I. Panov, *Low-Dissipation Systems* [in Russian], Nauka, Moscow (1981), 144 pp.
[3] F. F. Vol'kenshteĭn, *Electronic Processes at the Surface of Semiconductors in Chemisorption*, [in Russian], Nauka, Moscow (1987), 432 pp.
[4] J. Mendez, J. Gommez-Herrero, J. I. Pascual *et al.*, J. Vac. Sci. Technol. A **2**, 1145 (1996).
[5] V. F. Kiselev and O. V. Krylov, *Electronic Effects in Adsorption and Catalysis at Semiconductors and Insulators* [in Russian], Nauka, Moscow (1979), 236 pp.

Translated by R. M. Durham

Impact excitation of squeezed vibrational packets in molecules

A. V. Belousov, V. A. Kovarskiĭ, and O. B. Prepelitsa

Institute of Applied Physics, Academy of Sciences of Moldavia, Kishinev
(Submitted October 16, 1997)
Pis'ma Zh. Tekh. Fiz. **24**, 34–38 (July 12, 1998)

An analysis is made of vibrational packets created in molecules by collisions with fast protons. Some characteristic features of the Raman light scattering spectrum are discussed for a molecule with squeezed vibrational states. It is suggested that squeezed vibrational states in the ground electronic state of a molecule may be used for isotope separation.
© *1998 American Institute of Physics.* [S1063-7850(98)00607-7]

Squeezed states of oscillators for an electromagnetic field (squeezed light) and for squeezed vibrations (squeezed phonons) have recently attracted considerable attention.[1,2] A characteristic feature of the excitation of squeezed vibrational states is that the rates of chemical reactions may increase abruptly and exponentially (laser femtochemistry).[3,4] Most studies usually examine the preparation of squeezed vibrational states in excited molecular states, for example, by excitation of a molecular system with ultrashort laser pulses. However, the creation of squeezed vibrational wave packets in the ground electronic state would allow a new class of processes to be studied, which assume a super-Poisson distribution of vibrational occupation numbers. The simplest example could be the spectrum of Raman light scattering by a molecule in the ground electronic state.

Here we propose a new method of preparing squeezed vibrational states in the ground electronic state of a molecule, based on the excitation of molecular vibrations by collisions between molecules and fast protons. The impact time τ_0 in these collisions is estimated using the formula $\tau_0 = R_0/v$, where R_0 is the characteristic distance at which impact takes place, of the order of 1 Å (Ref. 5), v is the proton velocity: for $v \sim 10^7$ cm/s we have $\tau_0 \sim 1$ fs. For vibrations with the energy $\hbar\omega \sim 0.1$ eV this implies that a wave packet can be excited from ten vibrational states, i.e., $\omega\tau_0 \ll 1$. This case of inelastic collisions is the opposite of the case of slow adiabatic collisions for which $\omega\tau_0 \gg 1$, and is well described using the familiar Landau–Teller theory.[6] It is natural to consider molecular vibrational states accurately described by the harmonic model and having fairly long lifetimes. Such molecules may include many of those studied in laser isotope separation where $\tau_V \sim 10^{-9}$ s, $\hbar\omega \sim 0.1$ eV (see Ref. 7, for example).

To illustrate the fundamental relationships governing the excitation of squeezed vibrational packets, we shall use a simple one-dimensional model of the interaction potential of a heavy classical particle with a molecule, which was proposed in Refs. 8 and 9:

$$W(x,t) = -F(t)\left(1 + \lambda\frac{x}{R_0} + \frac{1}{2}\lambda^2 x^2\right).\qquad(1)$$

Here we have

$$F(t) = \frac{\mu v^2}{2}\cosh^{-2}\frac{vt}{2R_0};\quad \lambda = \frac{m_a}{m_a+m_b},\qquad(2)$$

x is the deviation of the vibrational coordinate from the equilibrium position, μ is the reduced oscillator mass of the impinging particle, and m_a and m_b are the atomic masses in a diatomic molecule.

The Schrödinger time-dependent equation for an oscillator, taking account of $W(x,t)$, may be expressed in the form

$$\psi(x,t) = \int_{-\infty}^{+\infty} dx_1 \int_{-\infty}^{t} dt_1 G_0(xt|x_1t_1)W(x_1,t_1)\psi(x_1,t_1).\qquad(3)$$

Here $G_0(xt|x_1t_1)$ is the Green's function of the oscillator. We assume that the time behavior of the interaction potential $W(x,t)$ in the active region $t \sim \tau_0$ may be sufficiently accurately approximated by a Gaussian pulse

$$F(t) = \frac{\mu v^2}{2}\exp(-t^2/4\tau_0^2).\qquad(4)$$

We use the condition of collisional nonadiabaticity, i.e., the approximation of short times t_1. We replace $\psi(x_1,t_1)$ on the right-hand side of Eq. (2) by $\psi(x_1,0)$. The wave function $\psi(x_1,0)$ is an eigenfunction of the Hamiltonian:

$$H = H_{\text{osc}} + W(x_1,0).\qquad(5)$$

Initially, the oscillator is assumed to be unexcited ($\hbar\omega \gg kt$) so that

$$\psi(x_1,0) = \frac{1}{\pi^{1/4}}\frac{1}{\sqrt{\delta^2}}\exp\left[-\frac{(x-\xi)^2}{2\delta^2}\right],$$

$$\xi = \frac{v^2\lambda}{2d\omega^2};\quad \delta^2 = \frac{\hbar}{\mu\Omega};\quad \Omega^2 = \omega^2 + \frac{\mu v^2\lambda^2}{2R_0^2 m_{ab}}.\qquad(6)$$

The integrals in Eq. (6) can be calculated directly by using the explicit form of the Green's function of the oscillator and the expression for the pulse (3). To simplify the calculations, we replace the narrow Gaussian pulse profile ($\tau_0 \to 0$) with a delta function of t, which appreciably simplifies the calculations. We give the result of integrating in

formula (6) using the accurate expression for the Green's function of the oscillator and the expression for $\psi(x,0)$ (5), which yields

$$|\psi(x,t)|^2 = N \exp[-(x-x_0(t))^2/\sigma^2(t)]. \qquad (7)$$

Here the following notation is introduced:

$$x_0(t) = \xi \cos \omega t; \quad \sigma^2(t) = \delta^2(\cos^2 \omega t + \eta \sin^2 \omega t),$$

$$\eta = \Omega/\omega = [1 + \mu v^2 \lambda^2 / 2R_0^2 m_{ab}\omega^2]^{1/2}, \qquad (8)$$

N is the normalization constant. The probability density obtained for the squeezed state is characterized by the squeezing parameter η which, in the particular case where the quadratic correction λ^2 in the expansion of the potential (1) is neglected, gives $\eta = 1$ and formula (7) describes a coherent packet. Thus, for $\eta > 1$ expression (7) describes a squeezed wave packet with a super-Poisson distribution and the dispersion $\sigma^2(t)$ greater than that of the coherent state δ^2.

Note that expression (7) may be obtained by accurately solving the problem with the potential (1) if this potential is used as the Pöschl–Teller potential in the Schrödinger problem for the motion of a classical oscillator in this potential.[10] In this approach it is convenient to use a secondary quantization basis where the squeezed state is represented as two successive transformations of shear and rotation, acting on the vacuum state. The problem with the Pöschl–Teller potential is solved using a familiar procedure where the constants in the solution of this equation are related to the above-barrier reflection coefficient, as suggested by L. P. Pitaevskiĭ.[10] The accuracy of this solution is the same as the solution (7) with fairly steep functions $F(t)$. It is easily confirmed that only this constraint on the function $F(t)$ gives a class of super-Poisson solutions of the form (7). We have confined ourselves to the simplest calculations of the wave packet for the steep potential $F(t)$.

Experimental observations of a squeezed vibrational packet are primarily based on the fact that the occupation numbers of the oscillator obey a super-Poisson distribution. In analyses of the Raman spectrum of light scattering by a molecule, the ratio of the intensities of the blue I_a (anti-Stokes) and red I_s (Stokes) satellites of the scattered light is determined by the condition $\varkappa = I_a/I_s \cong \bar{n}/(\bar{n}+1)$,

$\bar{n} = [\exp(\hbar\omega/kT)-1]^{-1}$, i.e., asymmetry is observed. The anti-Stokes component in the absence of squeezed states is usually lower than the Stokes component. For coherent and squeezed states the intensities I_a and I_s are equal, so that $\varkappa \sim 1$. A more accurate analysis of the variation of the parameter $\varkappa$ for various velocities of the proton beam incident on the molecules to excite squeezed states will allow the squeezing parameter to be determined experimentally. Since the average occupation numbers vary with time (because of the time dependence of the dispersion of the squeezed vibration), the ratio $\varkappa = I_a/I_s$ will also vary with time. In this case, unlike the method of two successive (short optical) pulses, comprising a preparatory optical pulse and a readout optical pulse, the squeezing parameter can be determined by the simpler technique described above and, which is particularly important, for vibrations in the ground electronic state. This circumstance may be used in laser isotope separation since the amplitudes of the squeezed vibrational states are fairly large and differ appreciably for molecular isotopes.

[1] V. P. Bykov, Usp. Fiz. Nauk **161**(10), 145 (1991) [Sov. Phys. Usp. **34**, 910 (1991)].
[2] A. V. Vinogradov and J. Janskzy, Zh. Éksp. Teor. Fiz. **100**, 386 (1991) [Sov. Phys. JETP **73**, 211 (1991)].
[3] V. A. Kovarskiĭ, Zh. Éksp. Teor. Fiz. **110**, 1216 (1996) [JETP **83**, 670 (1996)].
[4] V. A. Kovarskiĭ, Pis'ma Zh. Tekh. Fiz. **20**(24), 59 (1994) [Tech. Phys. Lett. **20**, 999 (1994)].
[5] A. A. Radtsig and B. N. Smirnov, *Handbook of Atomic and Molecular Physics* [in Russian], Atomizdat, Moscow (1980), 240 pp.
[6] L. Landau and E. Teller, Phys. Z. Sowjetunion **10**, 34 (1936).
[7] V. S. Letokhov, *Nonlinear Selective Photoprocesses in Atoms and Molecules* [in Russian], Nauka, Moscow (1983), 408 pp.
[8] K. V. Stupochenko, S. A. Losev, and A. I. Osipov, *Relaxation in Shock Waves* (Springer-Verlag, Berlin, 1967) [Russ. original, Nauka, Moscow, 1965, 482 pp.].
[9] B. F. Gordiets, A. I. Osipov, and L. A. Shelepin, *Kinetic Processes in Gases and Molecular Lasers* [in Russian], Moscow (1980), 510 pp.
[10] A. I. Baz', Ya. B. Zel'dovich, and A. M. Perelomov, *Scattering, Reactions and Decay in Nonrelativistic Quantum Mechanics*, transl. of 1st Russ. ed. (Israel Program for Scientific Translations, Jerusalem, 1966) [Russ. original, 2nd ed., Nauka, Moscow, 1971], 544 pp.

Translated by R. M. Durham

Influence of the type of cathode on the dynamic characteristics of ionization waves

A. S. Aref'ev and Yu. A. Yudaev

Ryazan State Radio Engineering Academy
(Submitted October 31, 1997)
Pis'ma Zh. Tekh. Fiz. **24**, 39–42 (July 12, 1998)

The influence of different types of cathodes on the dynamic characteristics of ionization waves is determined experimentally. It is established that when the discharge is initiated by negative pulses, the maximum wave propagation velocity is observed for a cold cathode while the maximum peaking of the output pulse leading edge is observed for a heated cathode. The mechanism for this effect is discussed.   © *1998 American Institute of Physics.* [S1063-7850(98)00707-1]

Studies of the influence of different types of cathodes on the dynamic characteristics of wave breakdown of gas gaps are of considerable theoretical and practical interest. An analysis of the scientific literature[1,2] does not answer the question as to how the emission from the surface of the electrode influences the dynamic characteristics of the ionization waves (displacement velocity, formation time, current pulse peaking, and so on). Moreover, many publications assert that the type of cathode does not influence the properties of the ionization waves. However, our experimental investigations have shown that thermionic emission from the cathode plays some role in the formation of ''slow'' ionization waves when the propagation velocity lies in the range 10^6–10^7 m/s. The apparatus used for the experimental investigations is shown schematically in Fig. 1. The distance between the ends of the electrodes was 270 mm and the diameter was 30 mm. To achieve uniform experimental conditions, the investigations were carried out using a single prototype where an indirectly heated oxide cathode *4* functioned as the cold and the heated cathode.

The measurements of the wave propagation velocity were made assuming that the current-recording detectors *5* are separated by the distances L_1 and L_3 from the volume where the plasma forms (Fig. 1), so that the propagation velocity of the high-voltage pulse in these sections was taken equal to the velocity of light and the propagation velocity of

the ionization wave was determined using the formula

$$V = L_2/(t_2 - t_1 - (L_1 + L_3)/c),$$

where t_1 and t_2 are the times of appearance of the signal at the first and second current detectors, respectively, c is the velocity of light, and L_1, L_2, and L_3 are distances as shown in Fig. 1.

Figures 2a and 2b give the propagation velocity of the ionization wave as a function of the neon pressure for the prototype with different types of cathodes. The discharge was ignited by negative pulses from the cathode side with a rate of rise of 5×10^{11} V/s.

A comparative analysis of these curves reveals that the ionization wave propagates at a higher velocity with a cold cathode than with a heated one. This behavior may be attributed to the following factors. The propagation velocity of the ionization wave is influenced by two interrelated processes, impact and photoionization. The relative influence of these factors on the ion formation mechanism depends on the filler gas concentration. At low pressure, both processes play a negligible role and the ionization wave has a low velocity. A rise in pressure increases the role of photoionization and impact ionization. The maximum propagation velocity (Fig. 2) corresponds to the optimum conditions for the formation of charged particles.
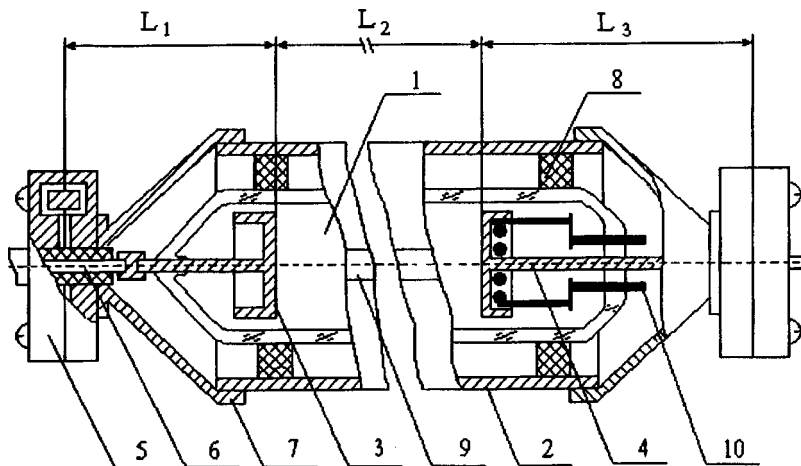

FIG. 1. Prototype to investigate dynamic characteristics of ionization waves: *1*—envelope, *2*—screen, *3*—anode, *4*—cathode, *5*—current shunts, *6*—high-voltage cable, *7*—adjusting device, *8*—insulator, *9*—slit for visual observations, and *10*—cathode heater leads.
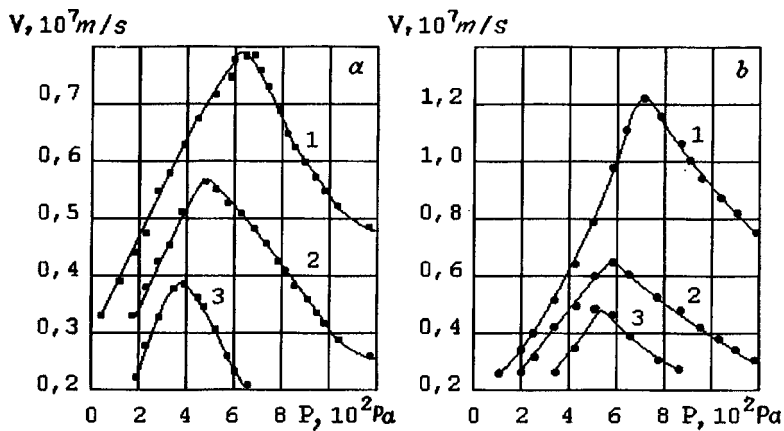
FIG. 2. Propagation velocity of ionization wave versus neon pressure for various types of cathodes: a—heated, b—cold. Negative control pulses $dU/dt = 5 \times 10^{11}$ V/s: *1*—13 kV; *2*—11 kV; *3*—9 kV.

As the amplitude of the initiating pulses increases, the maximum of the wave propagation velocity shifts toward higher pressures for both the cold and heated cathodes. An increase in the amplitude of the voltage pulse applied to the gap leads to an increase in the energy acquired by the electrons over the mean free path but at the same time, reduces the probability of the gas atoms being ionized, which causes a drop in the wave propagation velocity in the gap. Only an increase in pressure can reduce the mean free path for which the electron ionization probability will have a maximum.

With a heated cathode it is considerably easier for electrons to escape from the surface of the electrode, so that the plasma forms more rapidly than with a cold cathode, when a longer time is required to produce the same concentration of charged particles. The presence of a heated cathode makes the plasma formation process more vigorous but the charged particles begin to form at a lower electrode voltage, making the wave propagation velocity lower than that for a cold cathode (Fig. 2).

The type of cathode also influences the shape of the current pulse. With a heated cathode, the output pulse shows stronger peaking at a lower propagation velocity.

When the rate of rise of the initiating voltage was increased to 5×10^{12} V/s, the maximum propagation velocity shifted to higher pressure and the differences in the propagation velocity of the ionization waves progressively decrease.

Changes in the cathode geometry (length, diameter, surface area, configuration) did not alter the temporal and energy characteristics of the ionization waves.

Formation of the discharge by positive pulses from the anode side showed that the dynamic characteristics of the ionization waves do not depend on the nature of the second electrode, except for the leading edge duration of the current pulse and the voltage recorded in the cathode circuit. With a heated cathode the output pulse showed stronger peaking than for the cold cathode, although the propagation velocity was the same in both cases. Changes in the amplitude and slope of the applied voltage pulses altered the quantitative results, without changing the general behavior of the processes.

Using these phenomena in plasma current switches could improve their speed by several factors and increase the rate of rise of the anode current.[3]

[1] É. I. Asinovskiĭ, L. M. Vasilyak, and V. V. Markovets, Teplofiz. Vys. Temp. **21**, 577 (1983).
[2] A. N. Lagar'kov and I. M. Rutkevich, *Ionization Waves in Electrical Breakdown of Gases*, Springer-Verlag, New York (1994) [Russian orig.] Nauka, Moscow (1989), 206 pp.
[3] A. S. Arefiev and Yu. A. Yudaev, in *Proceedings of the Twelfth International Conference on Gas Discharges and their Applications*, Greifswald, Germany, 1977, Vol. 2, p. 800.

Translated by R. M. Durham

Synergic model of the superplastic deformation of materials

A. K. Emaletdinov

Servis Technological Institute, Ufa

A study is made of a synergic model of superplastic deformation of ultrafine-grained materials at high temperatures as a manifestation of collective modes of motion and self-organization in a system of stimulated grain-boundary slip. The evolution of grain-boundary slip is accompanied by the formation of a wavefront which separates two steady states of the system and leads to the appearance of the experimentally observed ''running neck'' at the surface of the sample. The synergic model is used to explain the scaling effect of superplasticity. © *1998 American Institute of Physics.* [S1063-7850(98)00807-6]

The superplasticity of inorganic materials is of major practical significance and is observed as a result of the development of a stable ultrafine-grained structure and deformation in a certain range of temperature and strain rate (usually for grain sizes $d_s \simeq 10$–15 μm, $T_s \simeq 0.5$–$0.6 T_m$, $\dot{\varepsilon}^p = 10^{-3}$–$10^{-1}$ s^{-1}) (Refs. 1–3). It has now been convincingly established that three deformation micromechanisms are involved simultaneously in superplastic deformation: grain-boundary slip, intragranular dislocation glide, and diffusion creep.[1–4] Grain-boundary slip occurs in two forms:[5] intrinsic slip at the velocity V_0 and slip stimulated by lattice slip at the velocity V_s, where $V_s \gg V_0$. It was established in Ref. 6 that in superplasticity, collective modes appear in the motion of ensembles of grains. The aim of the present study is to analyze the synergic model of superplastic deformation as a manifestation of grain-boundary, self-oscillating, dissipative structures.

The production of entropy in superplastic deformation is related to the rate of irreversible deformations: dissipative processes and their contribution to the total deformation. In the optimum range of strain rates (region II), the contributions of grain-boundary slip γ_g, intragranular dislocation glide γ_D, and dislocation creep γ_p are respectively given by[1,4] $\gamma_g \gtrsim 0.8$, $\gamma_D \lesssim 0.2$, $\gamma_p \to 0$. From the point of view of nonequilibrium thermodynamics and synergetics,[7] the appearance of a temperature–rate range for the onset of superplasticity is caused by a change in the dissipative process controlling the deformation: in region I the main processes are isolated dislocation glide and creep, in region II grain-boundary processes predominate, and in region III multiple dislocation glide is the dominant process.

On the basis of the physical model of superplastic deformation proposed in Ref. 4, we shall analyze a polycrystalline material consisting of equiaxial grains of average size d, deformed at the optimum rate $\dot{\varepsilon}^p$ (region II). The deformation is accomplished by grain-boundary defects of density ρ_1 and lattice dislocations of density ρ_2. The action of the dislocation glide produces stimulated grain-boundary slip with the bulk density ρ_3 (Fig. 1). In superplastic deformation collective modes appear in the motion of ensembles of grains when grain-boundary slip becomes a cooperative process incorporating the grain-boundary slip of many grains. The order parameters determining the behavior of the grain system in superplastic deformation will be collective, long-wavelength modes of grain-boundary slip. The controlling parameters will be the strain rate $\dot{\varepsilon}^p$ and the temperature T.

The defect interaction diagram has the form $\rho_1 \xrightarrow{\tau_g} \rho_2 \underset{\tau_0}{\overset{\tau_D}{\rightleftharpoons}} \rho_3$ where τ_g is the nucleation time for a lattice dislocation at the boundary and τ_D is the dissociation time for a lattice dislocation at grain-boundary defects in the boundary.[4] We write the basic equations for the dislocation kinetics in the relaxation time approximation in the form
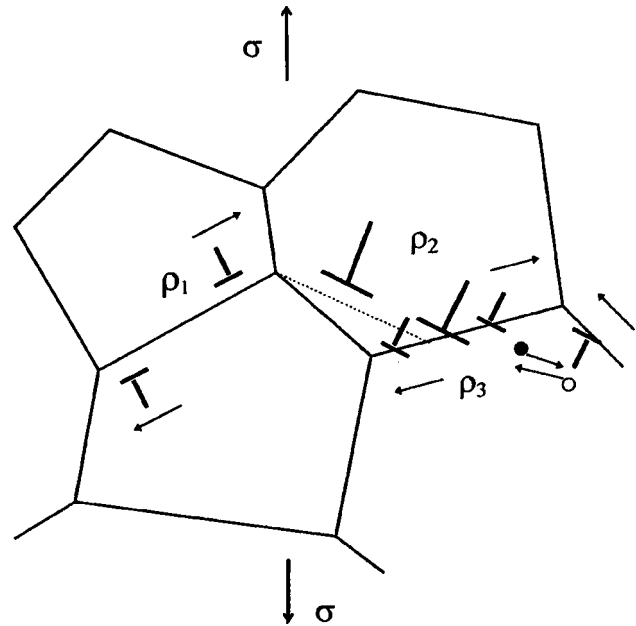

FIG. 1. Diagram showing the evolution of micromechanisms responsible for superplastic deformation: ρ_1—density of grain-boundary defects, ρ_2—density of lattice dislocations, and ρ_3—density of introduced grain-boundary defects.
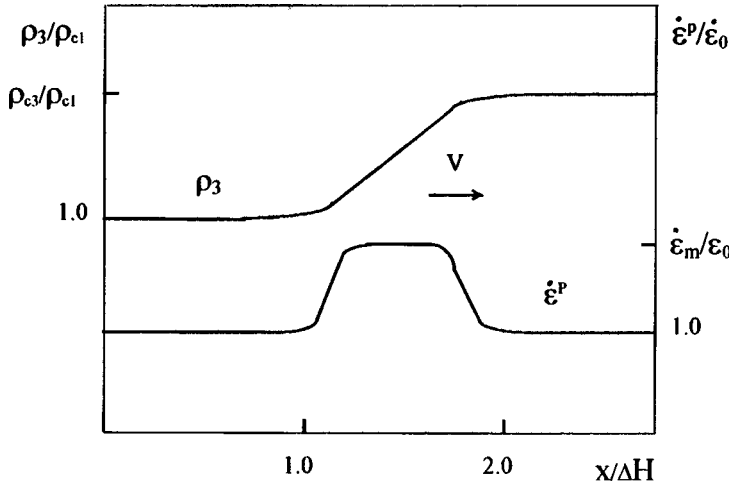
FIG. 2. Density of grain-boundary defects ρ_3/ρ_{c1} and strain rate $\dot{\varepsilon}^p/\dot{\varepsilon}_0$ as functions of distance $x/\Delta H$ in traveling neck.

$$\dot{\rho}_1 = A - \rho_1/\tau_g + \rho_2/\tau_D - k\rho_2\rho_3 + D_1\nabla^2\rho_1,$$

$$\dot{\rho}_2 = -\rho_2/\tau_D + \rho_1/\tau_g,$$

$$\dot{\rho}_3 = (\rho_* - \rho_3)/\tau_0 + k\rho_2\rho_3 - c\rho^2 + D_2\nabla^2\rho_3, \qquad (1)$$

where τ_0 is the annihilation time for grain-boundary defects at sinks (such as grain boundary joins, and so on), A is the rate of nucleation of dislocations, and k and c are normalization coefficients. Here it is assumed that the defect distribution exhibits substantial spatial nonuniformity, described by introducing the "diffusion term." Within a single grain we find ρ_1, $\rho_3 =$ const and gradients occur only when considering neighboring grains. The rapid transfer of active deformation from some boundaries to neighboring ones (Fig. 1) is accompanied by the formation of density gradients ρ_1 and ρ_3, and the "diffusion" coefficients of the defect flux densities will be given by $D_1 \lesssim d^2/\tau_D$ and $D_2 \lesssim d^2/\tau_g$. The initial conditions are $(\rho_{10}, 0, 0)$.

We shall analyze the system using bifurcation theory methods and Poincaré maps.[8] A search for the steady-state points of the system and their analysis using the linearized system of equations (1) revealed that the following steady states exist: two saddle-type points $(A\tau_0, A\tau_0\tau_D/\tau_g, 0)$ and $(\rho_{s1}, \rho_{s2}, \rho_{s3})$ for $A > \tau_g/K\tau_D\tau_0^2$ and the unstable focus point $(\rho_{F1}, \rho_{F2}, \rho_{F3})$ for $\rho_* > \rho_{c*}$. An analysis of the solutions of the kinetic equations (1)—space-time dissipative structures—may be sought in the form of expansions as a Fourier series in terms of plane waves $\rho \sim \Sigma_k \exp(pt + ikx)$. The characteristic equation of the system (1) has two types of solutions: 1) a spatially homogeneous solution and 2) a periodic, self-oscillating solution (traveling neck regime[1–3]). Periodic solutions are generated according to the type of Hopf bifurcation. Thus, there exists a critical density of activated grain-boundary slip boundaries when a self-oscillating regime is established in the system

$$\rho_{c*} = (k\tau_D A^2 \tau_0^2/\tau_g^2)(1+z)/(3+z), \quad z = 2\tau_g/Ak\tau_0^2\tau_D.$$

The type of wave regime is analyzed using the method of multiscale expansions[7] in terms of the small parameter

$D_1/D_2 \ll 1$. Converting to slow variables in Eqs. (1), we obtain in the first approximation $(t/\tau_0 = \tau, \xi = x/(D_2\tau_0)^{1/2}, \rho = \rho_3/\rho_*)$

$$\dot{\rho} = 1 + A\rho/(b_0 + d_0\rho_*\rho) - \alpha_0\rho - c\rho_*^2\rho^2 + \nabla^2\rho. \qquad (2)$$

Equation (2) for the slow amplitude of the cooperative grain-boundary slip has three established steady-state points. Physically this means that the system is stable at the minimum and maximum densities of grain-boundary defects and is unstable for ρ_{c2}. That is to say, a front or "neck" appears in the system, separating the two steady states ρ_{c1} and ρ_{c3}. Solving Eq. (2) in terms of the self-similar variable $\xi = x - Vt$, where V is the velocity of the front, with the boundary conditions ρ_{c2}, $\xi \to \pm\infty$, $\rho'_\xi = 0$, $\rho = \rho_{c1}$, we obtain an implicit expression for the defect distribution ρ in the form $\xi = \int d\rho/F(\rho, \alpha_0, d_0, \rho_*, c, k)$, where $F(z)$ is a given function. In the first approximation we have

$$\rho(\xi) \lesssim \rho_{c1} + (\rho_{c3} - \rho_{c1})/[1 + \exp(2\alpha_0(\rho_{c3} - \rho_{c1}))\xi/V]. \qquad (3)$$

The width of the front is determined in the first approximation by $\Delta H \simeq \tau_g D_2(\rho_{c3} - \rho_{c1})/\rho_*(D_1\tau_0)^{1/2}$. Estimates of V and ΔH for superplastic deformation are of the order $V \simeq 10^{-1}$ cm/s and $\Delta H \simeq 10^{-1}$ cm, which is similar to the experimental data.[1–3] A numerical solution of the system (1) is shown in Fig. 2.

Dissipative structures can only form when the dimensions of the nonequilibrium system (the sample) L exceed certain critical values.[7] For superplasticity, the minimum dimension L_c is determined by the condition for the appearance of collective modes and self-organization in the system of stimulated grain-boundary slip and has the form

$$L_c = (F_1(d_0, f'(\rho_{c1}), g'(\rho_{c3}), V, \tau_g))^{1/2} \gtrsim (\Delta H \cdot V \cdot \tau_g)^{1/2},$$

where $f(z)$ and $g(z)$ are the right-hand sides of the system (1), and $F_1(z)$ is a given function. An order-of-magnitude estimate of L_c gives $10^2 - 10^3$ μm. In Ref. 6, a departure

from superplastic deformation was in fact observed when the sample dimension was of the order of 60 μm.

[1] O. A. Kaĭbyshev, *Plasticity and Superplasticity of Metals* [in Russian], Metallurgiya, Moscow (1975), 280 pp.

[2] M. V. Grabskiĭ, *Structural Superplasticity of Metals* [in Russian], Metallurgiya, Moscow (1975), 280 pp.

[3] A. S. Tikhonov, *Superplasticity of Metals and Alloys* [in Russian], Nauka, Moscow (1978), 141 pp.

[4] O. A. Kaĭbyshev, R. Z. Valiev, and A. K. Emaletdinov, Dokl. Akad. Nauk SSSR **279**, 369 (1984) [Sov. Phys. Dokl. **29**, 967 (1984)].

[5] O. A. Kaĭbyshev, V. V. Astanin, and R. Z. Valiev, Dokl. Akad. Nauk SSSR **245**, 1356 (1979) [Sov. Phys. Dokl. **24**, 289 (1979)].

[6] V. V. Astanin, Fiz. Met. Metalloved. **79**(3), 166 (1995).

[7] G. Nicolis and I. Prigogine, *Self-Organization in Non-Equilibrium Systems* (Wiley, New York, 1977; Mir, Moscow 1979, 512 pp.).

[8] A. A. Andronov, E. A. Leontovich, I. I. Gordon, and A. G. Maĭer, *Qualitative Theory of Second-Order Dynamic Systems* [in Russian], Nauka, Moscow (1966), 326 pp.

Translated by R. M. Durham

Resolution of optically addressed liquid-crystal spatial light modulators

V. F. Nazvanov and D. I. Kovalenko

Saratov State University

Results are presented of calculations of the modulation transfer function of optically addressed, liquid-crystal, spatial light modulators based on layered photoconductor–liquid crystal structures, including surface-plasmon light modulators. Allowance is made for diffusive spreading of carriers in the photoconductor and the propagation length of surface plasmons in the layered structures. © *1998 American Institute of Physics.* [S1063-7850(98)00907-0]

Several models have been proposed to understand the constraints on the resolution of optically addressed spatial light modulators.[1–11] It has been shown that in optically addressed spatial light modulators based on photodetector–liquid crystal layered structures, the resolution is primarily determined by the thicknesses and dielectric constants of the photoconductor and liquid crystal layers. Theoretical and experimental investigations[1,4–6,10,13] have also shown that, in addition to the thickness of the liquid crystal layer, the resolution is also influenced by the orientation of the molecules in the liquid crystal layer and by its dielectric anisotropy. Allowance should also be made for diffusive spreading (and/or drift) of photoexcited carriers in the photoconductor which drastically reduces the resolution of spatial light modulators. Direct allowance for the carrier diffusion length in the photoconductor in calculations of the resolution of optically addressed liquid-crystal spatial light modulators was apparently proposed for the first time by one of the present authors in Ref. 7.

Here we present an expanded version of Ref. 7 in which we calculate the modulation transfer function of optically addressed liquid-crystal spatial light modulators. In addition, in the surface plasmon calculations[14,15] we also allow for the propagation length of the surface plasmons. It should be noted that a similar[7] but slightly different version was also proposed in Ref. 11 to allow for the diffusion spreading length of the carriers in the photosensor part of optically addressed, liquid-crystal spatial light modulators.

An expression was derived in Ref. 12 for the modulation transfer function of a light modulator formed by a two-layer structure consisting of an isotropic dielectric (photoconductor) and a layer of dielectric anisotropic material, assuming a sinusoidal charge distribution at the interface between the two layers. For a photoconductor–liquid crystal structure the modulation transfer function depends mainly on the ratio S_N/S_0, given by[8,12,16]

$$\frac{S_N}{S_0} = \frac{1}{\pi \nu} \frac{\varepsilon_{PS}/d_{PS} + \varepsilon_1/d_{LC}}{\varepsilon_{PS} \coth(\pi \nu d_{PS}) + \sqrt{\varepsilon_1 \varepsilon_2} \coth(\pi \nu \sqrt{\varepsilon_2/\varepsilon_1} d_{LC})}, \tag{1}$$

where d_{PS} is the thickness of the photosensor, ε_{PS} is the permittivity of the photosensor, d_{LC} is the thickness of the

liquid crystal, ε_1 is the parallel permittivity of the liquid crystal, and ε_2 is its perpendicular permittivity.

In their derivation of formula (1) the authors of Refs. 8, 12, and 16 neglected diffusive spreading of carriers in the photoconductor layer, although they did not deny the importance of this effect.

Diffusive spreading (and/or drift in the presence of an electric field) of photocarriers in the photoconductor may be taken into account directly[7] in calculations of the modulation transfer function by multiplying the ratio S_N/S_0 by the frequency-contrast characteristic of the photoconductor.[17,18]

In fact, the use of a photoconductor layer as one of the main elements in optically addressed light modulators is largely attributable to the capacity of a photoconductor with a specific contrast to produce an image of the exciting radiation, as occurs in iconics for photographic materials.[17] Calculations[18] show that the distribution of the nonequilibrium carrier concentration in a photoconductor obeys the same cosinusoidal distribution as the excitation function. However, the amplitude of the variation in the concentration differs from that of the excitation function by the factor $T(\nu, L_D)$, which depends on the spatial frequency ν and the diffusion wavelength L_D. Consequently, in the photoconductor the excitation function is converted into the spatial distribution function of the concentration with the frequency-contrast characteristic

$$T(\nu, L_D) = 1/(1 + 4\pi^2 \nu^2 L_D^2). \tag{2}$$

In the presence of an electric field in the photoconductor, the carrier displacement length in the field[19] should be taken instead of L_D. In general, for a photoconductor layer in an optically addressed spatial light modulator, this length depends on the voltage V across the photoconductor layer, the intensity of the writing light, the degree of modulation m, and also the spatial frequency.[7]

Figure 1 gives results of calculating the modulation transfer function of an optically addressed spatial light modulator comprising a bismuth silicate–liquid crystal structure from Ref. 16, neglecting and allowing for the diffusion length (curves *1* and *2*, respectively). This clearly shows that L_D influences the resolution of the optically addressed spatial light modulator. Using the experimental data from Ref. 16,
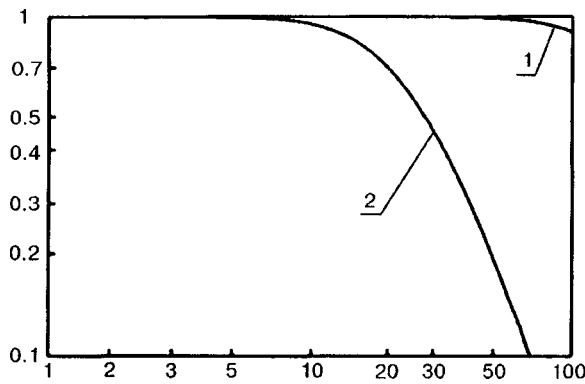
FIG. 1. Modulation transfer function of an optically addressed spatial light modulator based on a bismuth silicate–liquid crystal structure[16] with a modulation coefficient of 1: 1—L_D=0; 2—L_D=8 μm.
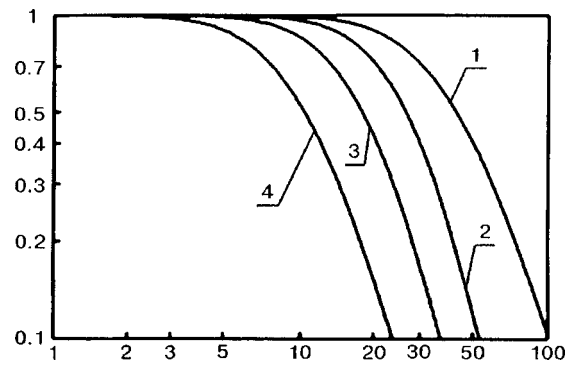

FIG. 2. Modulation transfer function of an optically addressed spatial light modulator based on an amorphous silicon–liquid crystal structure[14] with L_D=5 μm and a modulation coefficient of 1: 1—L_{SP}=0; 2—L_{SP}=5 μm; 3—L_{SP}=10 μm; 4—L_{SP}=20 μm.

we estimated the carrier spreading length in bismuth silicate to be 13.6 μm, which agrees with the real value.[20]

The resolution of surface-plasmon liquid-crystal light modulators is also extremely interesting.[14,15,21] In this type of spatial light modulator, in addition to allowing for the diffusive spreading of carriers in the photoconductor (corresponding to the frequency-contrast characteristic of the photosensor in an optically addressed spatial light modulator), it is also necessary to take into account[21] the blurring of the "picture" written in the photoconductor as a result of the finite propagation length L_{PS} of the plasmons in the photoconductor–liquid crystal layered structure. It is easy to imagine that the system for reading the image from an optically addressed spatial light modulator comprising a photoconductor–liquid crystal structure with surface plasmon excitation[14,15] is the second component of a general system for reproduction of an object, while the first is a system for writing the object in the photoconductor and thus in the photoconductor–liquid crystal structure. Then, in accordance with iconics,[17] for the entire surface-plasmon, optically addressed liquid-crystal spatial light modulator system, we can introduce the frequency-contrast characteristic determined by simply multiplying the characteristics of the system components, and specifically the frequency-contrast characteristic

$$T_0(\nu) = T(\nu, L_D) T(\nu, L_{SP}), \qquad (3)$$

where $T(\nu, L_{SP})$ is similar to Eq. (2), where the diffusion (or spreading) length L_D should be replaced by the surface plasmon propagation length. Thus, to allow directly for both the diffusion spreading length and the surface plasmon propagation length in calculations of the modulation transfer function of a surface-plasmon, optically addressed liquid-crystal spatial light modulator, expression (1) for S_N/S_0 must be multiplied by $T_0(\nu)$ as given by Eq. (3).

Figure 2 gives results of calculations of the modulation transfer function of a surface-plasmon, optically addressed, liquid-crystal spatial light modulator with the layer parameters taken from Ref. 14, allowing not only for the diffusion length but also for the surface plasmon propagation length. It is easy to see that L_{SP} limits the resolution of a surface-plasmon spatial light modulator. We used experimental

curves of the modulation transfer function[14] to calculate the lengths L_{SP} for the two directions of propagation of the surface plasmons studied in Ref. 14 and we obtained (for our assumed carrier spreading length of 2 μm in a layer of amorphous silicon) 8.2 μm (for ν=25 line/mm) and 16.9 μm (for ν=13 line/mm), respectively.

To conclude, direct allowance for the diffusive spreading of the carriers in the photosensor part of an optically addressed, liquid-crystal spatial light modulator can be made by introducing the frequency-contrast characteristic of the photoconductor into the expression for the modulation transfer function of the spatial light modulator. For surface-plasmon, optically addressed, liquid-crystal spatial light modulators, the propagation length of the surface plasmons is taken into account by introducing the frequency-contrast characteristic of the plasmon image reading system at the same time as that of the photosensor.

[1] A. A. Vasil'ev, Trudy Fiz. Inst. Akad. Nauk SSSR **126**, 3 (1981).

[2] U. Efron *et al.*, Opt. Eng. **22**, 682 (1983).

[3] S. S. Ignatosyan, V. P. Simonov, and B. M. Stepanov, Opt. Mekh. Promst. No. 1, 7 (1986) [Sov. J. Opt. Technol. **53**, 6 (1986)].

[4] A. A. Vasil'ev, Yu. K. Gruzevich, S. N. Levov *et al.*, Preprint No. 1 [in Russian], Lebedev Physics Institute, Academy of Sciences of the USSR, Moscow (1986).

[5] A. A. Vasil'ev, D. Kasasent, I. N. Kompanets, and A. V. Parfenov, *Spatial Light Modulators* [in Russian], Radio i Svyaz', Moscow (1987), 320 pp.

[6] Yu. D. Dumarevskiĭ, N. F. Kovtonyuk, and A. I. Savin, *Image Conversion in Semiconductor–Insulator Structures* [in Russian], Nauka, Moscow (1987), 176 pp.

[7] V. F. Nazvanov and A. V. Novikov, Abstracts of Papers presented at the First All-Union Seminar "Optics of Liquid Crystals," Leningrad, 1987 [in Russian], p 189.

[8] S. S. Ignatosyan, Opt. Mekh. Promst. No. 4, 4 (1988) [Sov. J. Opt. Technol. **55**, 198 (1988)].

[9] I. V. Fedorov, V. Yu. Zlatov, A. O. Radkevich, and A. V. Khlestov, Vopr. Radioélektroniki Ser. Obshch. Vopr. Radioélektron. [in Russian], No. 10, pp 51–59 (1990).

[10] N. F. Kovtonyuk and E. N. Sal'nikov, *Photosensitive MIS Devices for Image Conversion* [in Russian], Radio i Svyaz', Moscow (1990), 160 pp.

[11] P. R. Barbier, L. Wang, and G. Moddel, Opt. Eng. **33**, 1322 (1994).

[12] W. R. Roach and E. D. Frans, IEEE Trans. Electron Devices **ED-21**, 8–453 (1954).

[13] V. G. Chigrinov *et al.*, Mol. Cryst. Liq. Cryst. **55**, 193 (1979).

[14] M. E. Gardwell and E. M. Yeatman, Appl. Opt. **31**, 3880 (1992).

[15] V. F. Nazvanov, O. A. Afonin, and A. I. Grebennikov, Quantum Electron. **25**, 1028 (1995).

[16] P. Aubourg et al., Appl. Opt. **21**, 3706 (1982).

[17] K. V. Vendrovskiĭ and A. I. Veĭtsman, *Iconics* [in Russian], Nauka, Moscow (1968), p. 97.

[18] N. P. Aban'shin, D. I. Bilenko, and V. A. Lodgauz, Izv. Vyssh. Uchebn. Zaved. Fiz. **10**, 143 (1971).

[19] S. M. Ryvkin, *Photoelectric Effects in Semiconductors* (Consultants Bureau, New York, 1964) [Russ. original, Fizmatgiz, Moscow, 1963].

[20] M. P. Petrov, S. I. Stepanov, and A. V. Khomenko, *Photosensitive Electrooptic Media in Holography and Optical Information Processing* [in Russian], Nauka, Leningrad (1983), p. 88.

[21] V. F. Nazvanov, Scientific-Technical Report on ''Plasmon–Polariton'', Scientific Research Program No. 01.9.10.03393, Scientific-Research Institute of Mechanics and Physics, Saratov, on behalf of Saratov State University (1992) [in Russian].

Translated by R. M. Durham

Reduction in the critical conditions for instability of a highly charged droplet moving relative to a medium

S. O. Shiryaeva, V. A. Koromyslov, and O. A. Grigor'ev

Yaroslavl State University
(Submitted September 19, 1997; resubmitted February 10, 1998)
Pis'ma Zh. Tekh. Fiz. **24**, 54–57 (July 12, 1998)

It is shown that as the flow velocity of an ideal liquid flowing around a charged perfectly conducting droplet of ideal liquid increases, the critical self-charge of the droplet at which instability occurs decreases rapidly. © *1998 American Institute of Physics.*
[S1063-7850(98)01007-6]

Charged droplets moving relative to some medium are encountered in a wide range of problems in technical physics, geophysics, and technology.[1–3] However, whereas a considerable number of investigations have examined the breakup of free-falling droplets in the atmosphere,[4] problems involving the laws governing the buildup of instability in droplets with respect to their self-charge and with respect to a tangential discontinuity in the velocity field at the free surface of the droplet have not yet been addressed. Since the critical conditions for the instability of capillary waves at a charged liquid surface in the presence of a tangential velocity field do not depend on viscosity,[5] we shall examine models of ideal liquids to simplify the following reasoning.

We shall assume that an ideal incompressible dielectric medium having the density ρ_1 and permittivity ε moves at a constant velocity $\mathbf{U}$ relative to a spherical droplet of radius R, comprising an ideal, perfectly conducting liquid of density ρ_2, carrying the charge Q, where σ is the surface tension at the interface of the media. We shall find the critical conditions for instability of capillary vibrations of the droplet under these conditions.

We shall solve the problem in a spherical coordinate system with its origin at the center of the droplet using a linear approximation with respect to a perturbation $\xi(\theta,t)$ of the free surface of the droplet caused by thermal capillary waves and having peak values of $\sim 10^{-8}$ cm. The equation for the free surface of the droplet has the form $r(\theta,t) = R + \xi(\theta,t)$.

The expression for the velocity field of the irrotational liquid flow around the unperturbed droplet has the form[6]

$$\mathbf{V}(\mathbf{r}) = -\frac{R^3}{2r^3}[3\mathbf{n}(\mathbf{U}\cdot\mathbf{n}) - \mathbf{U}] + \mathbf{U}. \tag{1}$$

We shall assume that the wave motion in the droplet and in the surrounding medium is irrotational, with the harmonic velocity potentials Ψ_1, Ψ_2, and the electrostatic potential Φ satisfying the problem

$$\Delta\Psi_i = 0; \quad (i = 1;2); \quad \Delta\Phi = 0;$$

$$r \to \infty: \quad \nabla\Psi_1 = \mathbf{U}; \quad \Phi \to 0;$$

$$r = 0: \quad \nabla\Psi_2 = 0;$$

$$r = R + \xi: \quad \frac{\partial\xi}{\partial t} + \frac{1}{r^2}\frac{\partial\Psi_1}{\partial\theta}\frac{\partial\xi}{\partial\theta} = \frac{\partial\Psi_1}{\partial r};$$

$$\frac{\partial\xi}{\partial t} = \frac{\partial\Psi_2}{\partial r};$$

$$-\rho_1\frac{\partial\Psi_1}{\partial t} + \rho_2\frac{\partial\Psi_2}{\partial t} - \rho_1(\nabla\boldsymbol{\Psi_1})^2 - P_Q + P_\sigma = 0;$$

$$\Phi = \text{const};$$

$$P_\sigma(\xi) = -\frac{\sigma}{R^2}(2 + \Delta_\Omega)\xi;$$

$$P_Q = -\frac{Q^2}{2\pi\varepsilon R^4}\xi + \frac{Q^2}{4\pi\varepsilon R^4}$$

$$\times \sum_n (n+1)Y_n(\mu)\int_{-1}^{1}\xi Y_n(\mu)d\mu,$$

where Δ_Ω is the angular component of the Laplace operator in spherical coordinates.

We shall seek the solution of this problem in the linear approximation with respect to the surface perturbation ξ (as was done for the similar problem of the Helmholtz instability[6]) in the form

$$\Psi_1(\mathbf{r},t) = \varphi + \sum_n A_n r^{-(n+1)}Y_n(\mu)\exp(St);$$

$$\Psi_2(\mathbf{r},t) = \sum_n B_n r^n Y_n(\mu)\exp(St);$$

$$\xi(\mathbf{r},t) = \sum_n Z_n Y_n(\mu)\exp(St).$$

Y_n are spherical functions, A_n, B_n, and Z_n are first-order coefficients, φ is the potential of the liquid velocity field (1), of zeroth order, and the quadratic term $\sim(\nabla\boldsymbol{\Psi_1})^2$ in the dynamic boundary conditions at the free surface of the liquid is retained because it contains φ as a term.

This problem can easily be solved by conventional methods.[5] In terms of dimensionless variables where $R = 1$,

$\sigma = 1$, and $\rho_2 = 1$, we obtain an infinite system of homogeneous algebraic equations for the amplitudes of the capillary vibrations of the droplet:

$$\rho U^2 K_n Z_{n-2} - \rho U S L_n Z_{n-1} + \left\{ \left(\frac{\rho}{(n+1)} + \frac{1}{n} \right) \right.$$

$$\times S^2 - \rho U^2 M_n + (n-1)[n+2-W] \bigg\}$$

$$\times Z_n - \rho U S I_n Z_{n+1} + \rho U^2 J_n Z_{n+2} = 0, \qquad (2)$$

$$W \equiv \frac{Q^2}{4\pi\varepsilon}; \quad M_n \equiv \frac{9\alpha_n\alpha_{n-1}}{2n} + \frac{9\beta_n\alpha_{n+1}}{2(n+2)};$$

$$K_n \equiv \frac{9\alpha_n\alpha_{n-1}}{2n}; \quad L_n \equiv \frac{(9n+6)\alpha_n}{2n(n+1)};$$

$$I_n \equiv \frac{(9n+12)\beta_n}{2(n+1)(n+2)}; \quad J_n \equiv \frac{9\beta_n\beta_{n+1}}{2(n+2)}; \quad \rho \equiv \rho_1/\rho_2;$$

$$\alpha_n \equiv \frac{n(n-1)}{\sqrt{(2n-1)(2n+1)}}; \quad \beta_n \equiv \frac{(n+1)(n+2)}{\sqrt{(2n+1)(2n+3)}}.$$

A necessary and sufficient condition for the existence of a solution of this system is that the determinant composed of the coefficients of the unknown amplitudes Z_n should be zero. This constraint yields a dispersion equation for the problem which, neglecting mode interaction, has the simple form

$$S_n^2 = [n(n-1)[W-n+2] - n\rho U^2 M_n] \left(\frac{n\rho}{(n+1)} + 1 \right)^{-1}. \qquad (3)$$

The droplet becomes unstable when S_2^2 passes through zero and becomes negative. If this condition is satisfied, the amplitude of the dominant mode begins to increase exponentially with time, which leads to the successive excitation of the amplitudes of higher-order modes[3] and the droplet decays according to the law described in Ref. 7. It can be seen from Eq. (3) that as the velocity of the flow around the droplet increases, the critical Rayleigh parameter $W = W_*$ for the onset of instability decreases rapidly:

$$W_* = 4 - \rho U^2 M_2.$$

This observation justifies renewed efforts to construct a physical model for the initiation of a lightning discharge based on the idea of ignition of a corona discharge near a free-falling large melting hailstone in a thundercloud[8–10] consistent with the real conditions obtained in a thundercloud (using measured values of the charges on hailstones, the intracloud electric field, and the falling velocity of the hailstones).

To conclude, we note that the ideal liquid approximation used for the analysis does not restrict the generality of the result since the critical conditions for instability of a droplet with respect to its self-charge do not depend on the viscosity of the liquid.

[1] S. I. Shevchenko, A. I. Grigor'ev, and S. O. Shiryaeva, Nauch. Prib. **1**(4), 3 (1991).

[2] A. I. Grigor'ev, Yu. A. Syshchikov, and S. O. Shiryaeva, Zh. Prikl. Khim. **62**, 2020 (1989).

[3] A. I. Grigor'ev and S. O. Shiryaeva, Izv. Ross. Akad. Nauk Ser. Mekh. Zhidk. Gaza No. 3, 3 (1994).

[4] A. L. Gonor and V. Ya. Rivkind, Itogi Nauki i Tekhniki. Ser. Mekhanika Zhidkosti i Gaza Vol. 17 [in Russian], VINITI, Moscow (1982), pp. 98–159.

[5] S. O. Shiryaeva and A. I. Grigor'ev, *Methods of Calculating Critical Conditions for Electrohydrodynamic Instabilities* [in Russian], Yaroslavl State University Press, Yaroslavl (1996), 60 pp.

[6] L. D. Landau and E. M. Lifshitz, *Fluid Mechanics*, 2nd ed. (Pergamon Press, Oxford, 1987) [Russ. original, 3rd ed, Nauka, Moscow, 1986, 733 pp.].

[7] A. I. Grigor'ev and S. O. Shiryaeva, Zh. Tekh. Fiz. **61**(3), 19 (1991) [Sov. Phys. Tech. Phys. **36**, 258 (1991)].

[8] V. A. Dyachuk and V. M. Muchnik, Dokl. Akad. Nauk SSSR **248**, 60 (1979).

[9] A. I. Grigor'ev and S. O. Shiryaeva, Zh. Tekh. Fiz. **59**(5), 6 (1989) [Sov. Phys. Tech. Phys. **34**, 502 (1989)].

[10] A. I. Grigor'ev and S. O. Shiryaeva, Physica Scripta **54**, 660 (1996).

Translated by R. M. Durham

Charge properties of aluminum oxide layers synthesized by molecular layering

S. G. Sazonov, Z. N. Zuluev, V. E. Drozd, and I. O. Nikiforova

Physical Research Institute, St. Petersburg State University
(Submitted January 21, 1998)
Pis'ma Zh. Tekh. Fiz. **24**, 58–63 (July 12, 1998)

An investigation was made of the charge and conducting properties of layers of insulator obtained by molecular layering in Si–Al_2O_3–Al structures. No charge trapping in the insulator is observed at 77 K when depleting voltages are applied to the structure. © *1998 American Institute of Physics.* [S1063-7850(98)01107-0]

As the variety of semiconductors used in microelectronics increases, there is a need to obtain high-quality insulating layers at relatively low temperatures to prevent degradation of the semiconductor surface. Layers of Al_2O_3 synthesized by molecular layering are potentially useful from this point of view.[1,2]

The aim of the present paper is to make a complex study of the electrophysical properties of metal–insulator–semiconductor (MIS) structures with an Al_2O_3 insulator obtained by molecular layering, using the capacitance–voltage and current–voltage characteristics.

For the experiments we used KÉF-5 *n*-Si (111) wafers and KDB-10 *p*-Si(100) wafers. Silicon was chosen as the substrate because the characteristics of a silicon–insulator interface depend only weakly on the synthesis temperature of the insulator. In addition, the pretreatment stage of the substrate surface has been developed most thoroughly for silicon. As a result, the MIS structure had a fairly high-quality interface (the surface state density was $\sim 5 \times 10^{11}$ cm^{-2} eV^{-1}) which allowed us to study the electrophysical properties of the insulator and their dependence on the synthesis conditions.[3]

The samples were synthesized in the temperature range $T_s = 150$–310 °C using trimethyl aluminum and nitric oxide (NO_2). Aluminum contacts of 0.24 mm^2 were deposited by thermal deposition in vacuum.

The spread of the insulator thickness measured using an LÉF-3 ellipsometer over a 60 mm diameter substrate was less than 2%. The results of an investigation of the transmission spectra of the films show that the band gap does not exceed 6 eV. The composition of the synthesized films from ESCA data corresponds to Al_2O_3 stoichiometry (the atomic ratio of the elements is Al/O=0.7). Electron diffraction analyses revealed that the films are amorphous. The electrical strength of a layer of thickness $d = 100$ nm was 7.5 MV/cm.

The current–voltage characteristics of these structures were linear when plotted as $\log J$ vs $E^{1/2}$. The depth of a Poole–Frenkel center is 0.4 eV but the conduction mechanism cannot be identified specifically because of the small range of measurable current (three or four orders of magnitude). Layers of Al_2O_3 with $T_s = 150$ °C have the highest resistivity and breakdown field strength. The low-frequency

permittivity of the Al_2O_3 layers decreases with increasing T_s from 7.0 to 5.0.

For all the samples, the initial fixed charge Q_{FB}^0 in the insulator was negative and decreased as the synthesis temperature increased. The capacitance–voltage characteristics exhibit an injection type of hysteresis.

The experimental dependences of the charge Q_{FB} trapped during the action of the field, the integrated density of surface states, and the hysteresis of the capacitance–voltage characteristic as a function of the polarizing field $E_p = V_p/d$ (V_p is the voltage applied to the metal electrode for 1 min) are complicated for Si–Al_2O_3–Al structures with different parameters.

With a positive gate voltage, the negative charge in the insulator of *n*-Si structures increases with increasing V_p (Fig. 1a) as a result of trapping of electrons injected from the semiconductor into the insulator.

Since structurally different materials may be formed at different temperatures T_s, the observed dependence of Q_{FB} on T_s for $V_p > 0$ may be attributed to an increase in the barrier for the electrons at the semiconductor–insulator contact as T_s increases.

The behavior of $Q_{FB}(E_p)$ for $E_p < 0$ is qualitatively different (the polarity of the trapped charge is reversed as the field intensity increases) and depends strongly on T_s. The nonmonotonic behavior of $Q_{FB}(E_p)$ may be attributed to bipolar injection of carriers in the Al_2O_3.

Annealing the samples immediately after deposition of the insulator reduced the trapped charge.

The dependence of Q_{FB} on the polarizing strength E_p differs qualitatively at 300 and 77 K because for $E_p < 0$ and $T = 77$ K the value of Q_{FB} varies very little down to $E_p \sim -7$ MV/cm, after which the initial negative charge shows a slight decrease (Fig. 1b). The absence of a negative charge buildup in the *n*-type Si structure (as at $T = 300$ K in strong fields $E_p < 0$) can be attributed to the temperature dependence of the level of electron injection from the metal electrode into the insulator. As a result, at 77 K the injection current is so small that over the polarization time, the electrons captured by traps do not have time to create any appreciable charge. However, the low concentration of holes (minority carriers) and the longer times taken to form the inversion layer in *n*-Si at this temperature, have the result
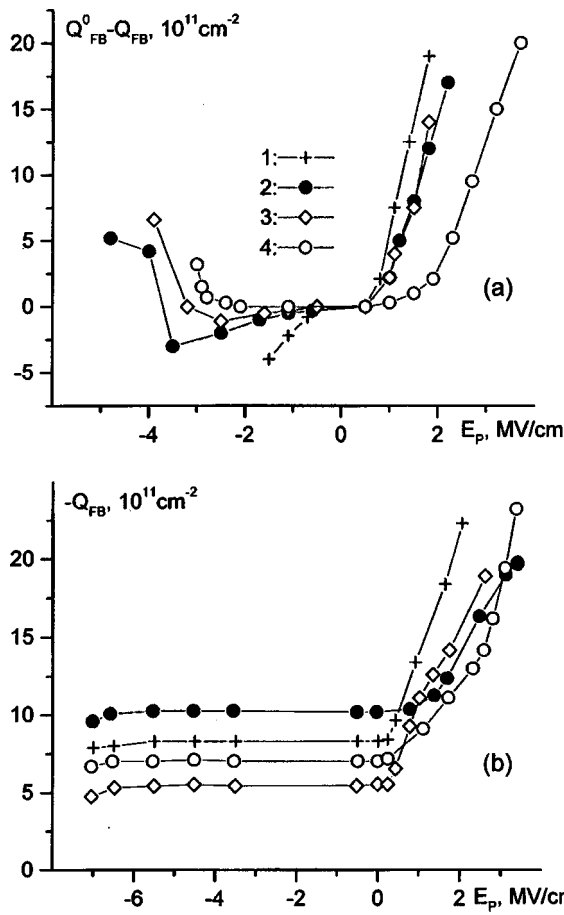
FIG. 1. Trapped charge density versus field strength in n–Si–Al$_2$O$_3$–Al structure at $T = 300$ K (a) and 77 K (b). T_s: *1*—150 °C; *2*—200 °C; *3*—240 °C; *4*—310 °C.

FIG. 2. Trapped charge density versus field strength (a) and polarization time (b) in p–Si–Al$_2$O$_3$–Al structure: *1*—$T = 77$ K, $Q_{FB}^0 = -1 \times 10^{11}$ cm^{-2}; *2*—$T = 300$ K, $Q_{FB}^0 = -6 \times 10^{11}$ cm^{-2}; *3*—$T = 77$ K, $V_p = 30$ V.

that no positive charge builds up for $V_p < 0$. This factor also explains the absence of electron trapping in the p-Si structure at positive voltages (Fig. 2a). An increase in the polarization time leads to a buildup of charge in the insulator (Fig. 2b). At negative gate voltages, positive charge accumulates in this structure as a result of trapping of holes injected from the semiconductor into the insulator and at $V_p > 0$ and $T = 300$ K, the negative charge increases as a result of injection of electrons from the metal.

Thus, although traps are present in the bulk of the insulator, at fairly low temperature no charge trapping is observed in the insulator over a fairly long period (tens of minutes) at depleting polarizing voltages (up to breakdown levels) as a result of the low level of carrier injection into the insulator. This opens up additional possibilities for investig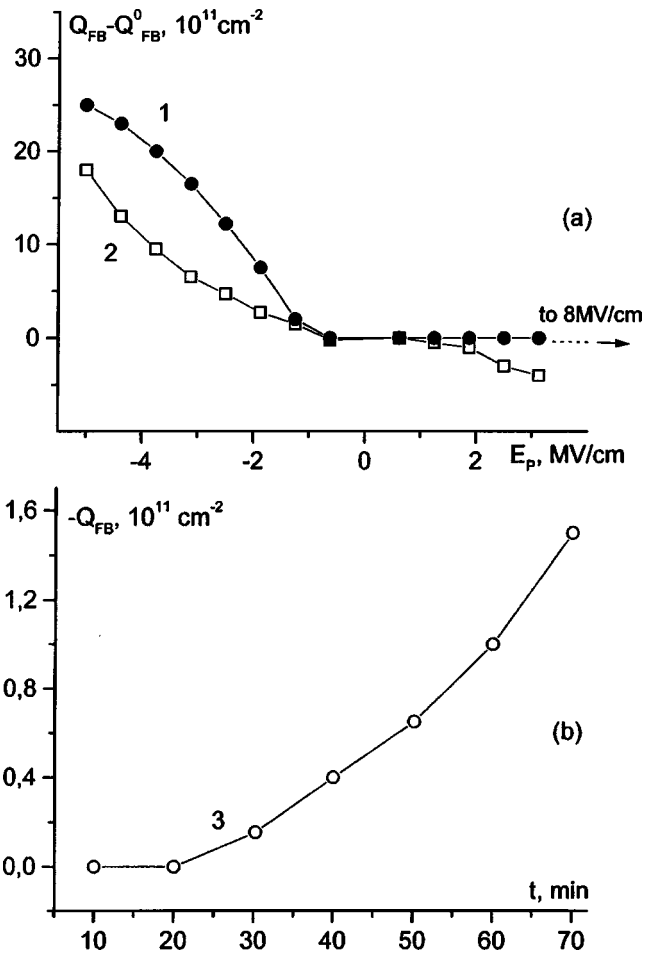ating insulating heterostructures obtained by molecular layering (insulating layers imbedded in the bulk of the Al$_2$O$_3$) since the charge properties of these structures will only be determined by the characteristics of the embedded layers and their interfaces.

[1] V. B. Aleskovski and V. E. Drozd, Acta Polytech. Scand. **195**, 155 (1990).
[2] V. E. Drozd, A. P. Baraban, and I. O. Nikiforova, Appl. Surf. Sci. **83**, 583 (1994).
[3] S. G. Sazonov, V. E. Drozd, Z. N. Zuluev, and O. E. Nikiforova, in *Proceedings of the International Scientific-Technical Conference "Dielectrics-97,"* St. Petersburg, 1997 [in Russian], p. 66–68.

Translated by R. M. Durham

Diffraction of low-energy electrons at a rippled surface

S. A. Knyazev and V. E. Korsukov

A. F. Ioffe Physicotechnical Institute, Russian Academy of Sciences, St. Petersburg

An analysis is made of a kinematic model of the scattering of low-energy electrons at a one-dimensional periodic toothed structure simulating a rippled surface. Calculations of the intensity profiles of the diffraction peaks are made for periodic systems of identical symmetrical triangular teeth with a variable number of atoms on each generatrix of the tooth and various angles of inclination of the generatrices to the horizontal. The main effect observed as a result of scattering at a periodic toothed structure involves broadening or splitting of the diffraction peaks compared with the diffraction patterns from a smooth chain of atoms. © *1998 American Institute of Physics.* [S1063-7850(98)01207-5]

In low-energy electron diffraction analyses of the transformation of the surface structure of Ge(111) and mica during stretching and bending of the crystals, we observed broadening, which was quasireversible with loading, and splitting of the peaks in the diffraction patterns.[1,2] It was shown by high-energy electron diffraction and scanning tunneling microscopy[1,3] that under deformation, the single-crystal surface is transformed to the polycrystalline and nanocrystalline state. This is accompanied by the appearance of a rough surface relief (protrusions and indentations of varying scale are observed, ranging from atomic terraces to extended hillocks and indentations with depths between 10 and 1000 nm). Thus, the process of mechanical loading of crystals may be viewed as involving the formation of shallow sections with different orientations to one another, and as one variant, the formation of a rippled surface structure.

This gives rise to the problem of diffraction of low-energy electrons at a periodic surface structure. The aim of the present study is to determine how the transition from a smooth to a rippled surface influences the intensity profile of the diffraction peaks on the low-energy diffraction patterns.

For a rippled surface the diffraction conditions in the direction of the grooves are the same as those for a planar surface. Thus, diffraction at a rippled surface—the intensity of the electron scattering at this structure—may be simulated by the scattering at a one-dimensional atomic chain having the same profile as the rippled surface and the angular distribution of the intensity need only be considered in the direction of this chain. The intensity of the diffraction peaks was calculated using a kinematic approximation for a one-dimensional periodic toothed structure with triangular symmetric teeth which gives

$$I = \left| \frac{\exp i(2Na\pi/\lambda(\cos\varphi\,\sin(\theta) + \sin\varphi(\cos(\theta)+1))) - 1}{\exp i(2a\pi/\lambda(\cos\varphi\,\sin(\theta) + \sin\varphi(\cos(\theta)+1))) - 1} \right.$$
$$\left. + \frac{\exp i(2(N-1)a\pi/\lambda(\cos\varphi\,\sin(\theta) - \sin\varphi(\cos(\theta)+1))) - 1}{\exp i(2a\pi/\lambda(\cos\varphi\,\sin(\theta) - \sin\varphi(\cos(\theta)+1))) - 1} - 1 \right|^2$$
$$\times |(\sin(2M(N-1)a\pi/\lambda\,\cos\varphi\,\sin(\theta)))/(\sin 2(N-1)a\pi/\lambda\,\cos\varphi\,\sin(\theta))|^2 .$$

The number of atoms N on one generatrix is the number of scattering atoms, M is the number of teeth, a is the distance between neighboring atoms, φ is the angle of inclination of the generatrix to the horizontal, and θ is the scattering angle.

Figure 1 shows how the angular dependence of the intensity of the diffraction peaks $I(\theta)$ changes in the transition from a smooth horizontal chain of atoms (Fig. 1a) to a toothed structure with few atoms per generatrix ($N=4$) and a comparatively large number of teeth ($M=20$) (Fig. 1b), and then to a structure with many atoms per generatrix ($N=20$) and few teeth ($M=4$) (Fig. 1c). It can be seen that

the transition to structures with more teeth substantially changes the diffraction pattern. For the first structure, this pattern is a set of isolated peaks and for the second, it comprises a set of peaks split into various sub-peaks.

In order to explain the nature of the diffraction peaks observed for scattering at a toothed structure, we constructed a series of $I(\theta)$ graphs for various angles of inclination of the tooth generatrices. For a small angle $\varphi(1°)$ the diffraction pattern for $N=4$ and $M=20$ contains peaks consistent with the diffraction from a smooth horizontal chain. An increase in the number of atoms per generatrix to 20 signifi-
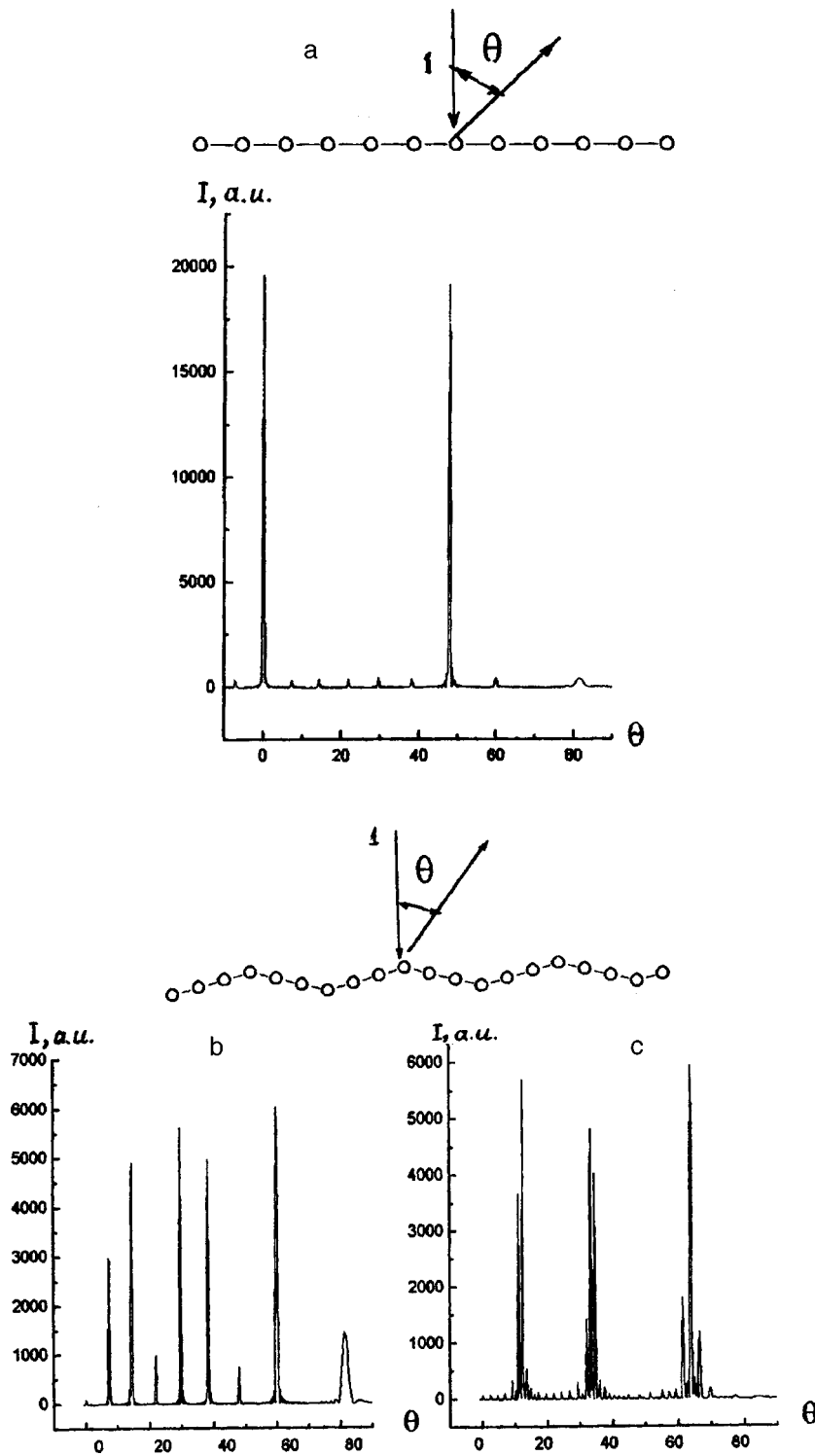
FIG. 1. Angular distribution of the intensity for diffraction at a one-dimensional chain, $E_r = 120$ eV, 1—electron beam; a—horizontal atomic chain $M \times M = 80$; b—toothed structure, $\varphi = 6$, $N = 4$, $M = 20$; c—toothed structure, $\varphi = 6$, $N = 20$, $M = 4$.

cantly transforms the diffraction pattern: the peaks become split, their intensity drops appreciably, and the diffraction pattern varies abruptly with the electron energy. As a result of changing from $\varphi = 6°$ to $\varphi = 13°$ ($N = 4$, $M = 20$), the structure of the diffraction pattern becomes sparser, the angular position of the diffractions peaks shifts, these peaks separate into individual groups, and their intensity varies rapidly with E_p. As the number of atoms per tooth generatrix increases ($N = 20$, $M = 4$), the peak corresponding to specu-

lar reflection from the generatrices becomes more clearly defined.

A series of $I(\theta)$ graphs was constructed as a function of the number of teeth. Figure 2 gives the diffraction pattern obtained for diffraction at one, two, and twenty teeth ($N = 4$, $\varphi = 6°$, $Ep = 120$ eV). All the curves were normalized relative to the structure with one tooth. The results clearly show that the diffraction structure is formed by scattering at one tooth and increasing the number of teeth in the
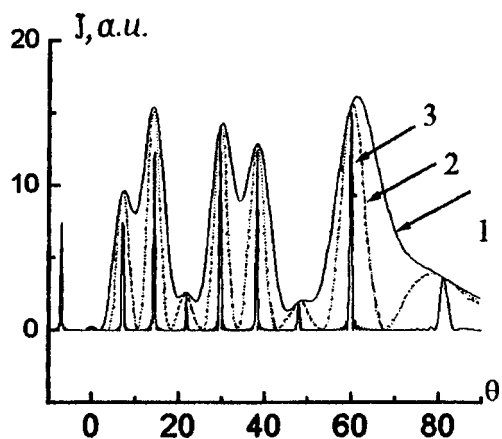
FIG. 2. Angular distribution of intensity for various numbers of teeth. All the curves are normalized to one tooth. *1*—one tooth, *2*—two teeth, and *3*—twenty teeth.

periodic structure to twenty merely reduces the angular width of the diffraction peaks. Similar results were obtained for other values of N and φ.

In order to identify the nature of the diffraction peaks formed by scattering at one tooth, we calculated $I(\theta)$ for various numbers of atoms per generatrix. The calculations showed that changing N from two to four appreciably alters the diffraction pattern. An increase in the number of atoms on the generatrix ($N = 10$–20–50) leads to the formation of a stable angular distribution of diffraction peaks. A compari-

son between the angular position of these peaks and the position of the diffraction peaks from a smooth chain of atoms positioned at angles $-\varphi$ and $+\varphi$ to the horizontal (in accordance with the generatrices of the tooth) showed that the angular position of the peaks for diffraction at one tooth may be ascribed to the (00), (10), and (01) peaks obtained by diffraction from two smooth atomic chains inclined to the horizontal at angles similar to the generatrices of the tooth.

This set of calculations shows that even a simple one-dimensional kinematic model of electron scattering at a toothed surface predicts an appreciable transformation of the low-energy diffraction patterns from a rippled surface compared with those for a smooth surface. These changes mainly involve broadening and splitting of the diffraction peaks. For toothed structures containing a considerable number of atoms per generatrix, the angular broadening of the peaks can be estimated as the angle of inclination of the tooth generatrix to the horizontal. These results can be used to estimate the parameters of rippled structures formed as a result of the deformation of single crystals from the changes in the low-energy electron diffraction patterns from the loaded surface.

[1] V. E. Korsukov, S. A. Knyazev, A. S. Luk'yanenko *et al.*, Fiz. Tverd. Tela (St. Petersburg) **38**, 113 (1996) [Phys. Solid State **38**, 60 (1996)].
[2] S. A. Knyazev, V. E. Korsukov, and B. A. Obidov, Fiz. Tverd. Tela (St. Petersburg) **36**, 1315 (1994) [Phys. Solid State **36**, 718 (1994)].
[3] S. N. Zhurkov, V. E. Korsukov, A. S. Luk'yanenko, B. A. Obidov, and A. P. Smirnov, JETP Lett. **51**, 370 (1990).

Translated by R. M. Durham

Criteria for the existence of generalized surface spin waves

S. V. Tarasenko

A. A. Galkin Physicotechnical Institute, Donetsk
(Submitted April 17, 1997; resubmitted February 25, 1998)
Pis'ma Zh. Tekh. Fiz. **24**, 70–75 (July 12, 1998)

A criterion for the existence of generalized surface spin waves is proposed on the basis of an analysis of the dipole-exchange surface spin dynamics of a tangentially magnetized, semibounded, easy-axis antiferromagnet. © *1998 American Institute of Physics.*
[S1063-7850(98)01307-X]

For a normally magnetized, semibounded, easy-axis ferromagnet (antiferromagnet) it was shown in Refs. 1 and 2 that hybridization of the magnetic dipole and exchange mechanisms for dispersion of the magnetic vibrations in a bounded crystal may result in the formation of a dipole-exchange, generalized surface (quasi-surface) spin wave, propagating along the boundary of the magnet, which is not achieved in the pure-exchange or in the magnetostatic approximation. So far however, the criterion which the dipole-exchange dynamics of an unbounded magnet must satisfy for a generalized surface spin wave to form at its boundary remains unclear.

In the present paper an analysis is made of the conditions for the formation of dipole-exchange surface spin waves in a semibounded easy-axis antiferromagnet (Cr_2O_3) and it is shown for the first time that the criterion for the existence of a generalized surface spin wave may be the presence of sections of maximum negative curvature on the isofrequency surface of the normal spin vibrations of an unbounded magnet and their specific spatial orientation relative to the normal to the surface of the magnet and a certain direction of propagation. By way of example, an analysis is made of a two-sublattice ($\mathbf{M}_{1,2}$ is the sublattice magnetization, $|\mathbf{M}_1|=|\mathbf{M}_2| = M_0$) model of an easy-axis antiferromagnet ($0Z$ is the easy axis). In this case, the density of the thermodynamic potential W of the easy-axis antiferromagnet may be represented in terms of the vectors of ferromagnetism $\mathbf{m}$ and antiferromagnetism $\mathbf{l}$ in the form

$$W=\frac{\delta}{2}\mathbf{m}^2+\frac{\alpha}{2}(\boldsymbol{\nabla}\mathbf{l})^2-\frac{\beta}{2}l_z^2-\mathbf{M}(\mathbf{H}+\mathbf{H}_m),$$

$$\mathbf{m}=\frac{\mathbf{M_1}+\mathbf{M_2}}{2M_0}, \quad \mathbf{l}=\frac{\mathbf{M_1}-\mathbf{M_2}}{2M_0}, \tag{1}$$

where δ, α, and $\beta > 0$ are the constants of homogeneous exchange, inhomogeneous exchange, and uniaxial anisotropy, respectively, $\mathbf{H} \parallel OY$ is the external magnetic field and $\mathbf{H}_m$ is the field induced by magnetic-dipole interaction. The dipole exchange dynamics of this model of a magnetic medium is known to be described by a closed system of equations consisting of the Landau–Lifshitz equations for the vectors $\mathbf{m}$ and $\mathbf{l}$ and the magnetostatics equations. Assuming that the easy-axis antiferromagnetic medium occupies the half-space $x < 0$ ($\mathbf{n} \parallel OX \perp \mathbf{H}$), this system of dynamic equa-

tions should be supplemented by the corresponding boundary conditions. If the spins at the surface of the easy-axis antiferromagnet are free ($\widetilde{\mathbf{m}}, \widetilde{\mathbf{l}}$ are small deviations of the vectors $\mathbf{m}$ and $\mathbf{l}$ from their equilibrium orientation), the system of boundary conditions which must be satisfied by a dipole-exchange surface spin wave localized at the interface between the magnetic and nonmagnetic media ($x=0$) may be represented in the form

$$\frac{\partial \widetilde{\mathbf{m}}}{\partial x}=\frac{\partial \widetilde{\mathbf{l}}}{\partial x}=0; \quad \mathbf{B}_m\mathbf{n}=\mathbf{B}\mathbf{n}; \quad [\mathbf{H}_m\mathbf{n}]=[\mathbf{H}\mathbf{n}];$$

$$|\widetilde{\mathbf{m}}|, \quad \phi_m|\widetilde{\mathbf{l}}|\to 0 \quad \text{for } x\to-\infty;$$

$$\phi\to 0 \quad \text{for } x\to\infty, \tag{2}$$

where $\mathbf{B}_m$, $\mathbf{H}_m$, ϕ_m ($\mathbf{B},\mathbf{H},\phi$) are respectively the magnetic induction vector, the magnetic field vector, and the magnetostatic potential in a magnetic (nonmagnetic) medium. It is well-known that in this model of an easy-axis antiferromagnet, neglecting the finite dimensions of a real magnetic sample, the antiferromagnetic resonance spectrum consists of two branches which, according to their mode of excitation by the microwave field $\mathbf{h}$, can be divided into a quasi-ferromagnetic mode (ω_F), linearly excited and with $\mathbf{h}\perp\mathbf{H}$, and a quasi-antiferromagnetic mode (ω_{AF}) linearly related to $\mathbf{h}\parallel\mathbf{H}$. For simplicity and conciseness, we shall subsequently assume that the external field $\mathbf{H}$ is such that

$$\omega_F \gg \omega_{AF}. \tag{3}$$

In this case, the indirect coupling of these modes of an unbounded crystal via the magnetic-dipole interaction field can be neglected and the surface dipole-exchange spin dynamics of a semibounded easy-axis antiferromagnetic can be investigated merely in terms of the quasi-antiferromagnetic mode of the spin-wave excitation spectrum ($|\widetilde{l}_{x,z}|,|\widetilde{m}_y|$). Then the corresponding characteristic equation determining the wave vector component of the magnetic vibrations $\mathbf{k}(k_x)$ normal to the surface, as a function of the experimentally determined frequencies ω, $k_\perp$, and ψ ($\cos\psi=k_y/k_\perp$, $k_\perp$ is the wave vector component of the spin vibrations tangential to the interface of the media), may be expressed in the form
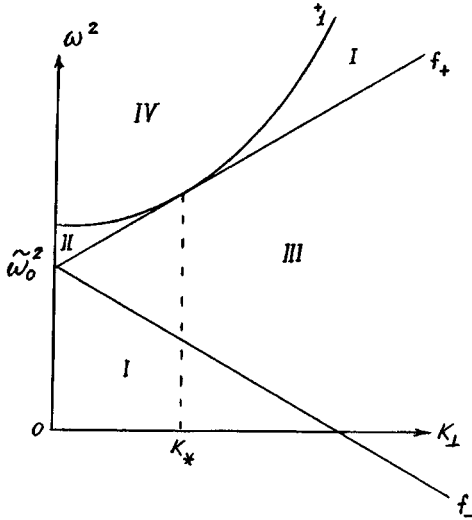
FIG. 1. Possible modes of dipole-exchange spin-wave excitations in a bounded easy-axis antiferromagnet with $\mathbf{n} \| OX$, $\mathbf{H} \| OY$, $\mathbf{l} \| OZ$ as a function of the frequency ω and the wave vector component tangent to the magnetic surface $k_\perp$: $f_1 = \widetilde{\omega}_0^2 + \widetilde{R} + c^2 k_\perp^2$, $f_\pm = \widetilde{\omega}_0^2 \pm 2\sqrt{\widetilde{R}} c k_\perp$; $c k_* = \sqrt{\widetilde{R}}$.

$$k_x^4 + A k_x^2 + B = 0; \quad A = 2k_\perp^2 - \frac{\omega^2 - \widetilde{\omega}_0^2}{c^2};$$

$$B = k_\perp^2 \left(\frac{c^2 k_\perp^2 + \widetilde{R} - \omega^2 + \widetilde{\omega}_0^2}{c^2} \right);$$

$$\widetilde{R} = \omega_0^2 \widetilde{\epsilon}; \quad \widetilde{\omega}_0^2 = \omega_0^2 + \widetilde{\epsilon} c^2 k_\perp^2, \tag{4}$$

where $\widetilde{R} = \omega_0^2 \widetilde{\epsilon}$; *here* $\widetilde{\epsilon} = (4\pi M_0 / H_E) \cos^2 \psi$ and $\omega_0^2 \approx g^2 (2 H_E H_A - H_A H^2 / 2 H_E)$; $c^2 = g^2 2 H_E (1 - H^2 / (2H_E)^2) \alpha M_0$, g is the gyromagnetic ratio, H_E and H_A are the fields of intersublattice exchange and uniaxial anisotropy, respectively, and $H_E \gg H_A$. Since relation (4) is a biquadratic equation for k_x, it can be confirmed that all possible modes of dipole-exchange linear magnetic vibrations propagating in the plane of an easy-axis antiferromagnetic film in the limit (3) are bipartial spin-wave excitations. Thus, the amplitude structure of the small vibrations of the magnetostatic potential ϕ_m (for an easy-axis antiferromagnet) along the normal to the interface is given in the form

$$\phi_m = A_1 \exp(i\omega t - q_1 x) + A_2 \exp(i\omega t - q_2 x),$$

$$q^2 \equiv -k_x^2, \tag{5}$$

where $A_{1,2}$ are arbitrary constants determined from the boundary conditions

Formulas (4) and (5) can be used to classify the possible modes propagating along the surface of an easy-axis antiferromagnet with $\mathbf{n} \| OX$ as a function of their conditions of localization near the interface between the magnetic and nonmagnetic media, which are determined from Eq. (4) by the character of the roots q_j^2 ($j = 1,2$) on the plane of the external parameters ω and $k_\perp$ for given ψ (see Fig. 1). It follows from Eqs. (4) and (5) that in the region of existence of dipole-exchange surface spin waves (region I) or volume spin waves (region II) on the plane of the parameters ω, $k_\perp$, and ψ, the inequalities $q_{1,2}^2 > 0$ or $q_{1,2}^2 < 0$, respectively, are satis-

fied. In the regions of existence of dipole-exchange generalized surface spin waves (region III) and evanescent surface spin waves (region IV), the conditions $q_1^2 = (q_2^2)^*$ and $q_1^2 > 0$, $q_2^2 < 0$, respectively, hold (''*'' indicates complex conjugation). The condition for nontrivial solvability of the system (2), (4), and (5) determines the implicit form of the dispersion law for the exchange-dipole surface spin waves propagating along the free boundary of an easy-axis antiferromagnet with $\mathbf{H} \perp \mathbf{n} \perp \mathbf{l}$. In the long-wavelength limit with the additional constraint $c^2 \gamma \ll \widetilde{R}$, this dispersion relation can be obtained in the explicit form

$$\omega^2 = \widetilde{\omega}_0^2 + c^2 (k_\perp^2 + \gamma(k_\perp)); \quad \gamma(k_\perp \to 0) \to 0;$$

$$\gamma(k_\perp) = 2k_\perp \sqrt{\frac{\widetilde{R}}{c^2} + k_\perp^2}$$

$$- \left(\sqrt{k_\perp \sqrt{\frac{\widetilde{R}}{c^2} + k_\perp^2} + \frac{\widetilde{R}}{4c^2}} - \frac{1}{2} \sqrt{\frac{\widetilde{R}}{c^2}} \right)^2. \tag{6}$$

Comparing formula (6) with the regions of existence of the possible types of exchange-dipole modes of spin-wave excitations shown in Fig. 1, it can be concluded that the surface spin wave (6) for $k_\perp \ll k_*$ is a generalized surface spin wave. Now for fixed ψ formula (4) is used to analyze the change in the curvature of the isofrequency surface $K(\theta)(\cos\theta = k_x / k, k^2 = k_x^2 + k_\perp^2)$ of the quasi-antiferromagnetic mode of the spectrum of normal spin vibrations of an unbounded antiferromagnet (4) as a function of the external parameter ω. For this purpose an analysis is made of the shape of the curve obtained by intersection of the isofrequency surface with the plane in which the vectors $\mathbf{n}$ and $\mathbf{k}_\perp$ lie. This analysis shows that for $\omega^2 < \omega_0^2 + \widetilde{R}(2 + \widetilde{\epsilon})$, $\theta = 0, \pi$ in the direction of propagation of the generalized surface spin wave being studied, sections with maximum negative curvature $K(\theta)$ form on this curve:

$$K(\theta = 0, \pi) < 0. \tag{7}$$

It is easily confirmed that for the dipole-exchange generalized surface spin waves studied in Refs. 1 and 2, a similar relation is found between the conditions for the existence of a generalized surface spin wave and the sections of maximum negative curvature on the curve obtained by intersection of the isofrequency surface of the normal spin vibration of an unbounded magnet with the plane in which the vectors $\mathbf{n}$ and $\mathbf{k}_\perp$ lie. Thus, this criterion can be applied to specify the conditions required for the formation of a generalized surface spin wave of the dipole-exchange or elasto-exchange type by calculating the dipole-exchange (elasto-exchange) magnon spectrum of an unbounded magnet.

We have so far considered the case with $H_y \neq 0$ in which condition (3) is satisfied between the antiferromagnetic resonance frequencies of an unbounded ferromagnet. We shall now assume that the condition opposite to (3) is satisfied between the quasi-ferromagnetic and quasi-antiferromagnetic branches of the antiferromagnetic resonance spectrum of this magnet, which is possible for $\mathbf{H} \| OX(\mathbf{l} \| OZ)$. The calculations show that if the magnetic-dipole mechanism of interaction between the quasi-ferromagnetic and quasi-

antiferromagnetic modes of the spectrum of an easy-axis antiferromagnet is neglected for the same relative orientations of the vectors $\mathbf{n}, \mathbf{l}, \mathbf{k}_\perp$, the dipole-exchange generalized surface spin wave determined above is as before the result of the normal quasi-antiferromagnetic mode of an unbounded crystal being localized near the surface of the magnet. Now, however, its spectrum (6) will lie at a higher frequency than that of the quasi-ferromagnetic mode of antiferromagnetic resonance and hence the surface spin wave (6) will now be an evanescent generalized spin wave since it generates quasi-ferromagnetic bulk spin waves as it propagates. Thus, depending on whether the low- or high-frequency mode of the spectrum of normal bulk magnons of an unbounded magnet is localized, criterion (7) is the condition for the existence of generalized surface spin waves or an evanescent generalized surface spin wave, respectively.

For a metallized magnetic surface or completely anchored spins dipole-exchange generalized surface spin waves of this type do not occur.

[1] R. E. De Wames and T. J. Wolfram, J. Appl. Phys. **41**, 987 (1970).
[2] B. A. Ivanov, V. F. Lapchenko, and A. L. Sukstanskiĭ, Fiz. Tverd. Tela (Leningrad) **27**, 173 (1985) [Sov. Phys. Solid State **27**, 101 (1985)].

Translated by R. M. Durham

Use of magnetic field screening by high-temperature superconducting films to switch microwave signals

T. M. Burbaev, S. I. Krasnosvobodtsev, V. A. Kurbatov, N. P. Malakshinov,
V. S. Nozdrin, and N. A. Penin

P. N. Lebedev Physics Institute, Russian Academy of Sciences, Moscow
(Submitted September 18, 1997)
Pis'ma Zh. Tekh. Fiz. **24**, 76–81 (July 12, 1998)

The efficiency with which YBCO films screen an alternating magnetic field near the superconducting transition was measured. In the decimeter range measurements were made of the characteristics of a switch whose operating principle was based on the change in the screening of an alternating magnetic field by a superconducting transition. © *1998 American Institute of Physics.* [S1063-7850(98)01407-4]

The use of a superconducting transition to switch microwave signals usually implies a device with thin superconducting bridges whose normal-state resistance is sufficiently high to ensure that the switching element has a high quality factor and to facilitate current control of the switch.[1] Nevertheless, the normal-state resistance of the bridges is generally less than 1000 Ω, which leads to appreciable ($\geq 20\%$) active losses. This limits the switchable power and thus the range of application of these switches. However, there is another method of using a superconducting transition to switch signals which can almost eliminate losses in the switching element over a fairly wide frequency range; this involves using the screening properties of a superconducting plate. In this case, the switching coefficient will be determined by the difference in the screening properties in the superconducting and normal states. In the first case, the screening is at a maximum while in the second, it is determined by the conductivity and by the signal frequency.

We first note that the screening of an electromagnetic wave incident normally on a superconducting plate will be efficient in the normal state, even for very thin films with $d < 1000$ Å. Here, the condition for weak absorption is $d \ll (2/z_0 \sigma_0)$, where $z_0 = 377$ Ω and σ_0 is the bulk conductivity of the sample at low frequencies. This condition cannot be satisfied for superconductors.

For the screening of an alternating magnetic field directed perpendicular to the plane of a superconducting plate, the situation is different.

The transmission of the magnetic field by the sample in the normal state is determined by the relation between the sample thickness and the depth of penetration $d_p = (2/\mu \mu_0 \omega \sigma_0)^{1/2}$. This difference is attributed to the boundary conditions at the surface where, in this case, the magnetic field has an antinode while the electric field has a node.[2] The condition $d \ll d_p$ yields the inequality $f \ll (\pi d^2 z_0^2 \varepsilon_0)^{-1}$, which determines the frequency range where the superconducting sample in the normal state will be almost transparent to the alternating magnetic field. For our high-temperature superconducting films an estimate gives $f \ll 1.7 \times 10^{13}$ Hz.

Our prototype switch consisted of a strip line fitted with magnetic coupling loops which was screened by a high-temperature superconducting film. The switch is shown schematically in Fig. 1 which gives a block diagram of the measuring apparatus. The device was designed to be inserted in a portable helium Dewar. The temperature of the sample was measured with a thermocouple. Measurements of the transmission coefficient $K_T = (S_1/S_2)$ and the switching coefficient $K_s = (K_{TN}/K_{TS})$ were made in the frequency range 0.01–300 MHz using SMV6.1 and SMV8.5 measuring detectors. Here S_1 and S_2 are the signals on entry to and at the exit from the switching device and K_{TN} and K_{TS} are the transmission coefficients in the normal and superconducting state of the high-temperature superconducting film, respectively. The signal generator was either the built-in calibration oscillator of the measuring detector or, when higher powers were required, a G4-37A generator.

Figure 1 shows the system used to measure the switching coefficient with the switch controlled by current pulses. For measurements of the transmission coefficient, the signal from the measuring detector *4* was fed directly to the *Y* input of an automatic plotter *7*. Measurements of the transmission coefficient in the absence of the superconducting film K_0 and with the coupling loop screened by copper foil of the same area as the high-temperature superconducting film K_{Cu} at frequencies ≥ 10 MHz, at which the depth of penetration of the copper is substantially less than the thickness of the foil, showed that the maximum switching coefficient $K_{S\,max} = (K_0/K_{Cu})$ is 12 dB. This value is determined by the design characteristics and is mainly limited by ''leakage'' of magnetic field beneath the screen through the insulating substrate, which is sandwiched between the superconducting film and the coupling loop.

We investigated YBCO films 1500 Å thick fabricated by laser deposition[3] on strontium titanate substrates. In the frequency range used the electrical properties of the substrate influenced the results negligibly, no difference being observed in the transmission coefficient with the film in the normal state and without the film.
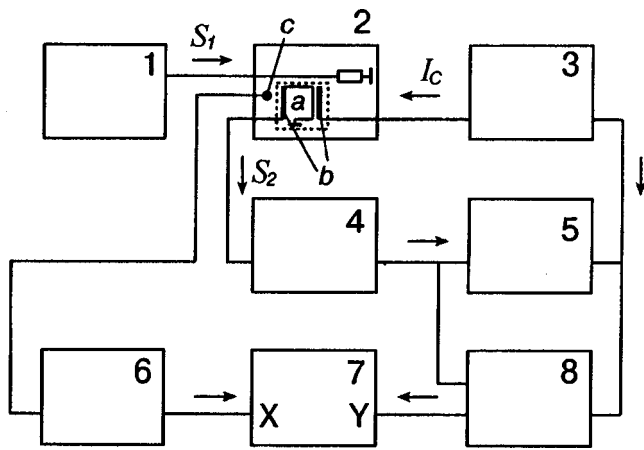
FIG. 1. Schematic of apparatus: *1*—rf generator, *2*—switching device, *a*—superconducting film with current contacts *b*, *c*—thermocouple, *3*—control current pulse generator, *4*—measuring detector, *5*—oscilloscope, *6*—dc microvoltmeter, *7*—automatic xy plotter, and *8*—synchronous pulse voltmeter.

FIG. 3. Switching coefficient versus temperature at 100 MHz for control currents: *1*—1.6 A, *2*—0.8 A, *3*—0.4 A, *4*—0.2 A, *5*—0.08 A. The dashed curve gives the temperature dependence of the transmission coefficient.

Figure 2 gives temperature dependences of the relative transmission coefficient measured at different frequencies. The absolute value of K_T increases with the square of the frequency and at 100 MHz in the open (normal) state of the superconducting screen is -30 dB. Also plotted is the measured dependence of the dc resistance of the film.

It can be seen that as the measurement frequency increases, the onset of screening, caused by the appearance of the superconducting phase with decreasing temperature, is shifted toward higher temperatures. At the same time, the reduction in the dc resistance with decreasing temperature begins at temperatures higher than that at which magnetic field screening appears.

The dependences observed for different types of films exhibit different behavior of the screening curves at different frequencies. For YBCO films the slope of the magnetic field transmission increases with decreasing frequency, whereas for BiSrCaCuO films and single crystals, the dependences are almost independent of frequency—the curves are shifted in temperature without any significant change in profile.[4]
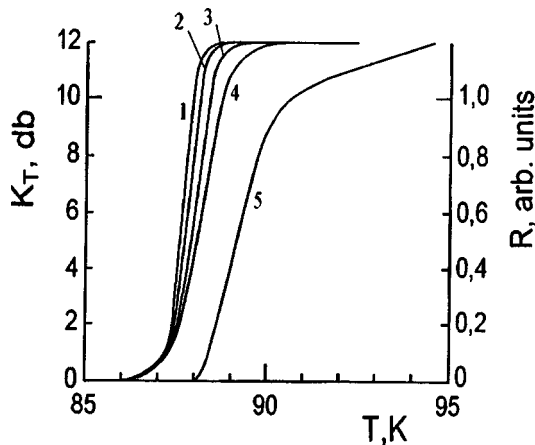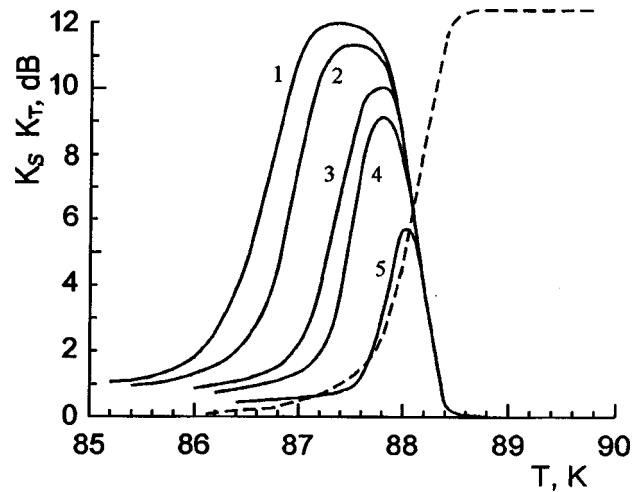

FIG. 2. Temperature dependences of the transmission coefficient at frequencies: *1*—1 MHz, *2*—30 MHz, *3*—100 MHz, *4*—300 MHz, *5*—dc resistance of film.

Our ac measurements of the temperature dependence of the electrical conductivity of the films revealed no significant differences in the curves obtained at different measurement frequencies, which could explain the magnetic field screening results. We thus postulate that the observed frequency shift effect is attributable to the response time required for the alternating magnetic field to polarize the thermally excited vortices which form in quasi-two-dimensional superconductors[5] and combine to form pairs rotating in opposite directions at temperatures slightly below the superconducting transition.

Figure 3 gives the temperature dependence of the switching coefficient measured at a frequency of 100 MHz for a YBCO film switch. Also plotted is the temperature dependence of the transmission coefficient at this frequency. A comparison of the curves shows that the control current required for complete switching is 1.6 A at an operating temperature of 87 K. Smaller control currents do not give complete switching because of the finite width of the superconducting transition and the extremely large dimensions of the film, 10×10 mm. At some expense in switching speed, the control signal power can be reduced in principle by controlling the temperature of the superconducting element.

To assess the operating capability of the switch at elevated signal powers, we used an inverse switching circuit in which the signal was fed to the feedback loop and the coefficient of transmission to the main line was measured. This ensured the maximum magnetic flux through the superconducting film and a low absorbed power in the matched load connected to the main line. Measurements made at 400 Hz revealed no substantial change in the temperature dependence of the transmission coefficient when the signal power was raised to 2 W, except for a small temperature shift of the curve, not exceeding 1 K, which was evidently caused by the sample being heated by the power dissipated in the load.

These results show that the screening of an alternating magnetic field by superconducting films may be of interest

for the practical development of superconducting switches for elevated-power microwave signals.

[1] M. M. Gaĭdukov, A. B. Kozyrev, V. N. Osadchiĭ, and V. F. Vratskikh, Pis'ma Zh. Tekh. Fiz. **20**(18), 86 (1994) [Tech. Phys. Lett. **20**, 761 (1994)].

[2] P. Grosse, *Free Electrons in Solids*, Mir, Moscow (1982).

[3] A. I. Golovashkin, E. V. Ekimov, S. I. Krasnosvobodtsev *et al.*, Physica C **162–164**, 715 (1989).

[4] T. M. Burbaev, G. A. Kalyuzhnaya, V. A. Kurbatov, V. S. Nozdrin, and N. A. Penin, Fiz. Tverd. Tela (St. Petersburg) **39**, 228 (1997) [Phys. Solid State **39**, 200 (1997)].

[5] V. Ambegaokar, B. I. Halperin, D. R. Nelson, and E. D. Siggia, Phys. Rev. Lett. **40**, 783 (1978).

Translated by R. M. Durham

Theory of the thermoelastic generation of mechanical vibrations in internally stressed solids by laser radiation

K. L. Muratikov

A. F. Ioffe Physicotechnical Institute, Russian Academy of Sciences, St. Petersburg
(Submitted February 25, 1998)
Pis'ma Zh. Tekh. Fiz. **24**, 82–88 (July 12, 1998)

An investigation was made of the behavior of transient deformations in solids with internal stresses exposed to time-modulated laser radiation. The nonlinear theory of thermoelasticity is used to propose a model for the excitation of mechanical stresses which takes account of the stress dependence of the thermoelastic coupling parameter. An expression is derived for the electric signal recorded by a piezoelement when mechanical vibrations are generated in a uniformly deformed sample. The results are compared with existing experimental data and show qualitative agreement. © *1998 American Institute of Physics.* [S1063-7850(98)01507-9]

An interesting line of research into the thermoelastic effect concerns the possible use of this effect to record mechanical stresses in solids.[1–5] Various experimental data have now been obtained for metals[1,4,5] and ceramics[2,3,6] as confirmation of this possibility. However, the mechanism responsible for the influence of mechanical stresses on the results of laser thermoelastic measurements has not been adequately clarified. In Ref. 4, a model was proposed for the formation of the thermoelastic signal, where its dependence on the mechanical stresses was mainly attributed to the dependence of the thermophysical parameters of the material on these stresses. In Ref. 6, however, it was shown that in ceramics a strong dependence of the thermoelastic signal on the residual stresses may be observed, even in the absence of any appreciable changes in their thermophysical properties.

Thus, the present paper proposes a model for the formation of the thermoelastic signal generated by laser radiation in solids which is capable of explaining these characteristics. An important difference is that this model assumes that the thermoelastic coupling coefficient depends on the mechanical stresses. Such a dependence was noted previously for the coefficient of thermal expansion[7] and for the elastic modulus.[8] Since the coefficient of thermoelastic coupling in isotropic solids is the product of these quantities, it is important to include this dependence in the thermoelastic coupling coefficient.

The generation of mechanical vibrations by laser radiation in mechanically stressed solids is analyzed in terms of nonlinear mechanics with initial deformations.[9] We shall assume that the initial deformations are not small. Thus, we shall assume that the displacement vector of points in the solid is given in the form

$$\mathbf{u}(\mathbf{r}) = \mathbf{r} + \mathbf{U}(\mathbf{r}) + \Delta\mathbf{u}(\mathbf{r}), \tag{1}$$

where $\mathbf{U}(\mathbf{r})$ describes the initial deformation and $\Delta\mathbf{u}(\mathbf{r})$ is the displacement of the solid particles caused by the thermoelastic deformations under action of the laser radiation.

The equation of motion for the elements of the solid in nonlinear mechanics[10] can be expressed in the form

$$\frac{\partial P_{ik}}{\partial x_k} = \rho_0 \Delta\ddot{u}_i, \tag{2}$$

where $P_{ik} = (\partial u_i/\partial x_m) t_{km}$ is the Pioli–Kirchhoff tensor, t_{km} is the stress tensor which is related to the internal energy density W of the solid by $t_{km} = \partial W/\partial u_{km}$; $u_{km} = \frac{1}{2}(\partial u_k/\partial x_m + \partial u_m/\partial x_k + \partial u_l/\partial x_k \partial u_l/\partial x_m)$ is the deformation tensor, and ρ_0 is the density of the solid in the initial state.

The energy density of the deformed solid may be expressed as the sum $W = W_1 + W_2$ (where W_1 is the mechanical energy density and W_2 is the energy density associated with the thermoelastic deformations). Here it is assumed that the solid is initially isotropic and its mechanical energy component is determined by the Murnaghan model.[11] For the thermoelastic energy density we shall assume by analogy with Ref. 7 that the thermoelastic coupling coefficient depends on the deformation tensor and this dependence is linear. We shall also assume that the strains Δu_{ik} created as a result of the action of laser radiation on the object are small. Under these conditions, the thermoelastic energy density may be expressed in the following form, to within linear terms in Δu_{ik}

$$W_2 = -\gamma_0(\delta_{ik} + \beta U_{ik})\Delta u_{ik}(T - T_0), \tag{3}$$

where γ_0 is the thermoelastic coupling coefficient for the nondeformed solid, β is a coefficient which determines the dependence of the thermoelastic coupling on the initial strain, and T_0 is the ambient temperature.

Note that for $\beta = 0$ equality (3) reduces to the usual expression for the thermoelastic energy density of an isotropic solid. Expressions (2) and (3) can be used to obtain the equation of motion for the displacement vector of the particles of a solid in which mechanical vibrations are excited by laser radiation as a result of the thermoelastic effect. Here we confine our analysis to a uniformly deformed solid with the components of the initial deformation vector defined as $U_i = A^{(i)}x_i$ ($A^{(i)}$ are constants characterizing uniform deformation in different directions). We shall also assume that the displacement vector $\Delta\mathbf{u}$ and the temperature fluctuations ΔT
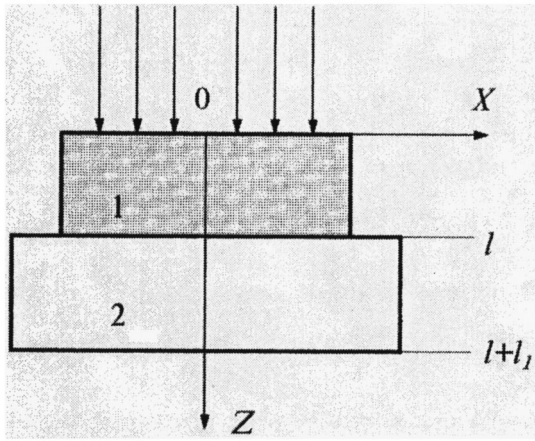
FIG. 1. Geometric configuration of sample and piezoelement: *1*—sample and *2*—piezoelement.

in the solid are small quantities and we shall use these to linearize the equations of motion. Without going into the details of the calculations, we give the final result for the vector components Δu_i. Using expressions (2) and (3), we obtain the following equations

$$f_k^{(i)} \frac{\partial^2 \Delta u_i}{\partial x_k \partial x_k} + h_k^{(i)} \frac{\partial^2 \Delta u_k}{\partial x_k \partial x_i} = g^{(i)} \frac{\partial \Delta T}{\partial x_i} + \rho_0 \Delta \ddot{u}_i, \quad (4)$$

where $f_k^{(i)} = \left[t_{kk}^{(0)} + \frac{(1+A^{(i)})^2}{2} (b + nU_{ii} + nU_{kk}) \right]$,

$b = 2\mu + (2m - n)U_{pp}$,

$h_k^{(i)} = (1 + A^{(i)})(1 + A^{(k)})$

$$\times \left[c_{ii} + 2mU_{kk} + \frac{1}{2}(b + nU_{ii} + nU_{kk}) \right],$$

$g^{(i)} = \gamma_0 (1 + A^{(i)})(1 + \beta U_{ii})$,

$c_{ii} = K - \frac{2}{3}\mu + 2(l - m + n/2)U_{pp} + (2m - n)U_{ii}$, $t_{kk}^{(0)}$ are the components of the initial deformation tensor, K and μ are the bulk modulus and the shear modulus of the material, and l, n, and m are the Murnaghan constants.

Note that on the right-hand sides of the expressions for $f_k^{(i)}$, $h_k^{(i)}$, c_{ii}, and $g^{(i)}$, summation is not performed over the repeated indices. Equation (4) can be used to determine the strain in a solid provided that the temperature distribution created by the exciting laser radiation is known. Here we shall assume that the appearance of internal stresses in an object does not cause appreciable changes in its thermophysical parameters. A similar situation has been observed experimentally in various ceramics.[6] We shall also assume that the surface of the sample is uniformly illuminated by laser radiation and the radiation is harmonically time-modulated.

In addition to the temperature distribution, the boundary conditions must also be defined to solve Eq. (4), these being determined by the method of recording the varying deformations in the object. Here we consider the case where these deformations are recorded by a piezoelement connected to the sample (see Fig. 1). To determine the varying deforma-

tions generated by the laser radiation, the boundary condition on the upper surface of the sample may be considered to be defined at the free surface. At the interface between the object and the piezoelement, we use the condition for continuity of the normal component of the stress vector at the interface $z = l$. In addition, to simplify the problem, we adopt the assumption made in nonlinear mechanics that the boundary conditions at a deformed surface may be replaced by those at an undeformed surface.[12]

The requirement for continuity of the normal component at the sample–piezoelement interface allows us to find the signal recorded by the piezoelement. This involves determining the component of the displacement vector $\Delta u_3(z,t)$ (Refs. 4 and 5). Assuming that the exciting laser radiation is harmonically modulated, we can express this component in the form $\Delta u(z,t) = \Delta u(z,\omega)e^{i\omega t}$ (where ω is the angular modulation frequency). Then, using Eq. (4) and the boundary conditions specified for $\Delta u_3(z,\omega)$ we obtain the following result:

$$\Delta u_3(z,\omega) = -\frac{U_3^{(0)} e^{-\sigma l}}{\cos Ql} \cos Qz$$

$$+ \left[\frac{\gamma_0 (1 + A^{(3)})(1 + \beta U_{33})}{f_3^{(3)} + h_3^{(3)}} \Delta T_s + \sigma U_3^{(0)} \right]$$

$$\times \sin Q(z - l) + U_3^{(0)} e^{-\sigma z}, \quad (5)$$

where $U_3^{(0)} = -[\gamma_0 \sigma (1 + A^{(3)})(1 + \beta U_{33})/(f_3^{(3)} + h_3^{(3)})\sigma^2 + \rho_0 \omega^2]\Delta T_s$, $\sigma = (1+i)\sqrt{\omega/2\varkappa}$, $\varkappa$ is the thermal diffusivity of the sample, $Q = \sqrt{\rho_0 \omega^2 / f_3^{(3)} + h_3^{(3)}}$, and ΔT_s is the amplitude of the temperature fluctuations of the sample surface.

The mechanical and electrical characteristics of the piezoelement are related by well-known equations.[13] Then, using the condition for continuity of the normal stress component at the sample–piezoelement interface, we obtain the following expression for the voltage $V(\omega)$ of the electric signal at the output of the piezodetector:

$$V(\omega) = -\frac{\varepsilon^{(T)} l_1}{C^{(ET)} \varepsilon^{(ST)} + e^{(T)2}} (f_3^{(3)} + h_3^{(3)}) \left. \frac{\partial \Delta u_3}{\partial z} \right|_{z=l}, \quad (6)$$

where $C^{(ET)}$, $\varepsilon^{(ST)}$, and $e^{(T)}$ are the piezoelectric characteristics determined as in Ref. 13.

Expression (6) can be used to determine the piezoelectric signal under fairly general conditions. However, the analysis is confined here to the case where the modulation frequency of the exciting radiation is not too high, so that the condition $Ql \ll 1$ is satisfied. We shall also assume that the sample is fairly thick in thermal terms, i.e., $\sigma l \ll 1$. Then, using expression (6), the signal from the piezodetector is obtained as

$$V(\omega) = i\,\frac{\varepsilon^{(T)}\varkappa\rho_0^{3/2}\omega^2 l_1}{C^{(ET)}\varepsilon^{(ST)}+e^{(T)2}}\,\frac{\gamma_0(1+A^{(3)})(1+\beta U_{33})\Delta T_s}{\left\{(1+A^{(3)})\left(K+\dfrac{4}{3}\mu\right)+\left[t_{33}^{(0)}+(1+A^{(3)})(2lU_{pp}+(4m+n)U_{33})\right]\right\}^{3/2}}. \tag{7}$$

Expression (7) can be used to analyze some general laws governing the behavior of the piezoelectric signal from objects with internal stresses. Here the analysis is confined to physical rather than geometric nonlinearities,[9,12] i.e., we shall assume $A^{(3)}\ll 1$. According to the results presented in Ref. 7, the coefficient β is positive. Thus, the action of tensile stresses helps to intensify the thermoelastic coupling in the sample while compressive stresses tend to reduce this coupling.

Experiments to excite mechanical vibrations in loaded titanium rods using laser radiation were described in Ref. 5. In accordance with expression (7), an increase in the piezoelectric signal was recorded when mechanical vibrations were excited by laser radiation in zones of tensile stresses while a reduction in this signal was observed in zones of compressive stresses. The influence of the internal stresses on the piezoelectric signal can be estimated using data on the coefficient β for metals.[7] Thus, for the conditions reported in Ref. 5, expression (7) shows that the stress dependence of the thermoelastic coupling coefficient may change the piezoelectric signal by 10%.

This value is slightly lower than that obtained in Ref. 5. However, it should be borne in mind that for most metals the Murnaghan constants are negative. Then, in accordance with expression (7), the dependence of the piezoelectric signal on the stresses, caused by mechanical nonlinearities, will be similar to the dependence of the thermoelastic coupling coefficient. Under these conditions, the total change in the piezoelectric signal will be slightly greater than that caused only by the change in the thermoelastic coupling coefficient. Unfortunately it is difficult to obtain a more detailed estimate of the piezoelectric signal because no data on the Murnaghan constant are available for titanium. Substantial changes in the piezoelectric signal as a result of internal stresses were also recorded near the ends of cracks in titanium.[3,6] These changes are usually also a few tens of percent.

To sum up, this theory qualitatively explains the main characteristics of the generation of mechanical vibrations by laser radiation in internally stressed solids. However, before quantitative agreement can be achieved between theory and experiment, this model must be further developed to account more comprehensively for the behavior observed in these experimental investigations.

[1] M. Kasai and T. Sawada, *Photoacoustic and Photothermal Phenomena II*, Springer Series in Optical Sciences Vol. 33 (Springer-Verlag, Berlin, 1990), p. 33.

[2] R. M. Burbelo, A. L. Gulyaev, L. I. Robur, M. K. Zhabitenko, B. A. Atamanenko, and Ya. A. Kryl, J. Phys. (Paris), Colloq. **4**, Colloq. 7, 311 (1994).

[3] H. Zhang, S. Gissinger, G. Weides, and U. Netzelmann, J. Phys. (Paris), Colloq. **4**, Colloq. 7, 603 (1994).

[4] M. Qian, J. Acoust. **14**(2), 97 (1995).

[5] R. M. Burbelo and M. K. Zhabitenko, *Progress in Natural Science* (Taylor and Francis, Washington, 1996), Supplement 6, p. 720–723.

[6] K. L. Muratikov, A. L. Glazov, D. N. Rouz, D. E. Dumar, and G. Kh. Kvaĭ, Pis'ma Zh. Tekh. Fiz. **23**(3), 44 (1997) [Tech. Phys. Lett. **23**, 188 (1997)].

[7] R. I. Garber and I. A. Gindin, Fiz. Tverd. Tela (Leningrad) **3**, 176 (1961) [Sov. Phys. Solid State **3**, 127 (1961)].

[8] T. Bateman, W. P. Mason, and H. J. McSkimin, J. Appl. Phys. **32**(5), 928 (1961).

[9] A. N. Guz', Prikl. Mekh. **6**(2), 3 (1970).

[10] T. Tokuoka, and M. Saito, J. Acoust. Soc. Am. **45**(5), 1241 (1969).

[11] A. I. Lur'e, *Nonlinear Theory of Elasticity*, North-Holland, Amsterdam (1990) [Russ. orig. Nauka, Moscow (1980), 512 pp.].

[12] V. V. Novozhilov, *Foundations of the Nonlinear Theory of Elasticity*, Graylock Press, Rochester, N.Y. (1953) [Russ. orig. Gostekhizdat, Moscow (1948), 211 pp.].

[13] W. Jackson and N. M. Amer, J. Appl. Phys. **51**, 3343 (1980).

Translated by R. M. Durham

Anomalously high conductivity in a thin polyphthalidylidene biphenylene film

V. A. Zakrevskiĭ, A. N. Ionov, and A. N. Lachinov

A. F. Ioffe Physicotechnical Institute, Russian Academy of Sciences, St. Petersburg;
Institute of Molecular and Crystal Physics, Russian Academy of Sciences, Ufa

An anomalously high conductivity was observed for the first time in a thin film of polyphthalidylidene biphenylene inserted between two metal electrodes with no electric field applied but exposed to the action of a small uniaxial mechanical pressure. © *1998 American Institute of Physics.* [S1063-7850(98)01607-3]

In recent years, various reports of high conductivity in polymer films have appeared (see Ref. 1 and the literature cited therein), and these unexpected results have attracted the attention of researchers. However, no generally accepted explanation has yet been provided for these observations especially because of the (in our opinion) inadequate treatment of the possible consequences which may result from the different experimental conditions. Thus, in the introductory part of this study we shall merely discuss some of the results obtained so far.

It was established in Ref. 2 that a thin ($d \cong 12$-μm) film of poly(3,3″-phthalidylidene-4,4″-biphenylylene) (PPB),[1)] one of a promising class of polyphthalidylidene arylene polymers, becomes highly conducting in a relatively low-intensity electric field ($E < 10^3$ V/cm) if a small ($P < 10^5$ Pa) uniaxial mechanical pressure is applied to the metal electrodes. It was shown in Ref. 3 that if the metal electrodes were in the superconducting state, the conductivity of this sandwich structure was so high that the instruments recorded effectively zero resistance. This effect was also observed for oxidized polypropylene[1,4] and polyimide films.[5]

Key parameters in these polymer film switching effects are the electric field strength and the electric current at which the conductivity of the material changes abruptly. These parameters can determine the mechanism responsible for the highly conducting state in the polymer. For example, switching of comparatively thick polyimide films ($d \sim 12$ μm) sandwiched between low-melting electrodes is accompanied by metallic dendrite intergrowth through the polymer film in an electric field close to breakdown ($E \sim 10^6$ V/cm) if there is no special limitation on the breakdown current between the electrodes.[6] In this case, the polymer will clearly be shunted by the metal bridge. It was shown in Refs. 4 and 5 that polymer films 3–5 μm thick are switched to the highly conducting state in a relatively low-intensity electric field ($E < 10^3$ V/cm). When the breakdown current was limited to 10–100 μA, no solid metallic dendrite formed, but the presence of electrode material in the form of isolated microparticles in the polymer matrix could not be ruled out. In this case, the anomalously high conductivity could be attributed to a conducting channel with a modified polymer whose structure differed from that of the initial polymer.

The aim of the present study was specifically to obtain new experimental data on the conditions for the formation of a highly conducting state and to discuss possible reasons for the appearance of conducting channels in the film. Experiments were first carried out to study the properties of thin polyphthalidylidene biphenylene films exposed to the action of uniaxial pressure in the absence of an external electric field.

The polymer sample was a PPB film ~ 1 μm thick. The electrodes were made of tin and had a diameter of 15 mm. The PPB film was deposited from a cyclohexane solution directly onto the polished surface of one of the tin electrodes by centrifuging. The film was then placed in a drying cabinet for 60 min at 100 °C to remove the cyclohexanone solvent. The second tin electrode was lightly clamped to the polymer film.

The formation of the conducting state in this sandwich structure was recorded as follows. The electrodes were connected to a digital voltmeter with a fairly high input resistance ($R_v > 10^8$ Ω). In the insulating state, when the resistance of the sandwich structure R_s ($R_s > 10^{14}$ Ω) exceeded the input resistance of the voltmeter R_v, the voltmeter display recorded a small fluctuating noise voltage, no greater than a few millivolts, caused by external induction in the voltmeter input circuit. As the pressure was raised to the threshold level ($\sim 10^4$ Pa), the structure changed from insulating to conducting, as a result of which R_s became lower than R_v. The signal induced at the input to the voltmeter then disappeared and the voltmeter displayed zero voltage.

An attempt was then made to measure the resistance of the film. The sandwich structure in which the conducting state was only produced by external mechanical pressure was placed in a helium cryostat. After the conducting state had been attained at room temperature and during cooling of the helium cryostat to liquid nitrogen temperature, the metal electrodes of the sandwich structure were shorted to eliminate induction of static electricity from external uncontrollable sources of electromagnetic radiation. At temperatures between 4.2 and 300 K the resistance of this sandwich structure remained constant at ~ 0.04 Ω. A current of 100 μA, set by the large load resistance, was selected to measure the temperature dependence of the resistance below 4.2 K and
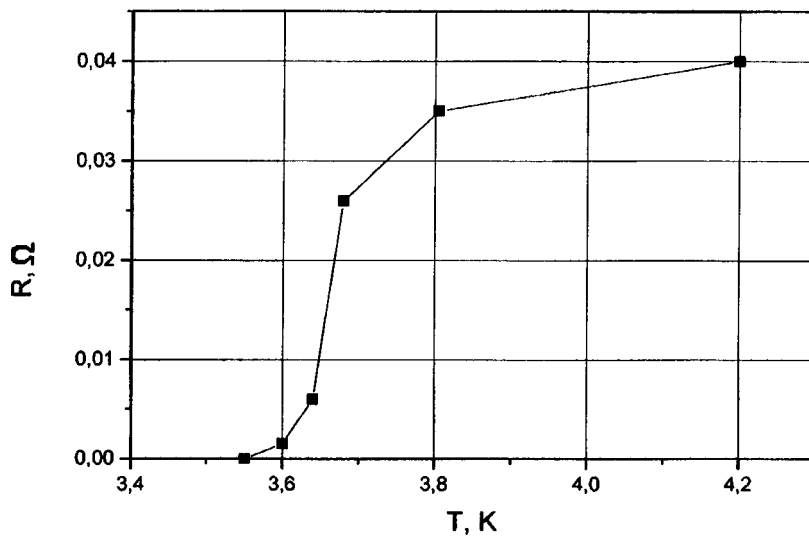
FIG. 1. Resistance of an Sn–PPB–Sn structure versus temperature under an external uniaxial pressure of $\sim 10^4$ Pa.

the voltage drop was measured with the voltmeter at the sandwich structure.

Figure 1 gives the temperature dependence of the resistance of a tin–PPB–tin sandwich structure. It is known that tin becomes superconducting for $T_c \cong 3.7$ K. Thus, at temperatures $T < 3.7$ K the resistance in the electrodes can be neglected and all the measured resistance will be determined exclusively by the conducting polymer channel. It can be seen from the figure that for $T \leqslant 3.7$ K the resistance drops sharply and for $T < 3.6$ K is less than 0.001 Ω, which is the resolution limit of this apparatus.

The highly conducting state in the sandwich structure is obtained under experimental conditions when there is no doubt that no electrode material is present in the polymer film. Thus, the highly conducting state is an intrinsic physical property of the metal–PPB film–metal sandwich structure.

The highly conducting state presupposes that there is a high concentration of free carriers with a fairly high mobility. In this case, the carriers are injected into the polymer from the electrodes.

Electrification of polymers on contact with metals (charge transport across the interface) is a well-known phenomenon studied by various authors.[7–9] It is assumed that electrons entering the polymer are trapped by deep local states situated near the Fermi level of the metal.[9] The deep levels are associated with molecular fragments (atomic groups) with a high positive electron affinity, such as end groups, side radicals, or impurities. According to estimates made in Ref. 9, these local deep levels are separated from the vacuum level by approximately 4 eV. This value is similar to the work function of a polycrystalline metal whose surface is coated with a layer of adsorbate (more accurately, it is similar to the lowest work function of the spotty surface of a metal from which contaminants have not been removed) and as a result, conditions are created for the injection of electrons into the polymer. Fairly high concentrations of centers with a high electron affinity are evidently only achieved in small volumes. This is why the anomalously high conductivity being discussed can only be observed with short distances

between the electrodes, as is found in our case, where the thickness of the film was less than 1 μm.

Pressure must be applied to the electrodes to achieve reliable mechanical contact between the metal and the polymer (or the contact area must be increased). This condition must be satisfied for efficient transport of electrons from the metal to the polymer.

At present, there is no rigorous theoretical model which could explain the high conductivity in polyphthalidylidene biphenylene. A possible mechanism for electron transport could involve resonant (activation-free) tunneling between nearest localized states. These low-energy states form chains with linear dimensions of order 1 μm. However, in this approach the conductivity in the chain may be very high but still finite.

[1)]In Ref. 2 this polymer is called polydiphenylenephthalide. The present name complies with the international classification—poly(3,3″-phthalidylidene-4,4″-biphenylylene)—and more accurately describes the polymer structure.

---

[1] V. M. Arkhangorodskiĭ, A. N. Ionov, V. M. Tuchkevich, and I. S. Shlimak, JETP Lett. **51**, 67 (1990).

[2] A. N. Lachinov, A. Yu. Zherebov, and V. M. Kornilov, JETP Lett. **52**, 103 (1990).

[3] A. N. Ionov, A. N. Lachinov, M. Rivkin, and V. M. Tuchkevich, Solid State Commun. **82**, 609 (1992).

[4] A. N. Ionov and V. M. Tuchkevich, Pis'ma Zh. Tekh. Fiz. **16**(16), 90 (1990) [Sov. Tech. Phys. Lett. **16**, 638 (1990)].

[5] A. M. El'yashevich, A. N. Ionov, M. M. Rivkin, and V. M. Tuchkevich, Fiz. Tverd. Tela (St. Petersburg) **34**, 3457 (1992) [Sov. Phys. Solid State **34**, 1850 (1992)].

[6] A. M. El'yashevich, A. N. Ionov, V. M. Tuchkevich *et al.*, Pis'ma Zh. Tekh. Fiz. **23**(7), 8 (1997) [Tech. Phys. Lett. **23**, 538 (1997)].

[7] D. K. Davis, J. Phys. D **2**, 1533 (1969).

[8] T. J. Fabish, H. M. Saltsburg, and M. L. Hair, J. Appl. Phys. **47**, 930 (1976).

[9] C. B. Duke and N. J. Fabish, Phys. Rev. Lett. **37**, 1075 (1976).

Translated by R. M. Durham

Stochastically induced hysteresis in optical carrier generation

Yu. V. Gudyma

Chernovtsy State University

A study is made of a mechanism for the occurrence of a noise-induced kinetic transition in a thin amorphous semiconductor wafer. © *1998 American Institute of Physics.*
[S1063-7850(98)01707-8]

The appearance of new steady states in nonequilibrium open systems in response to external multiplicative noise is one of the most dramatic effects in self-organizing systems.[1] However, the number of real physical systems in which this effect occurs is fairly limited and it is therefore relevant to search for such objects (see Ref. 2 for one of the most recent examples). Here we propose a model for the occurrence of a noise-induced kinetic transition in a thin amorphous semiconductor wafer.

Experimental and theoretical investigations show that in most amorphous semiconductors the fundamental absorption edge may be described by a simple power law.[3] For some semiconductors in the energy range above the exponential tail (GeTe, As_2Te_3, As_2Se_3, or As_2S_3) or for amorphous silicon which has no exponential absorption edge, the spectral dependence of the absorption coefficient is described by the formula

$$\alpha(\omega) = B(\hbar\omega - E_0)^2/\hbar\omega, \qquad (1)$$

where the values of the parameters B and E_0 are determined experimentally. This expression is similar to that for the absorption coefficient for indirect transitions in crystalline semiconductors. The renormalized value of the band gap[4]

$$E_g^* = E_g(1 - bn) \qquad (2)$$

implies that the light beam is of sufficiently high intensity for the lower states of the energy troughs to be filled more rapidly than they decay.

The influence of interelectron interaction on the electron energy spectrum in a nondegenerate semiconductor has been studied on many occasions. The simplest phenomenological form of this dependence has been selected here.

It is also implicit that the light intensity is so high that the concentrations of photogenerated electrons and holes considerably exceed their equilibrium values (which implies $n \approx p$). If the sample thickness is small compared with $(B\hbar\omega)^{-1}$, we can write the equation for the generation-recombination kinetics in the form

$$\frac{dn}{dt} = \nu\alpha J - an^2, \qquad (3)$$

where ν is the quantum yield, J is the photon flux density, and a is the coefficient of interband recombination (radiative or nonradiative). The form of the absorption coefficient (1) with allowance for Eq. (2) ensures positive feedback in Eq. (3).

It is convenient to introduce the dimensionless variables

$$\eta = bn, \quad \theta = b^{-1}at, \quad \Delta = (\hbar\omega - E_0)/E_0^{-1},$$

$$\beta = a^{-1}b^2 \nu B E_0^2 J(\hbar\omega)^{-1}.$$

Then, in accordance with Eqs. (3) and (1), we have

$$\frac{d\eta}{d\theta} = \beta(\Delta + \eta)^2 - \eta^2. \qquad (4)$$

Equation (4) has two steady-state solutions, unstable and stable, which correspond to a soft regime of bistability in the nonequilibrium carrier distribution. Note that in the model of direct allowed transitions the corresponding generation-recombination equation may have three roots near the absorption threshold. A similar situation was considered for crystalline semiconductors in Ref. 5. The indeterminate loss of coherence of the light is described by the process $\beta(t) = \beta + \sigma\xi(t)$, where the external noise $\xi(t)$ is characterized by very fast fluctuations compared with the characteristic evolution time of the system $\tau = b/a$ (quasi-white noise).

In terms of generalized functions, Gaussian white noise is the derivative of a Wiener process so that Eq. (4) is transformed to give the Stratonovich stochastic differential equation which may be made to correspond to the Fokker–Planck equation which determines the evolution of the transition probability $p(\eta, \theta | \eta', \theta')$

$$\frac{\partial p(\eta, \theta | \eta')}{\partial\theta} = -\frac{\partial}{\partial\eta}[\beta(\Delta + \eta)^2 - \eta^2$$
$$+ \sigma^2(\Delta + \eta)^3]p(\eta, \theta | \eta')$$
$$+ \frac{\sigma^2\beta^2}{2}\frac{\partial^2}{\partial\eta^2}\{\Delta + \eta\}^4 p(\eta, \theta | \eta'). \qquad (5)$$

The phenomena described by Eq. (5) take place on two time scales: the fast time scale is associated with inverse relaxation to the local minimum after the perturbation, while the slow scale is associated with a transition from the metastable minimum to the global minimum. The steady-state distribution in the stationary process has the form

$$p_s(\eta) = N\{\beta(\Delta + \eta)^2\}^{-1}$$

$$\times \exp\left(-\frac{2}{\sigma^2} \int_0^\eta [\beta\{\Delta + U\}^2 - U^2][\Delta + U]^{-4} dU\right).$$

(6)

The constant N is determined from the normalization condition. The solution (6) may be assigned a potential form since its maxima correspond to stable steady states and its minima correspond to unstable ones. We shall use the ''probability'' potential, after writing the steady-state probability density in the form

$$p_s = N \exp[-2V(\eta)/\sigma^2],$$

(7)

where

$$V(\eta) = -\left[\int_0^\eta [\beta\{\Delta + U\}^2 - U^2][\Delta + U]^{-4} dU\right.$$

$$\left. - \frac{\sigma^2}{2} \ln[(\Delta + \eta)^2]\right].$$

(8)

The extrema of the steady-state probability density are easily obtained from the equation

$$(\beta - \sigma^2\Delta)\Delta^2 + (2\beta - 3\sigma^2\Delta)\Delta\eta + (\beta - 1 - 3\sigma^2\Delta)\eta^2 - \sigma^2\eta^3 = 0,$$

(9)

which has three solutions (two stable and one unstable). For $\sigma \to 0$ there are only two of these solutions and they are exactly the same as the steady-state solutions of the determinate equation (4). Even unusually fast completely random fluctuations of the control parameters substantially change the macroscopic behavior of the nonlinear dynamic system (3): they give rise to additional steady states. Under the action of fast external noise, the system is converted from a soft to a hard (hysteresis) regime with a multivalued distribution of optically generated carriers in the thin semiconducting wafer. Estimates show that a laser radiation intensity of 100 W/cm is required for the experimental observation of light absorption hysteresis in these materials for wafers of the order of 100–1000 Å thick and in this case, the parametric fluctuations are less than 0.01–0.1 of the value.

[1] W. Horsthemke and R. Lefever, *Noise-Induced Transitions* (Springer-Verlag, Berlin, 1984; Mir, Moscow 1987, 400 pp.).

[2] R. E. Kunz and E. Scholl, Z. Phys. B **99**, 185 (1996).

[3] N. F. Mott and E. A. Davis, *Electronic Processes in Non-Crystalline Materials* (Clarendon Press, Oxford, 1971; Mir, Moscow, 1974, 472 pp.).

[4] A. L. Semenov, Zh. Eksp. Teor. Fiz. **111**, 2147 (1997) [JETP **84**, 1171 (1997)].

[5] V. A. Kochelap, L. Yu. Mel'nikov, and V. N. Sokolov, Fiz. Tekh. Poluprovodn. **16**, 1167 (1982) [Sov. Phys. Semicond. **16**, 746 (1982)].

Translated by R. M. Durham

A new method of reconstructing spectra

A. M. Egiazaryan and Kh. V. Kotandzhyan

Institute of Applied Physics Problems, Armenian Academy of Sciences
(Submitted July 28, 1997)
Pis'ma Zh. Tekh. Fiz. **24**, 5–9 (July 26, 1998)

A theoretical method is proposed for accurate reconstruction of the spectrum using bounded sets of discrete values of the spectrum intensities. The method is based on a well known measurement theorem from optics. This method was used to solve the corresponding integral equation to eliminate instrumental distortions and to accurately reconstruct the spectra using the appropriate discrete values. © *1998 American Institute of Physics.*
[S1063-7850(98)01807-2]

INTRODUCTION

Methods of obtaining x-ray spectra, Mössbauer spectra, and also theoretical methods of analyzing experimental data have been dealt with fairly extensively in the literature.[1–4] Since spectral lines reflect the distribution of electrons over the energy levels of crystal atoms and molecules, the highest possible resolution is required. In analyses of experimental data, curves are approximated by summing power series, with the result that the experimental points are smoothed. However, certain difficult problems must be overcome to improve the resolution. The aim of the present paper is to propose a theoretical method of accurately reconstructing the spectrum from bounded sets of discrete values of the spectrum intensities. The method is based on the measurement theorem well known in optics.[5] We propose a formula for complete reconstruction of the spectra assuming that the wave trains have a finite duration. This formula was applied to solve the corresponding integral equation to eliminate instrumental distortions when these are described by a dispersion distribution. We obtained a formula for accurate reconstruction of the spectra and present an example of suitably processed experimental curves.

THEORETICAL BASIS OF THE METHOD

It is known that for a specific class of functions, known as functions of bounded spectral width, the functions can be completely reconstructed from sets of discrete values if the constraint is imposed that the interval between these discrete values does not exceed a certain value. By functions $g(x)$ of bounded spectral width, we have in mind functions whose Fourier transforms are only nonzero in a finite region of space $2B$. This statement is known as the Kotel'nikov theorem, according to which

$$g(x) = \sum_{k=-\infty}^{\infty} g\left(\frac{k}{2B}\right) \frac{\sin \pi[2Bx-k]}{\pi[2Bx-k]}, \tag{1}$$

i.e., the function $g(x)$ can be completely reconstructed from its corresponding discrete values.

Regardless of their physical nature, the wave paths have a finite duration $2B$. Let us assume that the time dependence

of the train amplitude is described by the function $f(t)$. The Fourier transform $F(\omega)$ will then be the wave amplitude in the frequency space and $J(\omega) = |E(\omega)|^2$ its spectral intensity.

It then follows that $J(\omega)$ is a function of bounded spectral width and hence can be reconstructed from sets of its discrete values. We used this idea for a complete reconstruction of Mössbauer spectra recorded at our Institute. Figure 1 shows the experimental curve and the theoretical curve reconstructed using formula (1). In this case the shortest interval between the experimental points was taken as $1/2B$.

In the usual methods of treating experimental data (such as the power series method), the experimental curves are approximated by certain analytic functions. Depending on the accuracy of the approximation, only some of the experimental points lie on this analytic curve and these points are smoothed. When the spectrum is reconstructed by the method described above, all the experimental points lie exactly on the curve $g(x)$, as can be seen from Fig. 1.
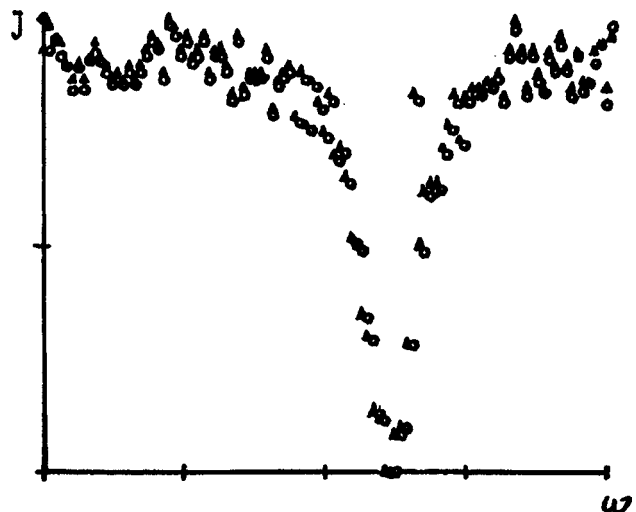

FIG. 1. Experimental curve of the Mössbauer spectrum (circles) and the corresponding theoretical reconstruction (triangles).

To eliminate instrumental distortions and reconstruct the accurate form of the spectrum $I(\omega)$, we need to solve the integral equation

$$J(\omega) = \int_{-\infty}^{\infty} I(x) \frac{dx}{\pi\Omega\left[1 + \left(\frac{\omega-x}{\Omega}\right)^2\right]}, \qquad (2)$$

where Ω is the half-width of the instrumental distortion curve.

Bearing in mind formula (1), we apply the convolution theorem for Fourier transformation to Eq. (2). Since we have

$$\frac{\sin \pi[2B\omega-k]}{\pi[2B\omega-k]} = \int_{-\infty}^{\infty} \text{rect } P \exp[-12\pi P(2B\omega-k)]dp, \qquad (3)$$

where

$$\text{rect } P = \begin{array}{ll} 1 & -\frac{1}{2} < P < \frac{1}{2} \\[2mm] 0 & P > \frac{1}{2}, \quad P < -\frac{1}{2}, \end{array}$$

the Fourier transform of the dispersion distribution has no zeros.[6] From formula (2) we obtain

$$I(w) = \sum_{k=-\infty}^{\infty} \int_{-\infty}^{\infty} dq \int_{-\infty}^{\infty} dP \text{ rect } P \exp[i2\pi qw + 2\pi\Omega|q| + 12\pi Pk]J\left(\frac{k}{2B}\right)\delta(2BP+q), \qquad (4)$$

where $\delta(x)$ is the Dirac delta function.

After various transformations, formula (4) becomes

$$I(w) = \sum_{k=-\infty}^{\infty} J\left(\frac{k}{2B}\right)\left[\frac{(8\pi Bw - 4\pi k + 8\pi\Omega B)\exp 2\pi\Omega B \sin(2\pi Bw - \pi k) - 8\pi\Omega B}{(4\pi Bw - 2\pi k)^2 + (4\pi\Omega B)^2}\right]. \qquad (5)$$

It is easily observed that when $\Omega = 0$, i.e., when the device does not distort the spectrum, the expansion (5) is identical to expansion (1).

Thus, expansion (5) can be used to reconstruct the exact form of the spectrum $I(w)$ from the experimentally determined corresponding discrete values.

With the proposed method, we can accurately describe the experimental curves by analytic expressions and thereby avoid smoothing of the experimental points.

When the proposed method is used in spectroscopy, the problem of reducing the goniometer pitch does not arise, since the reconstruction is equivalent to using goniometers with infinitely small pitch.

The proposed method is saves a lot of time compared with the conventional experimental methods of recording spectra and the distortions introduced by the apparatus can be eliminated to produce accurate spectra.

[1] M. A. Blokhin, *Physics of X-Rays* [in Russian], Gostekhizdat, Moscow (1957).

[2] M. A. Blokhin, *Methods of X-ray Spectroscopic Research*, Pergamon Press, Oxford (1965) [Russ. orig. Fizmatgiz, Moscow (1959)].

[3] Z. G. Pinsker, *X-Ray Crystal Optics* [in Russian], Nauka, Moscow (1982).

[4] R. G. Gabrielyan and Kh. V. Kotandjian, Phys. Status Solidi B **151**, 655 (1989).

[5] R. J. Collier, C. B. Burckhardt, and L. H. Lin, *Optical Holography* (Academic Press, New York, 1971; Mir, Moscow, 1973).

[6] A. P. Prudnikov, Yu. A. Brychkov, and O. I. Marichev, *Integrals and Series*, Vols. 1–3 (Gordon and Breach, New York, 1986, 1986, 1989) [Russ. original, Vols, 1–3, Nauka, Moscow, 1981, 1983, 1986].

Translated by R. M. Durham

Nonlinear stage of instability evolution in a monostable active medium

A. A. Pukhov

Joint Institute of High Temperatures, Scientific-Research Center of Applied Problems in Electrodynamics, Russian Academy of Sciences, Moscow
(Submitted January 8, 1998)
Pis'ma Zh. Tekh. Fiz. **24**, 10–15 (July 26, 1998)

A theoretical analysis is made of the nonlinear stage of instability evolution in a monostable active medium described by a ''reaction–diffusion'' type equation. The boundary of that region of the medium in which instability develops propagates at constant velocity. Group-theoretical analysis of the problem yields an analytic expression for the propagation velocity of this boundary. The results may be important for the analysis of instability evolution in a wide range of active media. © *1998 American Institute of Physics.* [S1063-7850(98)01907-7]

A wide range of highly nonequilibrium physical systems (active media) are described by a nonlinear ''reaction–diffusion'' equation

$$\frac{\partial \theta}{\partial t} = \Delta \theta + f(\theta), \tag{1}$$

where $\Delta = \partial^2/\partial^2 x + \partial^2/\partial^2 y + \partial^2/\partial^2 z$, and θ may be the temperature of the medium, the reagent concentration, the electric field, and so on, depending on the nature of the dissipative process (see Ref. 1 and the literature cited therein). To be specific, let us take θ to be the temperature. The nonlinear stage of instability evolution in these systems is completely determined by the form of the source function $f(\theta)$. For example, for bistable systems (Fig. 1, curve *1*) the transition between the two stable states of the medium $\theta(x,y,z,t) = \theta_1$ and $\theta(x,y,z,t) = \theta_3$ is accomplished by the propagation of a switching autowave. In the one-dimensional case, the asymptotic behavior of this wave $\theta(x,t) = \theta(x-ut)$ is characterized by its constant propagation velocity u (Ref. 1). Methods for approximate calculation of the wave velocity and its dependence on the parameters of the problem have now been studied in fairly great detail.[2,3]

In many situations, however, the system loses its bistability (such as when the dissipation depends strongly on temperature, the differential conductivity increases abruptly, and so on[1-3]). The qualitative form of the dependence $f(\theta)$ for this case is shown in Fig. 1 (curve *2*). When the temperature θ exceeds the threshold θ_2 in a certain region of the medium, the system undergoes unbounded self-heating. This circumstance is responsible for the particular instability evolution in a monostable medium. The nonlinear wavefront $\theta(x,y,z,t)$ separating the ''hot'' and ''cold'' regions is constructed as follows. The temperature θ in the cold region is equal to θ_1, whereas that in the hot region increases without bound. Thus, the evolution of instability in this case is the result of two parallel processes: expulsion of the cold region by the hot and a rapid increase in the temperature of the hot region.

We shall first consider the one-dimensional case ($D = 1$). Equation (1) has no self-similar solution of the traveling autowave type $\theta(x,t) = \theta(x-ut)$ because of the unbounded increase in the temperature of the hot region

$\theta(x,t) > \theta_2$. However, for a wide range of monostable active media numerical simulation has shown that despite the time-dependent behavior of the temperature $\theta(x,t)$ in the hot region, the front propagates at a constant velocity u, as shown in Fig. 2 (Refs. 4–6). Thus, the distribution $\theta(x,t)$ in the cold tail of the front has the form $\theta(x,t) = \theta(x-ut)$ and in a system moving together with the wave, asymptotically ($\theta \cong \theta_1$) satisfies the equation

$$\frac{d^2\theta}{dx^2} + u\frac{d\theta}{dx} + f(\theta) = 0. \tag{2}$$

In fairly general form the nonlinear source function $f(\theta)$ may be given as[5]

$$f(\theta) = a\,\theta^m(\theta^n - b), \tag{3}$$

where m, n, a, b are arbitrary positive values and $b = \theta_2^n$. The absence of a self-similar solution means that the velocity u cannot be determined as an eigenvalue of Eq. (2) with the boundary conditions $d\theta/dx = 0$ at $x = \pm\infty$ using standard methods from the theory of finite-amplitude autowave propagation.[1-3] in this case, group-theoretical concepts[7,8] can be applied to find the value of u. We assume that the exponents m and n are fixed and that a and b are control parameters of the problem. Equations (2) and (3) are then invariant with respect to the transformation group of the variables

$$x = L^{-p}x', \quad \theta = L^q\theta', \quad u = L^p u',$$

$$a = L^{2p+(1-m-n)q}a', \quad b = L^{nq}b', \tag{4}$$

which comprise a group of expansions with the scale factor L. The exponents of the scale factors of the expansion are determined by the condition of invariance with respect to the transformation (4), given by (2) and (3), so that the new (primed) variables satisfy the same equations (2) and (3). This has the result that the expansion group (4) contains free parameters L, p, and q which may have arbitrary values.

It is clear from physical reasoning that the velocity u in Eqs. (2) and (3) is a function only of a and b: $u = F(a,b)$. This relation should be invariant with respect to the group transformation (4), i.e., $u' = F(a',b')$ (Ref. 9). We shall
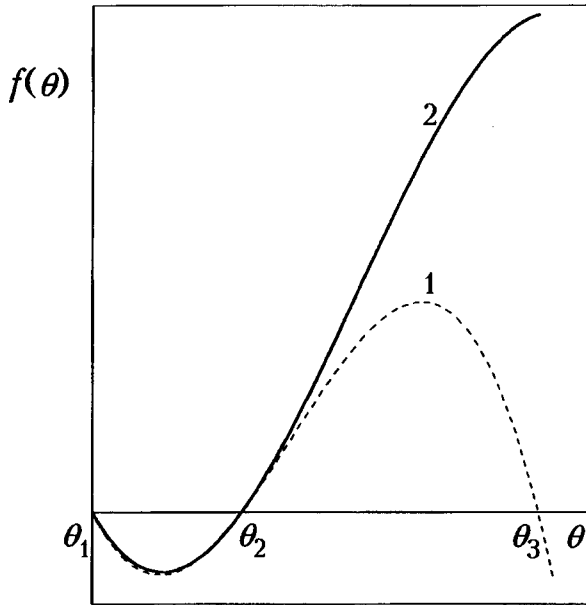
FIG. 1. Characteristic dependence of the nonlinear source function $f(\theta)$ on θ in the bistable (curve 1) and monostable (curve 2) cases.

seek a solution in the form $u \propto a^r b^s$ (Ref. 10), where the exponents r and s are to be determined. We then have

$$u/a^r b^s = L^{p(2r-1)+q[ns+(1-m-n)r]} u'/a'^r b'^s, \qquad (5)$$

and from the condition of invariance $u/a^r b^s = u'/a'^r b'^s$ we obtain $p(2r-1)+q[ns+(1-m-n)r]=0$. On account of the arbitrariness of p and q in the transformation (4), we obtain single-valued expressions for the exponents: $r=1/2$, $s=(m+n-1)/2n$. Thus, for the velocity u we have

$$u \propto a^{1/2} b^{(m+n-1)/2n}. \qquad (6)$$

The coefficient of proportionality of the order of unity in Eq. (6) cannot be obtained using group concepts. Numerical calculations[4,5] or additional reasoning[6] are required to determine this.

In the symmetric two-dimensional ($D=2$, $r=(x^2+y^2)^{1/2}$) and three-dimensional ($D=3$, $r=(x^2+y^2+z^2)^{1/2}$)
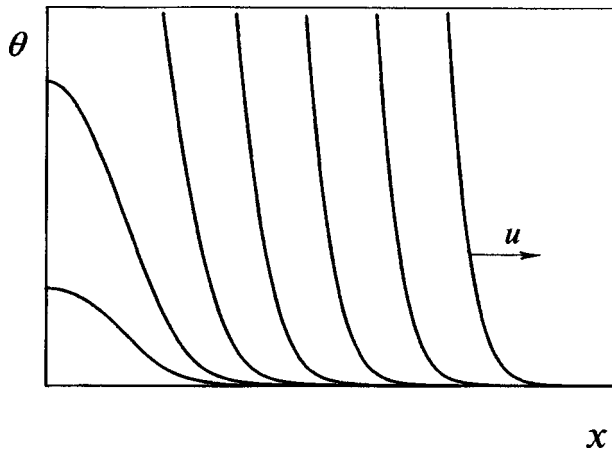
FIG. 2. Schematic showing the evolution of the wavefront profile in a monostable active medium.[4-6] The curves are separated by different time intervals.

cases, the self-similarity is approximate: $\theta(r,t) \cong \theta(r-ut)$ and for $r \gg 1$ we obtain for the wavefront velocity $dr/dt = u-(D-1)/r$ (Refs. 1 and 2). The curvature of the wavefront slows the wave which yields a logarithmic correction to the uniform propagation of the front $r \cong ut - u^{-1}(D-1)\ln t$. Thus, a group-theoretical analysis of Eqs. (1) and (3) can be used to obtain the functional dependence of u on the control parameters for any dimensions of the problem.

To conclude, we note that these characteristics of the evolution of instability in a monostable active medium show similarities to so-called ''blowup regimes.'' These regimes are observed in problems involving nonlinear active media where the specific heat and heat release depend strongly on temperature,[11] which are described by

$$\theta^k \frac{\partial \theta}{\partial t} = \nabla(\theta^l \nabla \theta) + f(\theta). \qquad (7)$$

By applying the procedure described above to Eqs. (3) and (7), we obtain for the wavefront velocity

$$u \propto a^{1/2} b^{(m+n+l-2k-1)/2n}. \qquad (8)$$

However, when using this result, one should bear in mind that the ''blowup regime'' may exhibit an explosive buildup of instability when the temperature of the medium goes to infinity within a finite time ($m+n-k-1>0$) (Ref. 11).

[1] V. A. Vasil'v, Yu. M. Romanovskiĭ, and V. G. Yakhno, *Autowave Processes* [in Russian], Nauka, Moscow (1987), 240 pp.
[2] A. Yu. Loskutov and A. S. Mikhaĭlov, *Foundations of Synergetics*, 2nd ed., Springer, New York (1994–1996) [Russ. orig., Nauka, Moscow (1990), 272 pp.].
[3] A. Vl. Gurevich and R. G. Mints, Usp. Fiz. Nauk **142**(1), 61 (1984) [Sov. Phys. Usp. **27**, 19 (1984)].
[4] Yu. M. L'vovskiĭ, Pis'ma Zh. Tekh. Fiz. **15**(15), 39 (1989) [Sov. Tech. Phys. Lett. **15**, 596 (1989)].
[5] S. V. Petrovskiĭ, Zh. Tekh. Fiz. **64**(8), 1 (1994) [Tech. Phys. **39**, 747 (1994)].
[6] A. A. Pukhov, Supercond. Sci. Technol. **10**, 547 (1997).
[7] N. H. Ibragimov, *Transformation Groups Applied to Mathematical Physics* (Reidel, Dordrecht, 1985) [Russ. original, Nauka, Moscow, 1983, 280 pp.].
[8] G. W. Bluman and S. Kumei, *Symmetries and Differential Equations* (Springer-Verlag, New York, 1989).
[9] L. Dresner, *Similarity Solutions of Nonlinear Partial Differential Equations* (Pitman, London, 1983).
[10] L. Dresner, IEEE Trans. Magn. **21**, 392 (1985).
[11] A. A. Samarskiĭ, V. A. Galaktionov, S. P. Kurdyumov, and A. P. Mikhalov, *Blow-up in Quasilinear Parabolic Equations*, W. de Gruyter, New York (1995) [Russ. orig., Nauka, Moscow (1987), 477 pp.].

Translated by R. M. Durham

Influence of the specific input energy on the characteristics of a nuclear-pumped Ar/Xe laser

M. V. Bokhovko, A. P. Budnik, I. V. Dobrovol'skaya, V. N. Kononov, and O. E. Kononov

Russian State Science Center—Physics and Power Institute, Obninsk
(Submitted January 14, 1998)
Pis'ma Zh. Tekh. Fiz. **24**, 16–20 (July 26, 1998)

Results are presented of experiments and model calculations on the pumping of a 1.73 μm Ar/Xe laser with ^{235}U fission fragments over a wide range of specific powers. An analysis is made of the mechanism for quenching of the lasing at high specific input energies. © *1998 American Institute of Physics.* [S1063-7850(98)02007-2]

It has been suggested that the He/Ar/Xe mixture for which the best power characteristics (efficiency, output power) have been achieved so far, should be used as the active medium in a power prototype of a large laser facility pumped by pulses from a nuclear reactor.[1] In this case, the specific pump energy of the uranium-235 fission fragments in the laser unit will be around 1 kJ l^{-1} and the postulated laser output power may be a few tens of kilojoules, depending on the maximum specific output energy of the active medium. The specific output energy of an Ar/Xe laser achieved so far is ~1 J l^{-1} and is determined by the quenching of the lasing as the specific input energy increases. This characteristic of a laser utilizing the $5d-6p$ transitions of the Xe atom has been investigated experimentally and theoretically by various authors.[2–4] However, the energy overloading mechanism of this laser and possible methods of surmounting this problem have not yet been fully clarified.[5,6]

Here we report the first investigation of the energy characteristics of a cw Ar/Xe laser carried out in order to study the mechanisms for quenching the lasing over a wide range of specific nuclear pump powers (between 0.3 and 3 kW cm^{-3}). The kinetic processes in an Ar/Xe laser are modeled numerically to interpret the experimental results.

The experiments were carried out using the BARS-6 two-region pulsed reactor, which can deliver a thermal neutron flux density of up to 2×10^{17} cm^{-2} s^{-1} on the surface of the laser cell with a neutron pulse duration of 200 μs. The inner surface of the laser cell was coated with a thin layer of uranium-235 with a total weight of 1 g. The 550 cm^3 laser cell had antireflection-coated optical windows and was filled with a 200:1 Ar/Xe mixture at a pressure of 380 Torr. The cavity was formed by two dielectric mirrors. The 1.73 μm laser radiation was directed into an IMO-2N calorimeter located within the reactor confinement and some was fed into the experimental hall where it was recorded using germanium photodetectors and a digital storage oscilloscope.[7] The thermal neutron pulse was recorded using vacuum fission chambers[8] and the fluence was measured by the activation of gold foils. These data were used to calculate the specific input energy and the pump power for the uranium-235 fission fragments. The experiments were carried out with the laser cell in three different positions relative to the active

zones of the reactor. The peak flux density of the thermal neutrons on the surface of the cell was between 2.4×10^{16} and 2×10^{17} cm^{-2} s^{-1}, the maximum thermal neutron fluence was 5×10^{13} cm^{-2}, and the specific pump power for the fission fragments was 3 kW cm^{-3}. The maximum laser radiation energy recorded experimentally was 0.49 J and corresponded to a specific output energy of 0.9 J l^{-1} and a specific power of 5.5 kW l^{-1}.

The kinetic processes in an Ar/Xe laser pumped by fission fragments were modeled mathematically to identify the mechanism for quenching of the lasing. The kinetic model was constructed using data given in Refs. 9 and 10 and took into account 46 components involved in 389 reactions and radiative transitions. The modeling assumed that the electron energy distribution function deviated from Maxwellian, the change in the temperature of the medium was calculated during the pump pulse, and the temperature dependence of the reaction rate constants and the stimulated emission cross section was taken into account. The pump pulse power, and the parameters of the cavity and the medium were defined according to the experimental conditions.

Figure 1 gives oscilloscope traces of the pump and 1.73 μm laser radiation pulses obtained in experiments with three specific input energies, and also shows the results of the mathematical modeling. For an input energy of 0.1 J cm^{-3} energy overloading of the Ar/Xe laser shows up as a limitation of the experimentally observed output power at around 3 kW when the input energy reaches ~20 mJ cm^{-3}. In this case, the laser efficiency in terms of deposited energy is 1.5%. The output power and efficiency calculated using the kinetic model are twice the experimental values and no appreciable energy overloading occurs. An increase in the specific input energy to 0.17 J cm^{-3} substantially shortens the laser pulse (from 300 to 80 μs), approximately halves the peak power, and reduces the efficiency to 5×10^{-2}%. The calculated results also reveal energy overloading in the form of quenching of the lasing and its duration shows good agreement with that observed experimentally. No power limitation is observed in this case and the efficiency is reduced approximately threefold, to 0.8%. When the specific input energy is increased further to 0.7 J cm^{-3}, this trend is still observed. Thus, in broad terms, the experimentally ob-
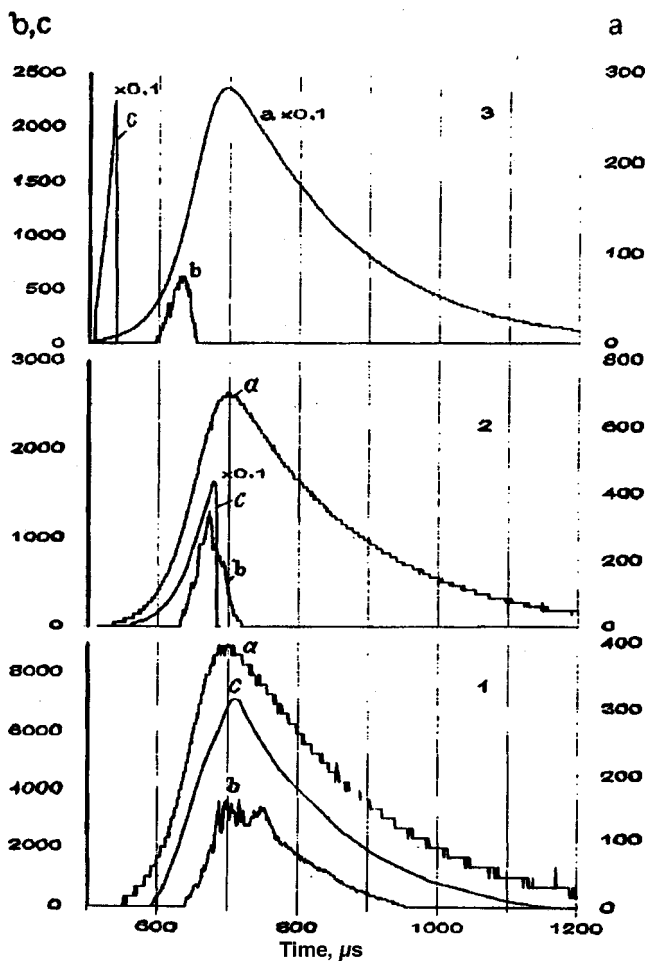
FIG. 1. Oscilloscope traces of pump (a, W cm^{-3}) and laser radiation pulses (b, W) and calculated results (c, W) for three specific input energies: *1*— 0.1 J cm^{-3}, *2*—0.17 J cm^{-3}, and *3*—0.7 J cm^{-3}.

served energy overloading of a nuclear-pumped Ar/Xe laser utilizing the 1.73 μm Xe-atom transition is fairly well reproduced by the kinetic model used for the calculations. The discrepancy between the experimental and calculated threshold and peak power may arise from the incomplete agreement between the real cavity parameters and those used for the calculations.

An analysis of the kinetic processes showed that at high pump power quenching of the lasing is caused by collisional processes involving electrons and not by an increase in the temperature of the gaseous medium. In this case, the rate of filling of Xe atoms in the upper active level drops sharply because of an increase in the electron concentration and especially their average energy, since the highly excited Xe atoms, formed as a result of dissociative recombination of ArXe ions, are predominantly ionized by electrons rather than quenched by Ar atoms accompanied by filling of the upper active level. This ultimately results in quenching of the lasing. In contrast to the proposed mechanism, the quenching of the lasing at low pump powers is attributed, as in Ref. 10, to simple mixing of the laser levels by electrons.

To sum up, these results show that the maximum specific output power of a fission-fragment-pumped Ar/Xe laser may be enhanced by incorporating molecular gas additives to reduce the electron temperature and possibly also electronegative gases to reduce their concentration. However, a reduction in the initial temperature of the gas mixture proposed in Ref. 11 is not effective.

[1] A. V. Gulevich, P. P. D'yachenko, A. V. Zrodnikov *et al.*, At. Energy **80**, 361 (1996).
[2] A. M. Voinov, L. E. Dovbysh, V. N. Krivonosov *et al.*, Dokl. Akad. Nauk SSSR **245**, 80 (1979) [Sov. Phys. Dokl. **24**, 189 (1979)].
[3] W. J. Alford and G. N. Hays, J. Appl. Phys. **65**, 3760 (1989).
[4] W. J. Alford, G. N. Hays, M. Ohwa, and M. J. Kushner, J. Appl. Phys. **69**, 1843 (1991).
[5] O. V. Sereda, V. F. Tarasenko, A. V. Fedenev, and S. I. Yakovlenko, Kvantovaya Elektron. (Moscow) **20**, 535 (1993) [Quantum Electron. **23**, 459 (1993)].
[6] A. V. Karelin, A. A. Sinyavskiĭ, and S. I. Yakovlenko, Kvant. Elektron. (Moscow) **24**, 387 (1997).
[7] V. I. Regushevskiĭ, O. E. Kononov, M. V. Bokhovko, and V. N. Kononov, Preprint No. 2478 [in Russian], Physics and Power Institute, Obninsk (1995).
[8] V. I. Regushevskiĭ, M. V. Bokhovko, V. N. Kononov *et al.*, Preprint No. 2531 [in Russian], Physics and Power Institute, Obninsk (1996).
[9] M. Ohwa, T. J. Moratz, and M. J. Kushner, J. Appl. Phys. **66**, 5131 (1989).
[10] J. W. Shon, M. G. Kushner, G. A. Hebner, and G. N. Hays, J. Appl. Phys. **73**, 2686 (1993).
[11] G. A. Hebner, IEEE J. Quantum Electron. **31**, 1262 (1995).

Translated by R. M. Durham

Use of a microconductor with natural ferromagnetic resonance for radio-absorbing materials

S. A. Baranov

T. G. Shevchenko Dnestr State University, Tiraspol

Thin radio-absorbing screens with an attenuation of 30 dB at frequencies of
8–10 GHz were fabricated using a composite with microconductor sections.
© *1998 American Institute of Physics.* [S1063-7850(98)02107-7]

The existence of natural ferromagnetic resonance in amorphous microconductors in the frequency range ~ 1–10 GHz (Refs. 1–7) has opened up the possibility of developing broad-band radio-absorbing materials. The present work treats the radio-absorbing properties of planar, thin (no more than 2 mm thick) samples made of rubber (KLTGS grade) filled with sections of microconductor (microwire dipoles). The radio-absorbing properties were investigated in the range 8–10 GHz. Note that the best results were obtained for dipoles 1–3 mm long with a core diameter $2r_c \sim 1$–$3 \, \mu$m.

The curve giving the frequency dependence of the attenuation is the same as the magnetic permeability curve of the natural ferromagnetic resonance, except that its half-width is greater (see Fig. 1). Measurements of the attenuation factor were made using the method described in Ref. 8 and the magnetic permeabilities were calculated by a method similar to that used in Ref. 6. The maximum attenuation exceeded 30 dB (a sheet of rubber without dipoles exhibits very low attenuation, no greater than 2 dB).

The investigations were made using FeBSiMnC alloys having natural ferromagnetic resonance in the range 8–10 Hz with a half-width of ~ 1–1.5 GHz and a magnetic permeability $\mu_{\mathrm{eff}} \sim 10^2$. In a certain range of dipole lengths (1–3 mm) absorption resonances were observed in the composite as a result of the dipole length l being comparable to $\lambda_{\mathrm{eff}}/2$, where λ_{eff} is the effective wavelength of the absorbed field in the composite (i.e., geometric resonance).

A disadvantage of amorphous materials based on metal alloys compared with ferrites is their high electrical conductivity. This prevents the dipole concentration in the composite from being increased substantially. The samples investigated contained no more than 5–8 g of microwire per 100 g rubber so that the absorption can only be of dipole nature.

It has also been established experimentally that strong inductive coupling exists between the dipoles,[4] which can be estimated by introducing the inductive impedance,[9]

$$Y \sim \mu \mu_0 l \, \ln\left[\frac{2l}{r_c}\right], \tag{1}$$

and its ratio to the resistance R,

$$Y/R \sim r_c^2/\delta^2, \tag{2}$$

where δ is the skin layer depth.

A reduction of r_c compared with δ may increase the absorption coefficient, since it creates the possibility of increasing the dipole concentration. Note that the width of the composite curve may be increased by using the dispersion of the magnetic susceptibility, which can extend the geometric resonance.

To sum up, the following conclusions can be drawn. Microwire has been used to fabricate composites in the form of planar radio-absorbing screens less than 2 mm thick which can operate efficiently in the range 8–11 GHz of practical interest. The use of thinner microwire can improve the characteristics of the screens by increasing the density of absorbing dipoles without increasing the effective conductivity of the sample. However, the fabrication of microwire with cores thinner than 1 μm presents technological difficulties.
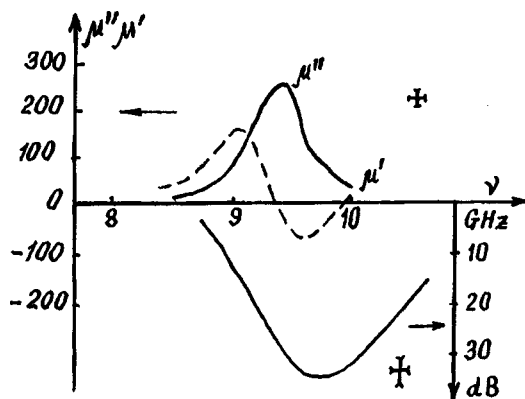

FIG. 1. Dispersion of the magnetic permeability of an amorphous microwire (left-hand ordinate) and attenuation factor for this amorphous microwire as a function of the field frequency (right-hand ordinate). The relative measurement error was less than 10% for the frequency and less than 20% for the magnetic permeability. The spread of the attenuation factor measurements was ± 5 dB.

[1] S. A. Baranov, V. I. Berzhanskiĭ, S. K. Zotov, V. L. Kokoz, V. S. Larin, and A. V. Torkunov, Fiz. Met. Metalloved. **67**(1), 73 (1989).

[2] S. A. Baranov, S. K. Zotov, V. S. Larin, and A. V. Torkunov, Fiz. Met. Metalloved. No. **12**, 172 (1991).

[3] S. A. Baranov, S. K. Zotov, V. S. Larin, and A. V. Torkunov, in *Proceedings of Young Scientists' Conference, Faculty of Physics, Lvov University*, L'vov, 1991 [in Russian], p. 5–7, Deposited Paper No. 763–UK91, 30.04.91.

[4] S. A. Baranov, Vestn. Pridnestrov. Univ. **1**(2), 126 (1994).

[5] L. G. Gazyan and L. M. Suslov, Radiotekhnika No. 7, 92 (1988).

[6] V. I. Ponomarenko, V. Zh. Berzhanskiĭ, I. V. Dzedolik, V. L. Kokoz, Yu. M. Vasil'ev, and A. V. Torkunov, Izv. Vyssh. Uchebn. Zaved. Radioélektron. **32**(3), 38 (1989).

[7] V. N. Berzhanskiĭ, I. G. Gazyan, V. L. Kokoz, and D. N. Vladimirov, Pis'ma Zh. Tekh. Fiz. **16**(12), 14 (1990) [Sov. Tech. Phys. Lett. **16**, 467 (1990)].

[8] *Electromagnetic Wave Absorbers for Chamber Shielding*, State Standard GOST R500, Nov. 1992 [in Russian], p. 1–15.

[9] P. L. Kalantarov and L. A. Tseĭtlin, *Calculation of Inductances* [in Russian], Énergoatomizdat, Moscow (1986), p. 92–99.

Translated by R. M. Durham

Thermal flicker noise in dissipative pre-melting processes in crystalline materials

L. A. Bityutskaya and G. D. Seleznev

Voronezh State University

An analysis is made of thermal fluctuations on the premelting exothermics of materials with different types of chemical bond (KCl, Ge, Sb, and Cu). Statistical and spectral parameters of the thermal fluctuations are introduced. It is shown that for these materials under certain conditions the thermal fluctuations may be identified as two-level thermal flicker noise. © *1998 American Institute of Physics.* [S1063-7850(98)02207-1]

Flicker noise, known for more than half a century, has recently attracted an upsurge of attention among researchers[1-4] because of the increasing interest being shown in problems of irreversibility, nonlinearity, and self-organization in which the fundamental role of flicker noise is becoming increasingly evident. Initially recorded as electrical noise in electronic and semiconductor devices ($p-n$ junctions, transistors, metal–semiconductor contacts),[3,4] flicker noise was later observed in an extremely diverse range of processes, ranging from fluctuations of the membrane potential of a living cell to music.[1,2]

In Refs. 5–8 a special method of digital differential thermal analysis in a dynamic mode at heating rates greater than 1 K/min with the pass band of the recorded signals controllable up to 1 Hz was used to observe transient dissipative processes which appeared as sharp-edged thermal pulses against whose background were observed low-frequency fluctuations of the temperature ΔT. These fluctuations are preserved and amplified by being held isothermally in the excitation region. The nature and parameters of the observed noise has not been studied.

The aim of the present paper is to make a spectral analysis of the thermal fluctuations of the premelting isotherms for crystalline materials with different types of chemical bonds: Cu, Sb, Ge, and KCl. The analysis was made using data obtained in Refs. 5–8, consisting of a set of readings from a differential thermocouple used to record the temperature difference between the sample and a standard, expressed in millidegrees Kelvin. The characteristic isothermal holding time was 30 min and the number of readings 1000–1500. The variance of the macroscopic thermal fluctuations for this groups of materials considerably exceeded the variance of the instrumental noise, which was 0.13 (see Table I). This means that the observed instability can be considered as a manifestation of the dynamic nature of the transient processes.[9]

The isothermal fluctuations were investigated by digital thermal analysis with the data processed by a special program using the Welch periodogram method.[10]

It should be noted that in spectral analyses of random processes[4,10] the results are represented as frequency dependences of the spectral power density S. The spectral power density is the energy characteristic of a random processes and in the calculations, the expression for S should contain the square of the amplitudes of its spectral components. However, the thermal fluctuations considered here are essentially a thermal energy release process, and in this case their spectral density, denoted as S^*, should contain an expression linear in the absolute values of the amplitude.

For all the materials, the spectrum consisted of two sections A and B approximated by straight lines for which the absolute values of the slopes satisfy $\alpha_A > 1$, $\alpha_B < 1$ and the critical frequency at which the slope changes is f_{cr} (see Fig. 1 and Table I). We draw attention to the fact that the ratio of the parameters α_B / α_A for Cu and Sb metals is close to 0.3, whereas for the semiconductor Ge and ionic crystal KCl it is close to 0.5. The presence of two sections in the spectrum suggests that the physical process generating the thermal fluctuations has two levels of the same nature.

A linear log–log dependence of the spectral power density on frequency is typical of the fluctuation process known as flicker noise.[4] The existence of two approximately rectilinear sections A and B observed on the spectra of all the materials studied suggests that the thermal fluctuations in

TABLE I.

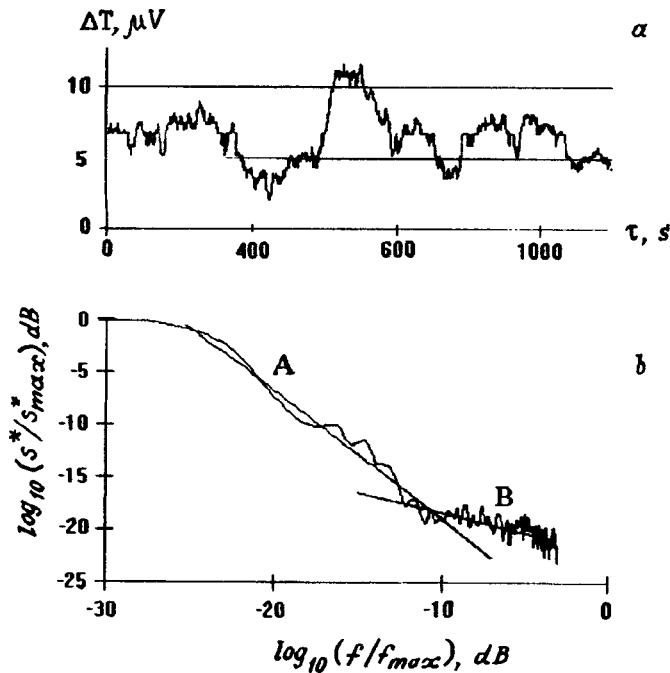| Material	Isothermal holding temperature, °C	Variance	Spectral characteristics			
			α_A	α_B	α_B / α_A	f_{cr}, Hz
Cu	1047	3.56	1.25	0.38	0.30	0.085
Ge	949	2.94	1.02	0.5	0.50	0.056
Sb	584	0.78	1.4	0.42	0.30	0.042
KCl	762	2.47	1.1	0.52	0.47	0.115

FIG. 1. Fluctuations of the heat release during isothermal premelting of copper: a—thermogram during holding at 1047 °C, b—relative spectral power density of the fluctuations $\log_{10}(S^*/S^*_{max})$ versus the relative frequency $\log_{10}(f/f_{max})$, where f_{max} and S^*_{max} are maxima.

regions of excitation at the premelting stage of crystalline materials may be identified as two-level thermal flicker noise. Two levels of flicker noise were also observed in experiments to study electric current fluctuations[11] but unlike the thermal fluctuations, the relationship $\alpha_A < \alpha_B$ was found in this case.

Since the characteristics that identify isothermal thermal fluctuations at the premelting stage as flicker noise are independent of the type of chemical bond, this indicates that the phenomenon is universal. At the same time, the parameters of these fluctuations introduced—the variance, the spectral density characteristics α_A and α_B, and the critical frequency f_{cr}—while preserving the general features, have their own characteristic values under given conditions and thus may serve as typical indications of the particular material.

[1] S. F. Timashev, Ross. Khim. Zh. **61**(3), 17 (1997).

[2] Yu. L. Klimontovich, *Statistical Theory of Open Systems* [in Russian], TOO ''Yanus'', Moscow (1995), p. 624.

[3] G. N. Bochkov and Yu. E. Kuzovlev, Usp. Fiz. Nauk **141**(1), 151 (1983) [Sov. Phys. Usp. **26**, 829 (1983)].

[4] M. J. Buckingham, *Noise in Electronic Devices and Systems* (Halsted Press, New York, 1983; Mir, Moscow, 1986).

[5] L. A. Bityutskaya and E. S. Mashkina, Pis'ma Zh. Tekh. Fiz. **21**(17), 85 (1995) [Tech. Phys. Lett. **21**, 720 (1995)].

[6] L. A. Bityutskaya and E. S. Mashkina, Pis'ma Zh. Tekh. Fiz. **21**(18), 8 (1995) [Tech. Phys. Lett. **21**, 728 (1995)].

[7] L. A. Bityutskaya and E. S. Mashkina, Pis'ma Zh. Tekh. Fiz. **21**(20), 30 (1995) [Tech. Phys. Lett. **21**, 828 (1995)].

[8] L. A. Bityutskaya and E. S. Mashkina, Pis'ma Zh. Tekh. Fiz. **21**(24), 90 (1995) [Tech. Phys. Lett. **21**, 1032 (1995)].

[9] S. É. Shnol', É. V. Pozharskiĭ *et al.*, Ross. Khim. Zh. **61**(3), 30 (1997). S. 30–36.

[10] S. L. Marple, Jr., *Digital Spectral Analysis with Applications* (Prentice-Hall, Englewood Cliffs, N. J., 1987; Mir, Moscow, 1990).

[11] R. F. Voss and J. Clarke, Phys. Rev. Lett. **13**, 556 (1976).

Translated by R. M. Durham

Distribution laws for microplastic deformations

V. V. Ostashev and O. D. Shevchenko

Pskov Polytechnic Institute
(Submitted January 23, 1998)
Pis'ma Zh. Tekh. Fiz. **24**, 28–30 (July 26, 1998)

Calculations and construction of bispectra are used to show that the deviation of the probability density of microplastic deformations from a normal distribution law is a measure of the evolution of synchronization effects and a measure of the completeness of the relaxation processes determining the plasticity of the material. © *1998 American Institute of Physics.*
[S1063-7850(98)02307-6]

The oscillating nature of plastic deformations at local structural levels may be described by the parameters of latent oscillatory processes (amplitude, frequency, phase), while the interaction of deformation defects on different scale levels is represented by the superposition and overlap of random quantities with different distribution laws.[1] The probability density distribution of microplastic deformations under the conditions of a factor experiment depends on the load parameters. For samples having maximum strength characteristics, this distribution is close to normal over the entire range of deformations in translational and rotational modes. For samples exhibiting maximum plasticity an estimate of the distribution law using the Pearson criterion suggests that the hypothesis put forward in Ref. 1 is unreliable. The distribution begins to deviate from normal for the rotational modes ω_z and then embraces the translational modes γ_{xy} and ε_{xx}.

We conjecture that random microdeformations obey a normal law as long as they predominate among the many factors responsible for inhomogeneity of the microplastic deformation field. One such factor at the wave interaction level is synchronization, which reduces the dispersion of the group velocity of the deformation defects and thus causes the evolution of macrorotations.[2,3]

The measure of the nonlinearity of the interactions of microplastic deformations and the contribution of synchronization was estimated by calculating the bispectra (see Fig. 1). The bispectrum reflects the Fourier transformation of the centered third-order correlation function

$$B(f_1,f_2)=\left(\frac{1}{2\pi}\right)^2 \int \int_{-\infty}^{\infty} R(\tau_1,\tau_2)$$

$$\times \exp[-i(f_1\tau_1+f_2\tau_2)]d\tau_1 d\tau_2,$$

where $R(\tau_1,\tau_2)=\langle x(t)x(t+\tau_1)x(t+\tau_2)\rangle$ is a third-order correlation function averaged over the ensemble. For a process with a normal distribution law the third moment (asymmetry) is zero. In this case, we have $\langle x^3(t)\rangle=R(0,0)=0$ and thus $B(1,2)=0$. The bispectrum therefore shows how the deviations of the process from Gaussian are ''expanded'' over frequency, i.e., occur as a result of various frequencies obtained under phase matching conditions $f_1+f_2+f_3=0$.

In general, the model of a polycrystalline deformable material at the statistical interaction stage is a system for which each level may be represented by linear and nonlinear components, and thus the distribution law of the microplastic deformations approaches normal to the extent that linearity is present at a given structural level. Quite clearly, the deviation from normal may be defined as a measure of the evolution of synchronization processes and as a measure of the relaxation processes. Accordingly, a deformable material shows a specific combination of strength and plasticity characteristics.
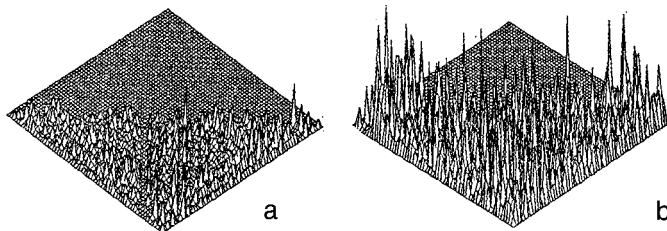

FIG. 1. Calculated bispectra for samples: a—with maximum strength and b—with maximum plasticity.

[1] V. V. Ostashev and O. D. Shevchenko, Abstracts of Papers presented at the 32nd Seminar ''Topical Strength Problems,'' St. Petersburg, 1996 [in Russian], pp. 35–36.
[2] Yu. I. Meshcheryakov, *New Methods in the Physics and Mechanics of Deformable Solids* [in Russian], Tomsk (1990), pp. 33–43.
[3] C. L. Nikias and M. R. Raghuver, Proc. IEEE **75**, 869 (1987).

Translated by R. M. Durham

Time evolution of three-crystal x-ray spectra during fluorination of a Pt/LaF$_3$/Si structure

A. A. Nefedov, S. E. Sbitnev, and S. S. Fanchenko

"Kurchatov Institute" Russian Science Center, Moscow
(Submitted January 8, 1998)
Pis'ma Zh. Tekh. Fiz. **24**, 31–34 (July 26, 1998)

A qualitative change was observed in the three-crystal x-ray spectra during fluorination of a Pt/LaF$_3$/Si structure. This may be attributed to smoothing of the surface of the platinum film, most likely as a result of the formation of platinum tetrafluoride which may undergo partial volatilization or partial dissociation with the sublimation of platinum. © *1998 American Institute of Physics.* [S1063-7850(98)02407-0]

A metal–ionic conductor–semiconductor structure with a solid LaF$_3$ electrolyte as the below-gate layer is a promising sensor to determine concentrations of toxic gases such as fluorine and hydrogen fluoride in the atmosphere.[1,2] The crystalline perfection of the interfaces and the quantitative characteristics of the surface roughness of these structures may be determined by analyzing spectra[3,4] obtained by three-crystal x-ray spectroscopy (TXS).[5] This technique involves measuring the intensity of an x-ray flux reflected successively by all three crystals (a crystal monochromator, the sample, and a crystal analyzer) as a function of the angle of rotation of the crystal analyzer θ_3 for a fixed angle of deviation α of the crystal from the exact Bragg angle. The rocking curve usually consists of three peaks: a principal peak, a pseudopeak, and a diffuse peak. The principal peak is caused by diffraction reflection from the crystal being studied, the pseudopeak characterizes the diffraction reflection curve from the crystal monochromator, and the diffuse peak is assigned to scattering of x-rays from defects in the crystal structure of the sample.

Three-crystal x-ray spectroscopy was used in Ref. 6 to study the characteristics of a Pt/LaF$_3$/Si sensor in air. It was shown that the thickness of the LaF$_3$/Si interface at which distortion of the silicon crystal structure was observed did not exceed 0.5 nm and the characteristic roughness of the platinum film on the surface of the lanthanum trifluoride was of the same order as the average thickness of this film, which was estimated as 40 nm. The possibility of carrying out TXS experiments in a controlled gaseous medium[7] makes this method extremely promising for studies of the kinetics of gas–surface interaction processes and especially for refining the mechanisms of the electrochemical reactions which take place at the three-phase interface of a metal–ionic conductor–semiconductor sensor with an active gas medium. Here we present the first results of a TXS study of a Pt/LaF$_3$/Si structure during fluorination.

Films of LaF$_3$ were grown on the (111) surface of a silicon single crystal by high-vacuum thermal vapor-phase deposition at a substrate temperature of 550 °C and the platinum film was deposited by magnetron sputtering in an argon plasma. For a sensor with high sensitivity the gas/Pt/LaF$_3$ interface should be three-phase which was achieved by successive annealing in air at 350 °C. The sample was placed in a hermetically sealed chamber which had gas inlet and outlet tubes, and x-ray transparent windows. The chamber was attached to the sample holder of a standard three-crystal spectrometer, after which one tube was connected to a pump which created a vacuum of 20 Torr in the chamber and the second tube was connected to a chamber containing crystalline XeF$_2$ powder. This substance is highly volatile at room temperature and has a partial pressure of gaseous xenon difluoride of around 2.5 Torr. Xenon difluoride has similar reaction properties to fluorine and this suggests that the fluorination of platinum by xenon difluoride with the formation of barely volatile platinum tetrafluoride is similar to the reaction with pure fluorine. The presence of water vapor in the chamber (the humidity was not monitored in this experiment) may substantially accelerate the formation of platinum tetrafluoride, even at room temperature. The use of XeF$_2$ instead of pure fluorine considerably simplified the apparatus and as a result we were able to measure the TXS spectra *in situ* during fluorination of the Pt/LaF$_3$/Si structure.

A series of TXS experiments was carried out at a fixed angle of deviation of the sample $\alpha = 100''$ from the exact Bragg angle (for silicon $\theta_B = 14.22°$) at intervals of around 10 min, after XeF$_2$ was admitted to the chamber. The measurements were made using CuK$_\alpha$ radiation at the wavelength $\lambda = 1.54$ Å. The experimental results are plotted in Fig. 1. It can be seen that the diffuse peak (*3*) decreases and almost completely disappears with time while the principal peak (*1*) increases in amplitude and becomes increasingly narrow. It should be noted that whereas this peak is almost indistinguishable from the background of the diffuse peak on the initial curves, for fairly large angles of deviation of the sample α this principal peak is clearly discernible, as was confirmed in another series of experiments.[6] Nevertheless, this substantial change in the profile of the principal peak is accompanied by no change in its area, which indicates that no changes take place at the silicon–lanthanum trifluoride interface (the thickness of this interface is of the order of 0.5 nm). The high intensity of the diffuse peak may be attributed to scattering of x-rays at inhomogeneous of the LaF$_3$/Si in-
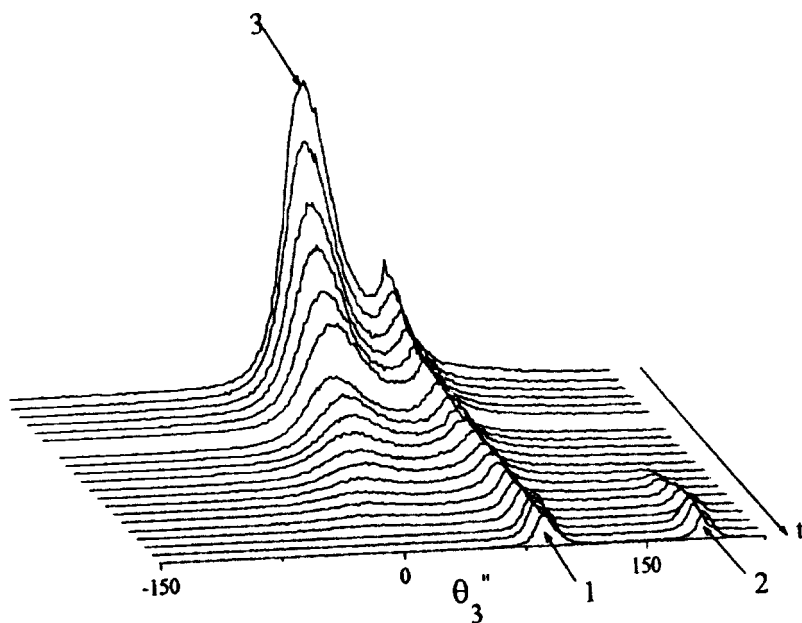
FIG. 1. Intensity of x-ray flux reflected successively from three crystals as a function of the angle of rotation θ_3 of the crystal analyzer obtained *in situ* during fluorination: *1*— principal peak, *2*—pseudopeak, *3*—diffuse peak (angle of deflection of sample $\alpha = 100''$, *t*—time after admission of XeF_2 to chamber, the curves were taken at 10 min intervals).

terface induced by stresses in the LaF_3 which were either created by the annealing of the platinum film or as a result of the buildup of nonuniform electric charge at the three-phase gas/Pt/LaF_3 interface. The high intensity of the pseudopeak compared with the principal one is caused by small-angle scattering of the wave incident on the inhomogeneous platinum film.[4] Thus, the decrease in the diffuse peak and the narrowing of the principal peak may indicate that the rough platinum surface becomes smoothed to specular during the experiment, which lasted around 3 h. This smoothing of the platinum surface is most likely caused by the formation of platinum tetrafluoride, which may partially volatilize and partially dissociate with the sublimation of platinum. Measurements of the TXS spectra after prolonged (two weeks) holding in air showed that the spectral profile does not undergo any further change, which indicates that this process is irreversible. The form of these spectra is almost the same as the TXS spectra obtained in another series of measurements for LaF_3/Si structures without the upper platinum layer both before and after fluorination under similar conditions (these spectra showed little variation in the course of fluorination).

[1] S. Krause, W. Moritz, and I. Grohmann, Sens. Mater. **9**, 191 (1992).
[2] W. Moritz, S. Krause, A. A. Vasiliev *et al.*, Sens. Mater. **24−25**, 194 (1995).
[3] A. M. Afanas'ev, M. V. Koval'chuk, É. F. Lobanovich *et al.*, Kristallografiya **26**, 28 (1981) [Sov. J. Crystallogr. **26**, 13 (1981)].
[4] P. A. Aleksandrov, A. M. Afanas'ev, and M. K. Melkonyan, Kristallografiya **26**, 1275 (1981) [Sov. J. Crystallogr. **26**, 725 (1981)].
[5] A. Iida and H. Kohra, Phys. Status Solidi A **51**, 533 (1979).
[6] A. A. Nefedov, S. S. Fanchenko, I. A. Shipov *et al.*, Poverkhnost' No 3, (*in press*) (1998).
[7] A. A. Nefedov, A. E. Rzhanov, V. I. Filippov *et al.*, Pis'ma Zh. Tekh. Fiz. **14**(5), 453 (1988) [Sov. Tech. Phys. Lett. **14**, 203 (1988)].

Translated by R. M. Durham

Phase instability and nonlinear effects in a mechanically synthesized FeB nanocrystalline alloy

V. A. Tsurin and V. A. Barinov

Institute of Metal Physics, Ural Branch of the Russian Academy of Sciences, Ekaterinburg
(Submitted January 13, 1998)
Pis'ma Zh. Tekh. Fiz. **24**, 35–40 (July 26, 1998)

Results are presented of investigations of the processes taking place during the mechanical formation of FeB alloy. It was observed that there are critical rates of introduction of damage and defect concentrations above which the system becomes unstable and two branches of nonequilibrium steady states appear. During grinding, transitions of a cyclic nature are observed between these states. It is noted that the evolution of the system is determined by the dynamics of the fluctuations and in this sense, the mechanical synthesis reaction may be unpredictable. It is established that the powder grinding process and mechanical formation of an alloy from atomic components cannot be treated on a purely mechanical or mechanochemical basis. They must be viewed as part of the general problem of nonlinear dynamic systems far from thermodynamic equilibrium. © *1998 American Institute of Physics.*
[S1063-7850(98)02507-5]

In mechanical alloy formation, the system continuously absorbs energy, some of which is dissipated in irreversible processes. Nonthermal processes also take place, such as chemical or topological disordering as a result of successive substituting collisions. The frequency of these elementary events is proportional to the rate of introduction of damage and is substantially higher than that under thermal equilibrium conditions. In consequence, systems exposed to mechanical action may be treated as dissipative systems far from equilibrium, the theory of which has attracted particular attention over the last two decades.[1,2] Systems far from equilibrium may undergo nonequilibrium phase transitions (i.e., transitions between nonequilibrium states) when the controlling parameters pass through certain critical values. Here we investigate the processes of synthesis and breakup of alloys in a FeB system as a function of the energy saturation of the alloy formation process and study how nonequilibrium states form in this system.

A mixture of Fe and B powder was treated mechanically in a Pulverizette centrifugal planetary mill. The degree of action was varied according to the ratio of the mass of the grinding balls (m_b) to the powder mass (m_p), $A = m_b/m_p$ and also by the speed of rotation of the mill and the treatment time. Two standard regimes were used to form an alloy of the FeB powder. In the high-speed treatment regime (HST), the speeds of rotation of the mill platform and the container were 450 and 850 rpm, respectively, while for the low-speed treatment (LST) these speeds were 200 and 380 rpm, respectively. The structural phase state of the FeB powder was investigated by Mössbauer spectroscopy at various stages of the mechanical treatment. Nuclear gamma ray spectra of the FeB powder were obtained at 300 K using a ^{57}Co source in a Cr matrix using a spectrometer and a resonance scintillation detector. A computer program was used for the

model calculations and to reconstruct the density function $P(H)$.[3]

The progress of mechanochemical reactions in a mixture of elemental Fe and B components is determined by the composition and by the mechanical treatment conditions.[4] Here, we investigate for the first time the alloy formation process in a mixture of iron and boron powders having the nominal composition Fe+60 at.% B after high-speed treatment for 45 h with the ratio $A = 13$ (13 HST). The results of the model calculations of the Mössbauer spectra are presented in Table I. The parameters obtained are similar to those given in Refs. 5 and 6 for nanocrystalline iron. The ratio of the subspectra $S_1/S_2 = 1$ indicates that ^{57}Fe resonant nuclei localized along grain boundaries make a significant contribution. For this area ratio, the density of the boundaries may be 10^{18}–10^{21} cm^{-3}. It is known that the dispersion process has an appreciable influence on the mobility of the atoms. It was shown in Ref. 7 that the coefficient of intragranular diffusion D of boron in iron at 110 °C is $D = 2.6 \times 10^{-19}$ m^2/s. In the nanocrystalline state, the diffusion coefficient increases to $D = 2.6 \times 10^{15}$ m^2/s and is comparable with the value of D along the grain boundaries. Thus, an analysis of the nuclear gamma ray spectrum suggests that the

TABLE I. Calculated experimental spectrum of mechanically synthesized Fe+60 at.% B alloy after high-speed treatment for 45 h in a planetary mill (13 HST).

Parameters of nuclear gamma spectrum	Subspectrum 1	Subspectrum 2
I.S., mm/s	0.292	0.266
G, mm/s	0.38	1.46
H, kOe	235	233
S, %	48	52

I.S.—isomeric shift relative to Fe; *G*—width of 1.6 lines of the nuclear gamma spectrum; *H*—hyperfine field; *S*—relative area of the subspectra.
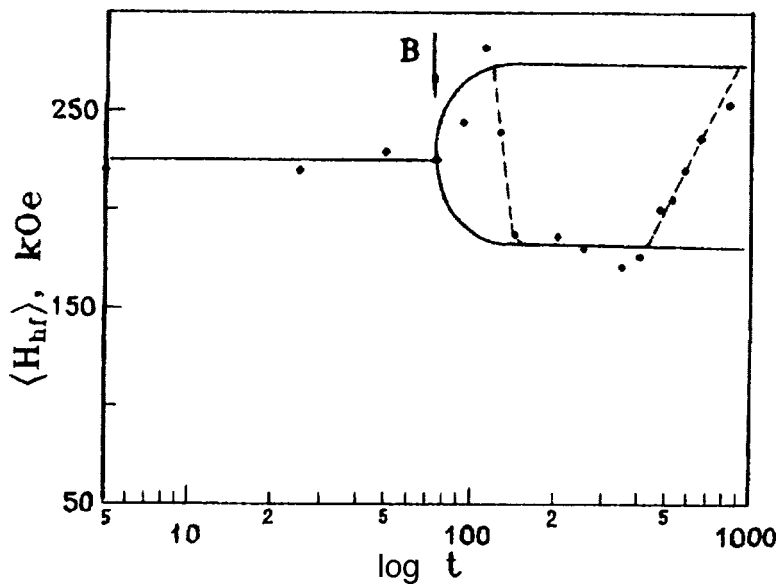
FIG. 1. Average hyperfine field $\langle H_{hf} \rangle$ of mechanically synthesized nanocrystalline Fe+60 at.% B alloy samples as a function of the grinding time in the 50 LST regime. The arrow indicates the bifurcation point B (splitting) where the branch splits into two nonequilibrium states. The dashed curve shows the transitions between these two states.

initial state of the synthesized Fe+60 at.% B alloy is characterized by high diffusion mobility of the boron atoms. The absence of α-Fe lines in the spectrum and the presence of a sextet with a field corresponding to $Fe_{67}B_{33}$ indicates that an appreciable fraction of the boron in the sample is in the free state, forming no chemical bond with Fe atoms.

In order to investigate phase transitions and the boron dissolution process, the initial synthesized Fe+60 at.% B powder was then subjected to further low-speed mechanical treatment with $A = 50$ (50 LST). This regime was used to reduce the local heating temperature of the powder particles and the formation of Fe_2B and FeB intermetallides.

The efficiency of the alloy formation process, phase transitions, and the concentrations of the components in the phases at the different stages of mechanical treatment may be assessed from the dependence of $\langle H_{hf} \rangle$ on the average boron concentration in the sample.[8] Figure 1 gives the average hyperfine field $\langle H_{hf} \rangle$ obtained by reconstructing the function $P(H)$ from the experimental nuclear gamma ray spectra of the samples plotted as a function of the grinding time. It can be seen that the dependence is nonmonotonic. After a certain time (110 h) the value of $\langle H_{hf} \rangle$ increases abruptly as a result of the decomposition of the initial synthesized nanocrystalline Fe+33 at.% B solid solution with the release of elemental Fe and B. An increase in the mechanical treatment time causes further dissolution of the boron with the formation of a near-equatomic phase in the amorphous state. Treatment above 400 h causes a phase transition in $Fe_{50}B_{50}$ regions to form an $Fe_{66}B_{33}$ solid solution with the release of B and Fe, i.e., the process observed at the initial stages of grinding is repeated. Figure 2 gives a three-dimensional representation of the distribution function of the hyperfine field $P(H)$ as a function of the mechanical treatment time for the 50 LST regime. The redistribution of the peaks corresponding to the Fe_2B ($Fe_{66}B_{33}$), Fe, FeB ($Fe_{50}B_{50}$) concentrations illustrates the nonequilibrium phase transitions in the system.

We postulate that the increase in the internal energy with increasing deformation and increasing work expended is

caused by the formation of lattice defects. An increase in the treatment time of the nanocrystalline alloy in the less energy-stressed regime (50 LST) has the result that the rate of defect formation is higher than their rate of relaxation because of the reduced local heating temperature of the sample. This leads to intensive mixing of atoms of different species and abruptly increases the rate of mass transfer. In the initial nanocrystalline alloy and also after a short grinding time (>110 h) a single state is established ($Fe_{66}B_{33}$ solid solution) exhibiting asymptotic stability, since in this region the system is capable of suppressing internal fluctuations or ex-
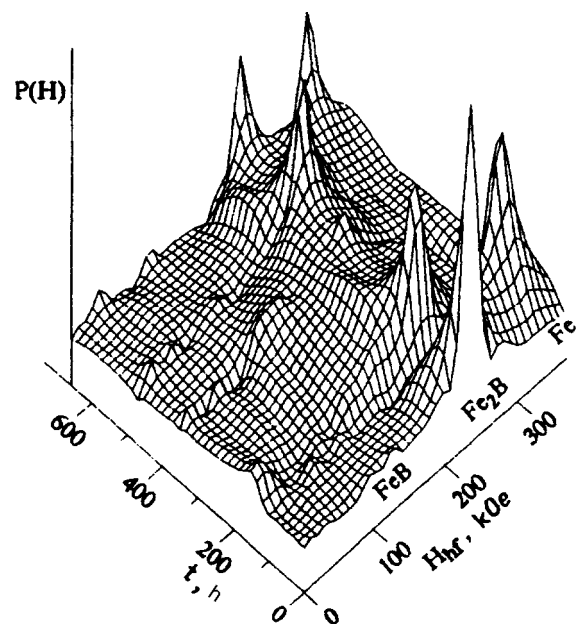

FIG. 2. Three-dimensional representation of the hyperfine field distribution function $P(H)$ as a function of the mechanical treatment time t in the planetary mill in the 50 LST regime. The redistribution of the peaks of the corresponding concentrations illustrates the phase transitions between the two nonequilibrium states.

ternal perturbations. For this reason, this branch of states is called the thermodynamic branch.[1] After a certain critical concentration of lattice defects is reached the crystal structure of the treated material becomes unstable, since the fluctuations or small external perturbations are not suppressed. The system departs from the standard state and is converted to a state far from thermodynamic equilibrium. The instability in the nonlinear region far from equilibrium is observed as splitting (bifurcation, indicated by the arrow in Fig. 1) of the thermodynamic branch into two branches of nonequilibrium steady states. The solution is determined randomly at the instant of instability via the fluctuation dynamics, and in this sense is unpredictable. The stabilization of some particular fluctuation determines the evolution of the system. This means that even as a result of small perturbations caused, for example, by some change in the treatment regime or the

presence of oxides,[9] the alloy formation reaction may take place by different methods.

[1] G. Nicolis and I. Prigogine, *Self Organization in Nonequilibrium Systems* (Wiley, New York, 1977).
[2] A. S. Balankin, *Synergetics of a Deformable Solid* [in Russian], MO SSSR, Moscow (1991), 358 pp.
[3] V. I. Nikolaev and V. S. Rusakov, *Mössbauer Investigations of Ferrites* [in Russian], Moscow State University Press, Moscow (1985), pp. 21–44.
[4] J. S. Benjamin, Met. Sci. Forum **88−90**, 1 (1992).
[5] U. Herr, J. Jing, R. Birringer, U. Gonser, and H. Gleiter, Appl. Phys. Lett. **50**, 472 (1987).
[6] W. Schlump and H. Grewe, Techn. Mitteil. Krupp **47**(2), 69 (1989).
[7] H. J. Hofler, R. S. Averback, and H. Gleiter, Philos. Mag. Lett. **68(2)**, 99 (1993).
[8] C. L. Chein and K. M. Unruh, Phys. Rev. B **25**, 5790 (1982).
[9] J. Balogh, L. Bujdoso, G. Faigel *et al.*, Nanostruct. Mater. **2**, 11 (1993).

Translated by R. M. Durham

Phase transition waves in strong electric fields

N. I. Kuskova

Institute of Pulsed Processes and Engineering, National Academy of Sciences of Ukraine, Nikolaev

A description is given of a semiphenomenological theory which yields an expression for the velocity of a phase transition wave in a condensed medium exposed to a strong electric field. The proposed theory may be applied to analyze an electron avalanche breakdown wave or a melting (evaporation) wave formed in a material under the action of an electric discharge. © *1998 American Institute of Physics.* [S1063-7850(98)02607-X]

The action of strong electromagnetic fields on condensed media may result in the following types of phase transitions: 1) melting and (or) evaporation as a result of electric breakdown of solid (or liquid) weakly conducting media and electrical explosion of conductors and 2) insulator–semiconductor or semiconductor–metal transitions as a result of electric discharges in insulators and high-resistivity semiconductors, which under certain conditions propagate as waves.[1–6]

An analysis will be made of phase transition waves processes involving the propagation of local regions of strong electromagnetic field variation where some phase transition takes place.

Let us determine the propagation velocity of a phase transition wave. We write the general one-dimensional continuity equation describing the change in some physical characteristic of the medium f (such as the internal energy ε, electrical conductivity σ, carrier concentration n, or density ρ) as a result of a phase transition which takes place under the action of a strong electric field. Denoting the rate of change of the parameter f by $w = w(E)$ (E is the electric field strength) and the flow velocity of the medium by v, we then have

$$\frac{\partial f}{\partial t} \pm v \, \frac{\partial f}{\partial r} = w. \tag{1}$$

We shall assume that the characteristic size of the region of field uniformity in which the characteristic f changes abruptly is δ. By means of the change of variables $z = r \pm ut$, where u is the wave propagation velocity, we obtain

$$u \cong \frac{w \delta}{\Delta f} \pm v, \tag{2}$$

where $\Delta f = |f_{\max} - f_0|$, f_0 is the initial distribution.

If the flow of the medium is "opposite" to the phase transition wave, there exists a threshold field strength E^* at which the phase transition wave can propagate. This threshold value E^* is determined from the condition $u > 0$, i.e., $w(E^*)\delta/\Delta f - v > 0$.

1. In ultrafast electrical explosions of conductors, the current distribution becomes highly nonuniform as a result of the formation and explosion of the skin layer. The character-

istic size of the region of current density nonuniformity j is equal to the width of the skin layer $\delta_j = (0.5\mu\sigma\omega)^{-1/2}$, where μ is the magnetic permeability and ω is the frequency of the current fluctuation.[7] The mechanism of wave displacement involves expulsion of the current from the skin layer in which the electrical conductivity drops sharply when the metal is heated by the high-density current. The rate of energy release is determined from the Joule heating rate $w(E) = \sigma E^2/\rho$, and formula (2) then yields an expression to estimate the velocity of the so-called current wave[3] through the conductor

$$u \cong \frac{\sigma E^2 \delta}{\rho \Delta \varepsilon}, \tag{3}$$

where $\Delta\varepsilon$ is the change in the internal energy of the metal in the skin layer and $v = 0$ since the layer in which the current wave propagates is cold.

2. In weakly nonuniform electrical explosions of conductors, such as the so-called fast regimes, all the characteristics of a cylindrical conductor in either the solid and liquid states are uniform except for the magnetic pressure. Since the boiling point depends weakly on pressure, volume expansion cannot take place even with uniform heating. Thus, the propagation of evaporation in the form of a phase transition wave moving from the outer boundary to the axis of the conductor is caused by the nonuniformity of the pressure p. The width of the evaporation wavefront in this case is given by

$$\delta_p = \frac{\lambda}{cP(0)} \frac{dP}{dT_b} \frac{a^2}{2r}, \tag{4}$$

where λ is the latent heat of evaporation, c is the specific heat of the liquid metal, $P(0)$ is the pressure on the conductor axis, dP/dT_b is the change in pressure and boiling point along the liquid–gas phase equilibrium curve, a is the radius of the conductor, and r is the instantaneous position of the wavefront.

Since the temperature of the conductor is uniform before the onset of boiling, the change of the specific internal energy at the front of the phase transition wave is $\Delta\varepsilon = \lambda$ and the velocity of this wave is given by

$$u \cong \frac{\sigma E^2 \delta_p}{\rho \lambda} - v. \tag{5}$$

3. We shall now consider the phase transition waves generated in the electrical breakdown of weakly conducting media, as a result of melting and (or) evaporation of the material which causes gas bubbles. An electric discharge takes place in this gas within a time much shorter than that needed to form the bubbles and results in the generation of a plasma at the front of the phase transition wave. The width of the front δ_E is determined by the geometry of the discharge gap and the plasma channel. In this case, the propagation velocity of the phase transition wave can be estimated from

$$u \cong \frac{\sigma E^2 \delta_E}{\rho \Delta \varepsilon} + v, \tag{6}$$

where $\Delta \varepsilon$ is the change in the specific energy of the material.

4. The propagation of plasma channels in insulators and semiconductors at supersonic velocities exceeding the carrier drift velocities indicates that the processes taking place in the streamer discharge are of a wave nature. The motion of the streamer in the interelectrode gap constitutes an ionization wave at whose front the carrier concentration changes substantially by $\Delta n = n_{max} - n_0 \cong n_{max} = (\varepsilon w^0/(e\mu))^{1/2}$ in a strong electric field (when the ionization rate is considerably higher than the recombination velocity).[8] Expression (2) for the velocity of the ionization wave then has the form[6]

$$u \cong \frac{w^0 \delta_E}{n_{max}} + v, \tag{7}$$

where $w^0 = w(E_{max})$ is the rate of generation of electron–hole pairs (as a result of tunneling, impact ionization, the Frenkel effect, or photoionization) and v is the electron velocity.

To sum up, the similarity between the electrical explosion of conductors and the electrical breakdown of insulators and semiconductors can be attributed to their being caused by the same mechanism: a phase transition wave at whose front the electrical conductivity changes considerably, falling sharply in the electrical explosion of conductors and increasing by several orders of magnitude in electrical breakdown. For the same geometry and times of action of the electromagnetic field, the phase transition waves formed in condensed media have common relationships and spectra of propagation velocities—supersonic and subsonic—depending on the field strength and the type of medium.

[1] V. Ya. Ushakov, *Pulsed Electrical Breakdown in Liquids* [in Russian], Tomsk State University Press, Tomsk (1975), 258 pp.

[2] N. I. Kuskova, Zh. Tekh. Fiz. **53**, 924 (1983) [Sov. Phys. Tech. Phys. **28**, 591 (1983)].

[3] V. A. Burtsev, N. V. Kalinin, and A. V. Luchinskiĭ, *Electrical Explosion of Conductors and Applications to Electrophysical Systems* [in Russian], Moscow (1990), 288 pp.

[4] F. D. Bennet, Phys. Fluids **8**, 1425 (1965).

[5] N. I. Kuskova, S. I. Tkachenko, and S. V. Koval, J. Phys.: Condens. Matter **9**, 6175 (1997).

[6] N. G. Basov, A. G. Molchanov, A. S. Nasibov *et al.*, Zh. Eksp. Teor. Fiz. **70**, 1751 (1976) [Sov. Phys. JETP **43**, 912 (1976)].

[7] Yu. V. Novozhilov and Yu. A. Yappa, *Electrodynamics*, Mir, Moscow (1981).

[8] V. V. Vladimirov, V. N. Gorshkov, O. V. Konstantinov, and N. I. Kuskova, Dokl. Akad. Nauk SSSR **305**, 586 (1989) [Sov. Phys. Dokl. **34**, 242 (1989)].

Translated by R. M. Durham

Optical properties of the polarized Dirac vacuum

S. G. Oganesyan

"Laser Engineering" Scientific-Industrial Organization, Erevan
(Submitted July 7, 1997; resubmitted January 22, 1998)
Pis'ma Zh. Tekh. Fiz. **24**, 45–47 (July 26, 1998)

An investigation is made of the propagation of laser radiation through the Dirac vacuum polarized by a strong electric field. Calculations are made of the refractive index of the vacuum and the angle of rotation of the plane of polarization of the radiation. The possibility of measuring strong electric fields is assessed. © *1998 American Institute of Physics.*
[S1063-7850(98)02707-4]

The optical properties of free electron beams (Ref. 1, Sections 13 and 48) can be used to study their internal structure. We note that, according to Dirac,[2] the vacuum is a set of free electrons filling all possible negative-energy levels. Here it is shown that the optical properties of the Dirac vacuum can be used to study (especially to measure the strengths of) very strong fields $E_0 < E_{cr} = m^2 c^3 / e\hbar = 1.3 \times 10^{16}$ V/cm (in the opposite case $E_0 > E_{cr}$ breakdown of the vacuum occurs). Let us assume that the Dirac vacuum is polarized by a strong static electric field $\mathbf{E}_0$ and elliptically polarized laser radiation passes through this region:

$$E_{1x} = E_1 \sin(\omega t - kz), \quad E_{1y} = E_2 \cos(\omega t - kz). \quad (1)$$

We shall describe this system using the Heisenberg–Euler Lagrangian[2] expanded as a series to the fourth order with respect to the field,

$$L' = R[(\mathbf{E}^2 - \mathbf{H}^2)^2 + 7(\mathbf{EH})^2].$$

Here we have $R = \alpha / 360 \pi^2 E_{cr}^2$, $\alpha = e^2 / \hbar c$, $\mathbf{E} = \mathbf{E}_0 + \mathbf{E}_1$, and $\mathbf{H} = \mathbf{H}_1$. Note that this Lagrangian is suitable for describing static and variable fields if the frequency of the latter satisfies the condition $\omega \ll mc^2 / \hbar$ (Ref. 3). Let us now calculate the polarization $\mathbf{P} = \partial L' / \partial \mathbf{E}$ and the magnetization $\mathbf{I} = \partial L' / \partial \mathbf{H}$ of the Dirac vacuum. Then collecting in the current $\mathbf{j} = c \,\mathrm{curl}\, \mathbf{I} + \partial \mathbf{P} / \partial t$ those terms oscillating at the frequency ω and substituting these into the Maxwell equation, we find the tensors of the permittivity and magnetic permeability of the Dirac vacuum,

$$\varepsilon_{ij} = (1 + 8\pi R E_0^2)\delta_{ij} + 16\pi R E_{0i} E_{0j},$$

$$\mu_{ij} = (1 - 8\pi R E_0^2)\delta_{ij} + 56\pi R E_{0i} E_{0j} \quad (2)$$

(note that in the calculations we neglected the influence of the Dirac vacuum on the field $\mathbf{E}_0$). In order to simplify the following analysis, we assume that the field $\mathbf{E}_0$ is directed along the x axis. In this case, the equations for the x and y projections of the field are separated

$$\frac{\partial^2 E_{x,y}}{\partial z^2} - \frac{1}{c^2} \frac{\partial^2 E_{x,y}}{\partial t^2} = \frac{4\pi}{c} \frac{\partial j_{x,y}}{\partial t},$$

where $j_x = 4 R E_0^2 \partial E_x / \partial t$, $j_y = 14 R E_0^2 \partial E_y / \partial t$. Obviously, the laser radiation linearly polarized along the x and y axes has different refractive indices

$$n_\parallel = 1 + 8\pi R E_0^2, \quad n_\perp = 1 + 28\pi R E_0^2. \quad (3)$$

If the laser radiation is elliptically polarized (1), under the action of the field E_0 its axes will be turned through the angle

$$\varphi = \frac{1}{2} \arctan\left[\frac{2\delta}{\delta^2 - 1} \sin\left(\frac{\alpha}{9} \frac{E_0^2}{E_{cr}^2} \frac{z}{\lambda} \right) \right]. \quad (4)$$

Here z is the size of the field interaction zone, $\delta = E_2 / E_1$ is the ratio of the major axes of the ellipse, and $\lambda = 2\pi c / \omega$ is the wavelength of the laser radiation. Clearly, by measuring the refractive indices (3) or the angle of rotation (4), we can uniquely determine the strength of the static electric field E_0. Note that these results are also valid for a variable field $E_0(t)$ if its characteristic fluctuation time is shorter than the interaction time of the fields $\tau = z / c$.

Let us assume that an electric field having the strength $E_0 = 1.3 \times 10^{15}$ V/cm (or $E_0 = 0.1 E_{cr}$) is localized in a region whose size is of the order a. Let us also suppose that the wavelength of the laser radiation is $\lambda = a / 10$ and the ratio of the major axes of its polarization ellipse is $\delta = 1.1$. In this case, the angle of rotation of the plane of the ellipse (4) is $\varphi = 4.2 \times 10^{-4}$ rad. Note that the angle of rotation φ decreases rapidly with decreasing field strength E_0. If $E_0 = 1.3 \times 10^{14}$ V/cm (or $E_0 = 0.01 E_{cr}$), we obtain $\varphi = 4.2 \times 10^{-6}$ rad.

[1] V. M. Harutunian and S. G. Oganesyan, Phys. Rep. **270**, 217 (1976).
[2] V. B. Berestetskiĭ, E. M. Lifshitz, and L. P. Pitaevskiĭ, *Relativistic Quantum Theory* (Pergamon Press, Oxford, 1971) [Russ. original, Part 2, Nauka, Moscow, 1971, 287 pp].
[3] A. A. Grib, S. G. Mamaev, and V. M. Mostepanenko, *Vacuum Quantum Effects in Strong Fields* [in Russian], Moscow, (1988), 290 pp.

Translated by R. M. Durham

Electron energy balance in an ionization-unstable plasma in a magnetogasdynamic channel

R. V. Vasil'eva, E. A. D'yakonova, A. V. Erofeev, and T. A. Lapushkina

A. F. Ioffe Physicotechnical Institute, Russian Academy of Sciences, St. Petersburg
(Submitted January 20, 1998)
Pis'ma Zh. Tekh. Fiz. **24**, 48–53 (July 26, 1998)

An experimental investigation was made of the evolution of ionization instability in a model of a disk-shaped Faraday magnetogasdynamic channel connected to a shock tube in a pure rare gas (xenon) with an alkaline additive. The main components of the average electron energy balance were determined: the Joule heating power, the average rate of energy transport of the heavy component by elastic collisions, and the average rate of energy lost through ionization. It was found that the electron energy defect which includes losses not taken into account, increases abruptly at supercritical values of the magnetic induction and accounts for approximately half of the Joule heating power. It is concluded that some of the electron energy is transferred to pulsations. © *1998 American Institute of Physics.* [S1063-7850(98)02807-9]

One of the fundamental problems of ionization-unstable magnetogasdynamic (MGD) fluxes is the electron energy balance, which has mainly been studied using a rare gas with an easily ionized alkali metal additive as the working medium. Under the conditions of MGD channels, the degree of ionization of the additives is in equilibrium with the electron temperature and the selective heating of the electrons is determined by the fact that the Joule heating power is equal to the average rate of energy transport of the heavy component in elastic collisions.[1] In this model, all the characteristics associated with the formation of plasma inhomogeneities are reduced to the fact that the effective plasma conductivity σ_{eff}, which determines the Joule heating, is less than the average value $\langle\sigma\rangle$. Using the relation $\sigma_{\text{eff}}=\langle\sigma\rangle\beta_{\text{eff}}(\omega/\langle\nu\rangle)^{-1}$ (Ref. 1) to determine the degree of separation of the temperature of the light and heavy plasma components, we propose a formula similar to the Kerrebrok formula:

$$\left\langle\left(\frac{T_e}{T}-1\right)\right\rangle = \frac{\gamma M^2}{3\delta}\beta_{\text{eff}}\langle\beta\rangle(1-K_y)^2, \tag{1}$$

where $\gamma=c_p/c_v$, M is the Mach number of the flow, $\beta_{\text{eff}},\langle\beta\rangle$ are the effective and the average Hall parameters, $\delta=1$ is the inelastic loss factor, and K_y is the load factor. However, an analysis made in Ref. 1 shows that this formula is not valid in all experiments. Some of the Joule energy may well be converted to pulsations, and here we propose to determine this fraction of the energy.

For this study a pure rare gas without alkali additives is used as the active medium under conditions when the ionization in the MGD channel is nonequilibrium. Thus, the inelastic energy losses to ionization of the gas must be taken into account in the electron energy balance. However, the problem still remains: does the Joule heating reduce to the average energy dissipated in the elastic and inelastic losses.

The experiment was carried out using a disk-shaped Faraday MGD channel connected to a shock tube with $K_y\rightarrow0$, $K_y\approx0.1$. The apparatus and the measurement method were described in Refs. 2–5. The duration of the flow was 400 μs. The experiments were carried out using xenon, the Mach number of the shock wave front in the shock tube was 6.9, and the initial pressure was 26 Torr with weak MGD interaction. The Mach number of the flow in the disk channel was 2–3, the Hall parameter was 1–3, and the degree of ionization of the gas $10^{-4}-10^{-3}$. Measurements were made of the effective plasma conductivity, the local values of the conductivity, the Hall parameter, and the electron densities and temperatures at various radii. Measurements were also made of the flow velocity and gas pressure. The atomic densities and temperatures were reconstructed by comparing the experimental and calculated data.

The electron energy balance is compiled for a volume of gas some distance from the entrance to the channel so that it is in a region of weakly varying gasdynamic parameters. It is assumed that the evolving plasma inhomogeneities do not perturb the gasdynamic flow. The experiments showed that the average Hall current and the average perturbation of the azimuthal field are zero. The estimates also showed that the energy losses caused by the emission and excitation of atoms and also associated with the variation of the average electron temperature are low compared with the energy dissipated in ionization. Under these assumptions, the electron energy balance has the following form:

$$\sigma_{\text{eff}}(uB)^2(1-K_y)^2 = \frac{3m_e}{m_a}k\langle n_e\rangle\langle\nu\rangle(\langle T_e\rangle-T)$$
$$+ \left(E_i+\frac{5}{2}k\langle T_e\rangle\right)\frac{\langle\Delta n\rangle}{\Delta t}+\Delta W, \tag{2}$$

where E_i is the ionization potential. The ionization rate is determined from the increment of the electron density at two radii $r_1=7$ cm, $r_2=10$ cm, $\Delta t=(r_2-r_1)/u$, $\langle\Delta n\rangle=\langle n_{e_2}\rangle-\langle n_{e_1}\rangle+\langle n_{e_1}\rangle(n_{a_2}-n_{a_1})/n_{a_1}$. In the section r_2-r_1 the plasma flow parameters vary negligibly, and thus the average

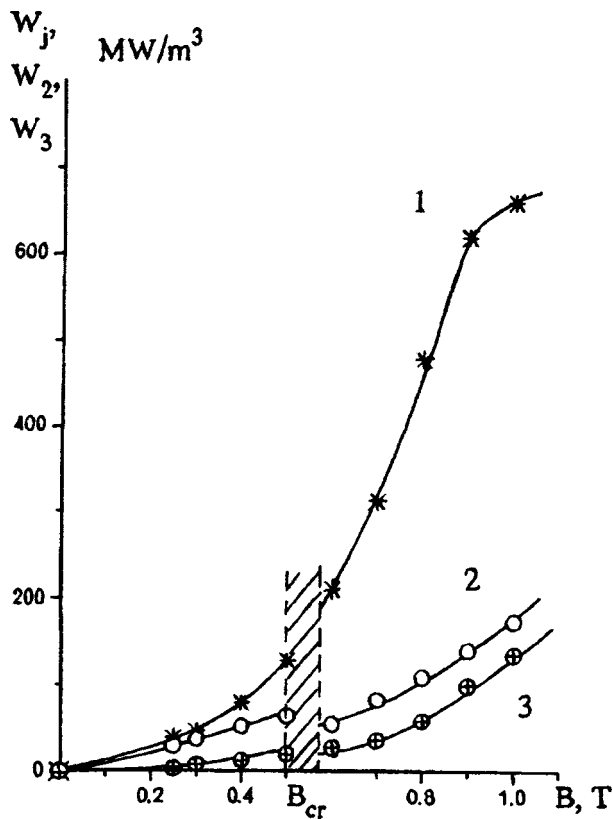FIG. 1. Joule heating power W_j (*1*), elastic energy losses W_2 (*2*), and energy dissipated in ionization W_3 (*3*) for various magnetic inductions; B_{cr} is the critical magnetic field.
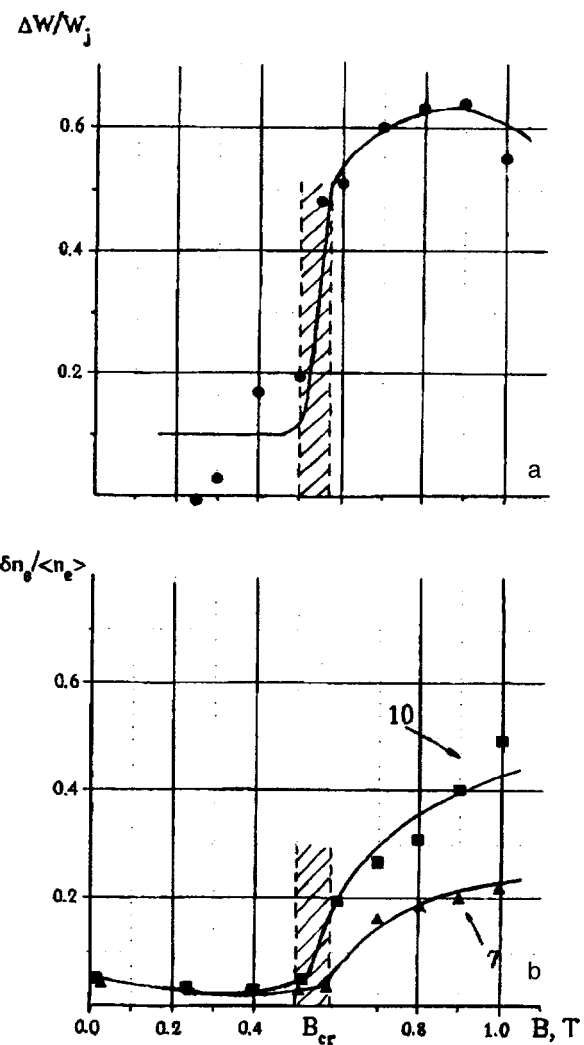

FIG. 2. a—Relative electron energy defect for various magnetic fields; b—fluctuations of the electron density at two radii for various magnetic inductions. The numbers on the curves are the values of r in centimeters.

values of the plasma parameters for this section are used to determine the elastic losses. The values of σ_{eff} were also measured for this section. The average energy transport rate is defined as $\langle \nu \rangle = n_a \langle c_e \rangle \langle Q_a \rangle (1 + \langle n_e \rangle / n_a \langle Q_i \rangle / \langle Q_a \rangle)$, where $\langle Q_a \rangle$ and $\langle Q_i \rangle$ are the energy transport cross sections for the atoms and ions, which are determined for $\langle T_e \rangle$. The electron energy defect ΔW includes the additional electron losses neglected in the energy balance. Figure 1 gives the components of the energy balance for subcritical and supercritical values of the magnetic field. The Joule heating slows at maximum magnetic induction because the stream slows appreciably as a result of the action of the ponderomotive force. The elastic energy losses increase because the electron density is greater and because the energy transport rate increases with electron temperature. The inelastic energy losses increase since the ionization rate increases with increasing field.

Figure 2a gives the energy defect relative to the Joule heating power. The values of $\Delta W / W_j$ for subcritical magnetic fields are taken as a basis for comparison. The observed difference of $\Delta W / W_j$ from zero in this region is within experimental error. The relative error in the determination of $\Delta W / W_j$ when these values are compared for different magnetic inductions is less than 20%. The slight decrease observed at $B = 1$ T is evidently caused by a reduction in the Joule heating. The fluctuations of the electron density shown in Fig. 2b reveal correlations between the fluctuations and

the energy defect. The indicated range of critical magnetic field values can be explained by the fact that the occurrence of fluctuations in a fixed cross section depends on the magnetic induction and on the time taken for the evolution of ionization instability. Since a longer lifetime is required for the plasma volume to attain larger distances, the lower the value of the magnetic induction, the larger the radius before the onset of instability. As the instability while the plasma volume moves from r_1 to r_2, the fluctuations grow. It can be seen from Fig. 2 that an energy defect appears when the inhomogeneities form and increases as the fluctuations in the electron density increase.

Thus, in fully developed ionization instability, the electron energy defect caused by structuring of the plasma accounts for approximately half the Joule heating power. This indicates that not only does the growth of the instability produce characteristic features in the current flow but various paths of electron energy losses in pulsations probably also exist. However, a more comprehensive model of ionization turbulence is required to determine these losses.

[1] A. V. Nedospasov and V. D. Khait, *Principles of the Physics of Processes in Low-Temperature Plasma Devices* [in Russian], Énergoatomizdat, Moscow (1991), 224 pp.

[2] R. V. Vasil'eva, A. L. Genkin, V. L. Goryachev *et al.*, *Nonequilibrium Rare-Gas Plasma with Nonequilibrium Ionization and MGD Generators* [in Russian], A. F. Ioffe Physicotechnical Institute Press, St. Petersburg, 206 pp.

[3] A. V. Erofeev, R. V. Vasil'eva, A. D. Zuev, T. A. Lapushkina, E. A. D'yakonova, and A. A. Markhotok, in *Proceedings of the 12th International Conference on MGD Electrical Power Generation*, Yokohama, Japan, 1996, Vol. 1, pp. 74–82.

[4] T. A. Lapushkina, R. V. Vasil'eva, A. V. Erofeev, and A. D. Zuev, Zh. Tekh. Fiz. **67**(12), 12 (1997) [Tech. Phys. **42**, 1382 (1997)].

[5] T. A. Lapushkina, E. A. D'yakonova, and R. V. Vasil'eva, Pis'ma Zh. Tekh. Fiz. **24**(2), 58 (1998) [Tech. Phys. Lett. **24**, 66 (1998)].

Translated by R. M. Durham

Electron energy in exoelectronic emission from a ferroelectric

L. M. Rabkin and V. N. Ivanov

Rostov State University

An analysis is made of the change in the potential in the plane of a grid electrode on the surface of a ferroelectric caused by exoelectronic emission under the influence of a pulsed electric field. The potential is calculated by means of integral equations from electrostatics. An estimate is made of the possible initial energies of electrons leaving the surface of the ferroelectric. © *1998 American Institute of Physics.* [S1063-7850(98)02907-3]

Exoelectronic emission from the surface of ferroelectrics has recently been studied to gain a deeper understanding of the physical properties of these materials and also with a view to using these materials to develop highly efficient pulsed emitters for vacuum devices.[1,2] In this last case, the ferroelectric is exposed to a pulsed electric field. However, the mechanism responsible for the high initial energies of the emitted electrons (up to a few kilo-electronvolts) has not been discussed in the literature, even though the spread of the initial velocities is the limiting factor in the application of these emitters. Here we examine a model to estimate the order-of-magnitude energy of the emitted electrons.

In the steady state, surface polarizing charges are screened by free charges distributed along the surface of the ferroelectric. When a fairly strong polarization-reversing electric field is abruptly applied, the polarizing charges vary rapidly, whereas the free charges do not vary significantly during polarization reversal since the emitted charge accounts for a small fraction of the polarizing charge and the conductivity of the ferroelectric is low. A change in the total surface charge alters its potential, which determines the energy of the emitted electrons.

In the usual experimental setup to observe exoelectronic emission, a grounded conducting film electrode in the form of a grid is deposited on the emitting surface of a ferroelectric wafer and an external electric field which reverses the polarization of the ferroelectric is generated by applying a pulsed voltage to a solid conducting electrode on the other surface of the wafer. We shall assume that the wafer is an order of magnitude thicker than the width of the slits in the conducting grid and that in calculations of the potential distribution in the plane of the grid, created by the charges distributed in this plane, the influence of the solid electrode can be neglected. Since the purpose of these calculations is to estimate the order-of-magnitude potential at the slit, for simplicity we shall consider a single slit between two conducting half-planes located on the surface of a semi-infinite ferroelectric.

The problem of the potential distribution created by uncompensated surface charges formed at the slit after polarization reversal of the ferroelectric induced by an external electric field is difficult to solve in a general formulation because of the nonlinear dielectric properties of the ferro-

electric. We shall confine our analysis to the limiting case of an external electric field so strong that the spontaneous polarization is completely oriented in the direction of the electric field and the dielectric properties of the ferroelectric are determined by two polarization mechanisms, which we shall assume to be linear. Disregarding the existing anisotropy (the difference between the permittivity measured parallel to the direction of spontaneous polarization and that measured in the perpendicular direction) we describe the dielectric by the scalar relative permittivity ε.

We position the origin of the Cartesian coordinate system at the center of a slit of width $2a$, with the z axis parallel to the slit, the x axis perpendicular to the slit parallel to the conducting half-planes, and the y axis running from the ferroelectric into vacuum. The problem involves determining the potential within the slit $\phi(x)$ ($|x| \leq a$, $y=0$) assuming that the charge density distribution $\sigma(x)$ ($|x|<a$) within the slit is known and that the electrode potential is zero, i.e., $\phi(x)=0$ ($|x|>a$). Since in this problem charges are only present at the planar interface of the two dielectrics, the potential and the electric field may be sought in a homogeneous medium with the equivalent relative permittivity $\varepsilon_e=(\varepsilon+1)/2 \cong \varepsilon/2$. It is convenient to introduce the electric field component in the slit plane $E=E_y(x)$ as the unknown, for which electrostatics methods using Fourier transformation[3] yield the singular integral equation

$$\pi^{-1}\int_{-a}^{+a} E(x_1)(x_1-x)^{-1}dx_1 = \sigma(x)/(2\varepsilon_e\varepsilon_0), \qquad (1)$$

where $\varepsilon_0=8.85\times10^{-1}$ F/m is the permittivity of free space.

Assuming that the function $\sigma(x)$ is even and $E(x)$ is odd, the solution of Eq. (1) is written as follows:[4]

$$E(x)=-(2\pi\varepsilon_e\varepsilon_0(a^2-x^2)^{1/2})^{-1}\int_{-a}^{+a}(a^2-x_1^2)^{1/2}\sigma(x_1)$$
$$\times(x_1-x)^{-1}dx_1. \qquad (2)$$

In relations (1) and (2) the integrals are understood in the sense of the principal value. The value of the integral is obtained by integrating $E(x)$:

$$\phi(x)=(2\pi\varepsilon_e\varepsilon_0).$$

$$\int_{-a}^{+a} \sigma(x_1)\ln((a^2 - xx_1 + ((a^2 - x^2)(a^2 - x_1^2))^{1/2})/$$

$$(a|x - x_1|))dx_1. \tag{3}$$

In order to estimate the potential, we assume that the surface charge density $\sigma(x)$ is constant and we set this equal to the spontaneous polarization P_s. We then find

$$\phi(x) = P_s/(2\varepsilon_0\varepsilon_e)(a^2x^2)^{1/2}. \tag{4}$$

The maximum energy of the emitted electrons is obtained using the highest value of the potential ϕ_{max} attained at the center of the slit ($x = 0$)

$$\phi_{max} = P_s a/(2\varepsilon_e\varepsilon_0). \tag{5}$$

Taking the values for barium titanate ferroelectrics $P_s = 0.25$ C/m^2, $a = 10^{-4}$ m, and $\varepsilon = 1000$, we obtain $\phi_{max} = 2.8$ kV, which is of the same order of magnitude as the experimental results.[1]

The potential distribution within the slit can also be calculated in the other limiting case of a weak external field when the ferroelectric can be described in the linear approximation of the scalar permittivity, $\varepsilon \gg 1$. Taking the external field in the ferroelectric at some distance from the slit to be perpendicular to the surface of the ferroelectric and uniform with the strength E_0, and using the method which was applied to derive relations (1) and (2), we find

$$\phi(x) = 0.5E(\varepsilon - 1)/(\varepsilon + 1)(a^2 - x^2), \tag{6}$$

i.e., in this approximation regardless of the specific value of the relative permittivity of the ferroelectric, we obtain

$$\phi_{max} \cong E_0 a/2. \tag{7}$$

On the basis of equalities (5) and (7), which were obtained for the limiting cases of strong and weak polarization-reversing fields, we can predict in general that the maximum energy of the emitted electrons will increase with increasing slit width. Note that the assumption used in the model, that the external electric field at some distance from the slit is uniform with the constant strength E_0, presupposes that as the width of the slit increases, the thickness of the ferroelectric wafer and the amplitude of the polarization-reversing voltage pulse increase proportionately. We also postulate that the increase in this energy with increasing polarization-reversing field should be slower in strong fields.

To sum up, these calculations of the potential distribution at the surface of a ferroelectric in the plane of a grid electrode have yielded estimates of the possible initial energies of the electrons leaving the surface of the ferroelectric as a result of exoelectronic emission under the action of a pulsed electric field.

[1] H. Gundel, H. Rige, E. J. N. Wilson *et al.*, Ferroelectrics **100**, 1 (1989).
[2] J. Asano, T. Imai, M. Okuyama, and Y. Hamakawa, Jpn. J. Appl. Phys., Part 1 **31**, 3098 (1992).
[3] I. N. Sneddon, *Fourier Transforms* (McGraw-Hill, New York, 1951, reprinted Dover, New York, 1995; IL, Moscow 1995).
[4] F. G. Tricomi, *Integral Equations* (Interscience, New York, 1957; IL, Moscow, 1960).

Translated by R. M. Durham

Lasing in submonolayer InAs/AlGaAs structures without external optical confinement

B. V. Volovik, A. F. Tsatsul'nikov, N. N. Ledentsov, M. V. Maksimov, A. V. Sakharov,
A. Yu. Egorov, A. E. Zhukov, A. R. Kovsh, V. M. Ustinov, P. S. Kop'ev, Zh. I. Alferov,
I. E. Kozin, M. V. Belousov, and D. Bimberg

A. F. Ioffe Physicotechnical Institute, Russian Academy of Sciences, St. Petersburg;
Institute of Physics, St. Petersburg State University, Petrodvorets;
Insitut für Festkörperphysik, Technische Universität Berlin, Hardenbergstr. 36, D-10623 Berlin, Germany
(Submitted February 13, 1998)
Pis'ma Zh. Tekh. Fiz. **24**, 58–66 (July 26, 1998)

Structures having a set of planes with submonolayer InAs inclusions in an AlGaAs matrix were
fabricated and studied. Lasing was observed as a result of optical excitation. It is shown
that lasing takes place via the ground state of excitons localized at InAs islands and may be
achieved without external optical confinement of the active region by wide-gap layers
of lower refractive index. The low threshold excitation density shows that these structures may
be used to develop low-threshold injection lasers in the visible range, exciton waveguides,
and self-contained microcavities. © *1998 American Institute of Physics.*
[S1063-7850(98)03007-9]

INTRODUCTION

Studies of growth processes in an InAs–GaAs system have shown that the depositing submonolayer InAs coatings leads to the spontaneous formation of an array of islands around one monolayer high with a characteristic width of around 4 nm and small dispersion of the lateral dimensions.[1,2] It is deduced from Refs. 3–5 that submonolayer structures possess unique optical properties. An appreciable increase in the exciton binding energy was observed as a result of lateral quantization.[3] In addition, a high luminescence efficiency and high exciton oscillator strength were observed even for an InAs layer of ultrasmall average thickness.[4] Lifting of the momentum selection rules was also demonstrated.[5] Later it was shown that in II–VI structures with CdSe/ZnMgSSe submonolayers the localization of excitons at islands and lifting of the momentum selection rules allows lasing to be achieved via the exciton ground state in submonolayer superlattices.[6] Lasing was achieved in structures without optical confinement by wide-gap layers of lower refractive index as a result of modulation of the refractive index near the exciton resonance.[7]

So far, no similar effects have been reported in III–V systems where the low electron mass makes the exciton localization energy at submonolayer islands extremely low (less than 50 eV for InAs submonolayers in GaAs[4]). We proposed and fabricated structures with InAs submonolayer islands in an AlGaAs matrix in which lasing was achieved in structures without external optical confinement as a result of an increase in the exciton localization energy in the islands. Lasing is observed at low optical excitation densities which opens up extensive prospects for using this effect in visible lasers to improve the optical confinement, in exciton waveguides, and self-contained microcavities, i.e., vertically emitting lasers, where modulation of the refractive index near the exciton resonance region in the quantum dot allows self-contained tuning of the cavity mode and the gain profile.

EXPERIMENT

The structures were grown by molecular beam epitaxy on semi-insulating GaAs(100) substrates in a RIBER 32P system with a solid-state As source under standard conditions of As enrichment. The structure studied in detail here was fabricated by growing a 0.3 μm thick GaAs buffer layer on the substrate, followed by a 0.7 μm thick $Al_{0.32}Ga_{0.68}As$ layer, and a thin (10 nm) $Al_{0.4}Ga_{0.6}As$ carrier-confinement layer. Another $Al_{0.32}Ga_{0.68}As$ (20 nm) layer was then followed by growth of the active region which consisted of 20 ultrathin GaAs quantum wells 1 nm thick with 0.5 ML InAs deposited at the center of each. The wells were separated by $Al_{0.32}Ga_{0.68}As$ barriers 50 Å thick. A $Al_{0.32}Ga_{0.68}As$ layer 100 nm thick and a thin (10 nm) $Al_{0.4}Ga_{0.6}As$ were then grown. The growth temperature was 600 °C, but during growth of the active region the temperature was reduced to 485 °C to avoid segregation and re-evaporation of In atoms from the surface.

Luminescence was excited by an Ar^+ laser ($\lambda = 514.5$ nm, $P = 500$ W/cm^2), a pulsed nitrogen laser ($\lambda = 337$ nm, pulse power 1 MW/cm^2), and a halogen lamp whose light was passed through a monochromator. The luminescence signal was recorded using a cooled photomultiplier.

RESULTS AND DISCUSSION

Figure 1 shows spectra of the photoluminescence, luminescence excitation, and optical reflection from this sample. It can be seen that at low levels of excitation with a photon energy higher than the $Al_{0.32}Ga_{0.68}As$ band gap, the spectrum contains a single peak which is attributed to radiative recombination of excitons localized at InAs islands. Note that this peak is shifted appreciably in the long-wavelength direction relative to the energy of the optical transition predicted for a GaAs quantum well 1 nm thick. This indicates that the exci-
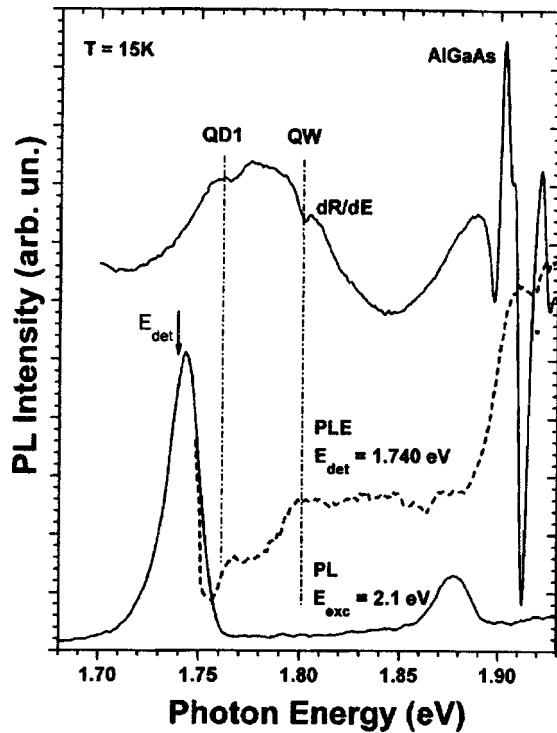
FIG. 1. Photoluminescence, luminescence excitation, and optical reflection spectra of this structure.
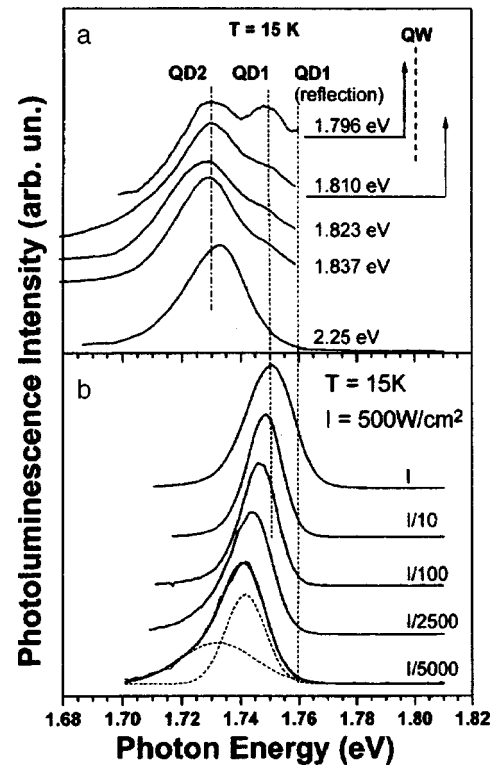

FIG. 2. a—Photoluminescence spectra for various excitation energies, indicated near the spectra. The position of the lines QD1 (reflection) and QW is taken from the optical reflection spectrum; b—photoluminescence spectra for various excitation densities. The luminescence was excited by an Ar⁺ laser. The dashed lines give the representation the spectrum as two Gaussian curves.

tons are strongly localized at InAs islands. The photoluminescence excitation spectrum has two characteristic features denoted as QD1 and QW. Note that these lines exactly match the exciton characteristics observed in the reflection spectrum, although that associated with QW is substantially less broadened. The position of the QD1 and QW characteristics in the luminescence excitation spectrum remains constant as the detection energy varies. We attribute these characteristics to states caused by excitons localized at InAs islands and exciton states in the ultranarrow GaAs quantum well (QW). This interpretation is quite consistent with the spectral position of the peaks and their half-width. The photoluminescence spectrum obtained for resonant excitation with a photon energy below the quantum-well band gap reveals two lines, one (QD2, 1.729 eV) shifted substantially in the long-wavelength direction compared with QD1 and another peak at 1.750 eV, close in energy to QD1 (Fig. 2a). Under low-density nonresonant excitation, the QD1 line is less efficiently excited, evidently because carriers with a high momentum in the plane of the GaAs quantum well are more efficiently trapped at islands with a high localization energy (QD2). However, at high excitation densities the QD1 line always predominates in the spectrum (Fig. 2b). Similar effects were also noted in submonolayer CdSe/ZnSe structures.[8]

As the excitation density is increased further, the line is shifted to a position close to QD1 in the reflection spectrum (Fig. 2b). In this case, the QD1 peak continues to dominate in the photoluminescence spectrum and the QD1 states do not saturate which evidences their high density. At high excitation densities a stimulated emission line is observed from the end of the cavity.

A cavity of length $L = 1$ mm was cut to investigate lasing. Figure 3a gives the integrated luminescence intensity as a function of the excitation density. It can be seen that at 800 W/cm², the intensity increases sharply, evidently because of the onset of stimulated emission at a photon energy of 1.750 eV (Fig. 3b). Note that for injection pumping, the threshold density of 800 W/cm² corresponds to a threshold current of ~200 A/cm², which is the upper limit for the threshold current because of the unknown fraction of carriers lost from the surface as a result of the surface nature of the nitrogen laser excitation. Thus, structures with InAs/AlGaAs submonolayers can be used to develop low-threshold injection lasers in the visible range even without external optical confinement (the average difference in the Al composition between the submonolayer superlattice and the confining layers is only 5%). The structure is shown schematically in the inset to Fig. 3c.

Figure 3c gives the temperature dependence of the threshold excitation density. It can be seen that from ~70 K the threshold density increases exponentially and by approximating the dependence using the formula $P = P_0 \times \exp(T/T_0)$ we can determine $T_0 = 30$ K. This behavior of the threshold density can be attributed to the thermal emission of carriers from islands. We observed lasing up to 170 K. The thermal stability of the emission may be improved by increasing the localization energy which can be achieved by using wider-gap confining layers or by using vertically correlated island growth.[9]
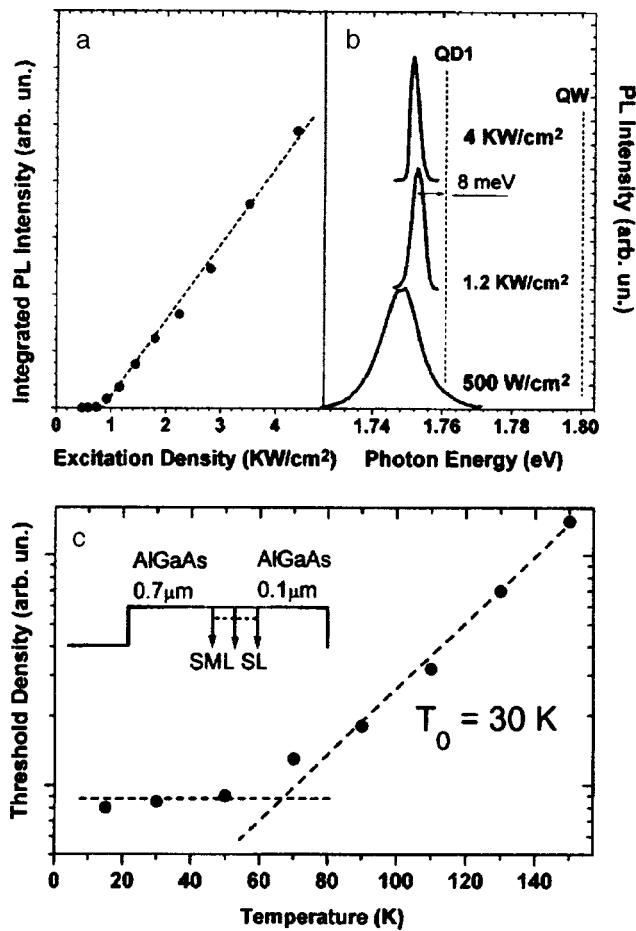
FIG. 3. a—Integrated photoluminescence intensity from end versus excitation density; b—photoluminescence spectra from end for various excitation densities shown on the spectra. The position of the QD1 and QW lines is taken from the optical reflection spectrum; c—temperature dependence of threshold excitation density. The value of T_0 was obtained using the approximation $P = P_0 \exp(T/T_0)$. The structure is shown in the inset.

CONCLUSIONS

We have demonstrated lasing in optically pumped structures formed by submonolayer InAs inclusions in an AlGaAs matrix without external optical confinement. The lasing occurs at low excitation densities, which makes these structures promising for the development of low-threshold injection lasers in the visible range, exciton waveguides, and self-contained microcavities.

[1] P. D. Wang, N. N. Ledentsov, C. M. Sotomayor Torres, P. S. Kop'ev, and V. M. Ustinov, Appl. Phys. Lett. **64**, 1526 (1994).

[2] V. Bressler-Hill, A. Lorke, S. Varma, P. M. Petroff, K. Pond, and W. H. Weinberg, Phys. Rev. B **50**, 8479 (1994).

[3] P. D. Wang, N. N. Ledentsov, C. M. Sotomayor Torres, I. N. Yassievich, A. Pakhomov, A. Yu. Egorov, P. S. Kop'ev, and V. M. Ustinov, Phys. Rev. B **50**, 1604 (1994).

[4] M. V. Belousov, N. N. Ledentsov, M. V. Maximov, P. D. Wang, I. N. Yassievich, N. N. Faleev, I. A. Kozin, V. M. Ustinov, P. S. Kop'ev, and C. M. Sotomayor Torres, Phys. Rev. B **51**, 14 (1995).

[5] A. A. Sirenko, T. Ruf, N. N. Ledentsov, A. Yu. Egorov, P. S. Kop'ev, V. M. Ustinov, and A. E. Zhukov, Solid State Commun. **97**, 169 (1996).

[6] N. N. Ledentsov, I. L. Krestnikov, M. V. Maximov, S. V. Ivanov, S. L. Sorokin, P. S. Kop'ev, Zh. I. Alferov, D. Bimberg, N. N. Ledentsov, and C. M. Sotomayor Torres, Appl. Phys. Lett. **69**, 1343 (1996); *ibid.*, **70**, 2677 (1997).

[7] I. L. Krestnikov, S. V. Ivanov, P. S. Kop'ev, N. N. Ledentsov, M. V. Maximov, A. V. Sakharov, S. V. Sorokin, A. Rosenauer, D. Gerthsen, C. M. Sotomayor Torres, D. Bimberg, and Zh. I. Alferov, Mater. Sci. Eng. B (in press).

[8] I. L. Krestnikov, M. V. Maksimov, S. V. Ivanov, N. N. Ledentsov, S. V. Sorokin, A. F. Tsatsul'nikov, O. G. Lyublinskaya, B. V. Volovik, P. S. Kop'ev, and C. M. Sotomayor Torres, Fiz. Tekh. Poluprovodn. **31**, 230 (1997) [Semiconductors **31**, 127 (1997)].

[9] I. L. Krestnikov, M. V. Maximov, A. V. Sakharov, P. S. Kop'ev, Zh. I. Alferov, N. N. Ledentsov, D. Bimberg, and C. M. Sotomayor Torres, in *Proceedings of the Eighth International Conference on II–VI Compounds,* Grenoble, France (J. Cryst. Growth, *in press*).

Translated by R. M. Durham

Thermionic valve effect and cathode crater rhythm in a low-voltage cold-cathode vacuum arc

M. K. Marakhtanov and A. M. Marakhtanov

N. E. Bauman State Technical University, Moscow
(Submitted November 6, 1997)
Pis'ma Zh. Tekh. Fiz. **24**, 67–72 (July 26, 1998)

A vacuum arc with a cold cathode burns rhythmically. The period of the rhythm is determined
by a thermionic valve effect which occurs between the hot crater and the cold cathode as
a result of the brief retention of the heat in the crater by the oppositely propagating electron flux.
© *1998 American Institute of Physics.* [S1063-7850(98)03107-3]

The experiments were carried out using the Bulat-6 vacuum-arc evaporation system and were described in Ref. 1.

The rhythmic nature of cathode craters can be seen from a photograph of the cathode where the motion of the cathode spot is imaged as a chain of light (Fig. 1a). The number of links in the chain is proportional to the exposure time. Each link consists of a cathode spot D_s from luminescence around a crater D, and a switching path of length L and width δ (Figs. 1b and 2a). The path probably consists of spots of smaller diameter δ burning around small cathode craters.[1] Since the links of the chain possess approximately the same brightness, we can assume that the average period of the rhythm $t_1 = \tau/N$ is also the same for all the links, where τ is the frame exposure time and N is the number of links in a particular frame. The average period $t_1 = 6 \times 10^{-4}$ s was determined from 16 photographs of a Ti cathode in an arc of

voltage $V = 24$ V and current $I = 67-72$ A, using black and white film (200 ASA), an exposure time of $1/30 - 1/500$ s, and a Zenit camera without any light filter.

The rhythm can be identified on the oscilloscope traces in Figs. 1c and 1d. It has been established[2] that any appearance of a cathode spot at a new site is preceded by its disappearance at an old site. The arc current should change abruptly between these events, inducing voltage surges in the Rogowski loop. The time between the voltage minima on the oscilloscope traces of the loop can then be taken to be equal to the period of the cathode spot rhythm. The average period is $t_2 = 1.4 \times 10^{-4}$ s for a Ti cathode at $I = 92$ A (Fig. 1c) and $t_2 = 2.9 \times 10^{-3}$ s for an Al cathode at $I = 73$ A (Fig. 1d). The Rogowski loop was mounted on an 8 mm diameter conductor near the cathode. The coil consisted of 270 turns on a ferrite ring of 16 mm diameter and 3×4 mm cross section.
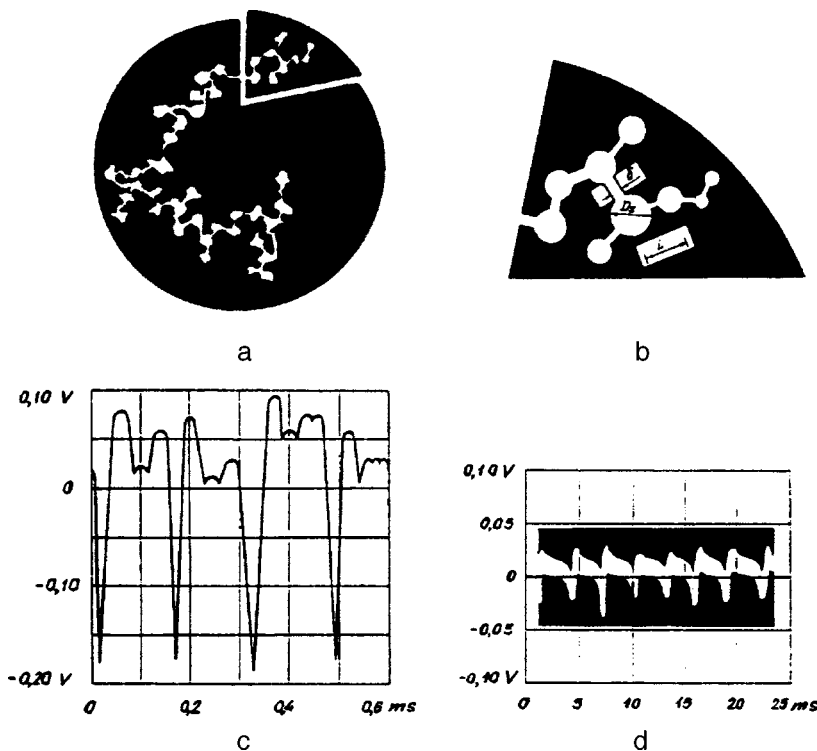

FIG. 1. Experimental illustration of a cathode crater rhythm: a—light chain of 42 cathode spots on the surface of a Ti cathode of diameter 56 mm, $\tau = 1/60$ s, $I = 69$ A, $V = 24$ V; b—diagram showing a link in the chain consisting of a cathode spot D_s and a switching path L, with the average value $D_s = 2.82$ mm; c—oscilloscope trace of output voltage of Rogowski loop in arc with Ti cathode, $I = 92$ A; d—the same in an arc with an Al cathode, $I = 73$ A.
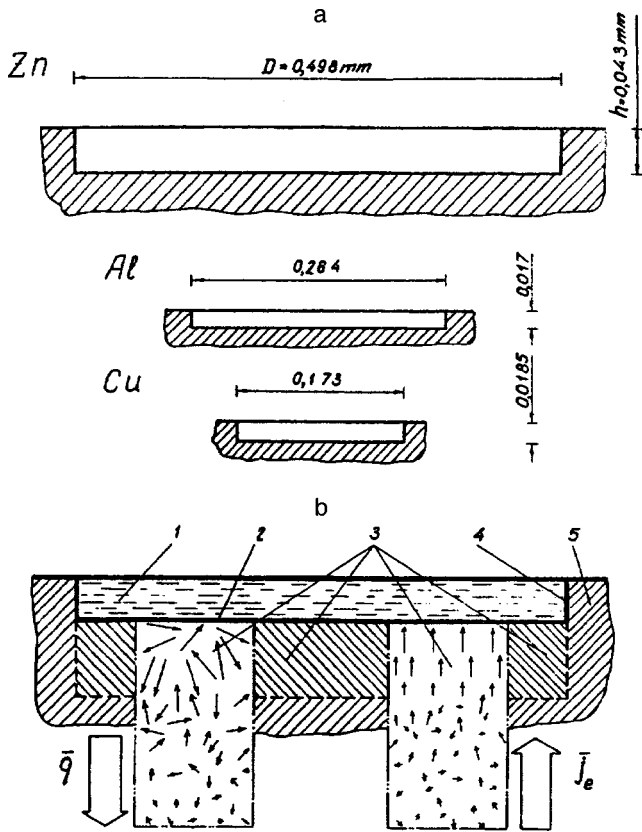
FIG. 2. Schematic of thermionic valve in cold cathode: a—average diameter D and depth h of cathode crater in highly conducting metals, current and arc voltage: Zn 48 A×16.7 V, Al 52 A×36 V, Cu 105 A×24.5 V; b—components of valve: *1*—molten metal, *2*—bottom of crater, *3*—valve layer of heated but solid metal, *4*—side surface of crater, *5*—cold cathode metal; the flux $\bar{q}$ of hot electrons (shown by the long arrows) transfers the kinetic energy of the electrons from the crater *1* to the cold cathode *5*; the opposite electron flux $\bar{J}_e$ transfers electrical energy from the arc power supply to the crater; the thermal energy is partially "blocked" in the crater as a result of the high flux density $\bar{J}_e$.

The output impedance of the loop was 75 kΩ.

The cathode crater rhythm can be determined from the known dimensions D and h (Fig. 2a and Ref. 1) and also from the rate of cathode sputtering S which is 15.20×10^{-6}, 4.05×10^{-6}, 11.76×10^{-6}, 11.57×10^{-6}, 4.42×10^{-6}, and 2.27×10^{-6} kg/s for Zn, Al, Cu, Fe, Ti, and Cr cathodes, respectively. The density ρ of these metals is 7150, 2700, 8930, 7880, 4540, and 7150 kg/m^3, respectively, and the average crater mass is $M = \rho D^2 h = 7.62 \times 10^{-8}$, 0.32×10^{-8}, 0.49×10^{-8}, 0.11×10^{-8}, and 0.032×10^{-8} kg, respectively. The average period of the crater rhythm is then $t_3 = M/S = 50.1 \times 10^{-4}$, 7.9×10^{-4}, 4.2×10^{-4}, 3.5×10^{-4}, 2.5×10^{-4}, and 1.1×10^{-4} s for the appropriate metal. Here it is assumed that S is constant and the switching time of the spot can be neglected.

Thus, for titanium we have $t_1 = 6 \times 10^{-4}$ s, $t_2 = 1.4 \times 10^{-4}$ s, and $t_3 = 2.5 \times 10^{-4}$ s. The similarity between the values of t indicates that the process of crater nucleation and disappearance on the cathode is regular. We shall determine the reason for this regularity.

The crater has a high temperature (but probably below the boiling point T_b of the metal) and also has a planar pro-file and short lifetime (Fig. 2a and Ref. 1). It is located on a cold conductor from which an unusually dense electron current flows into the crater. A thermal barrier is created between the crater and the cathode as a result of this current. Heat is transferred in the metal by the electronic and lattice conduction.[3,4] For Zn, Al, and Cu (for which the electrical conductivity is $\sigma > 0.25\sigma_{Cu}$) electronic heat transfer predominates and their real thermal conductivity is higher than σ (Ref. 4). In metals with low σ (Fe, Ti, and Cr) both mechanisms are involved in heat transfer and the real thermal conductivity increases with the ratio λ/σ (Ref. 4). Almost all the heat $\bar{q}$ leaves the crater through the bottom *2*, since its area is much greater than that of the side surface *4* (Fig. 2b).

The density of the electron flux to the crater is $j_e \simeq I/D^2$ because of its planar profile (Fig. 2a and Ref. 1). The flux $\bar{J}_e$ moves "forcibly" under the action of the power supply source and transfers the heat flux $\bar{q}$ back into the crater (Fig. 2b), producing a thermionic valve effect. The effect takes place over the period t when the crater area increases to the maximum D^2, i.e., as long as the electron drift velocity exceeds the critical value $V_e \geq V_{ec} = J_e/(en_e)$ $= 0.009, 0.026, 0.259, 0.133, 0.092$, and 0.307 m/s, respectively. Here we find $j_e = j$ (see Ref. 1), and the free electron concentration in the appropriate metal is $n_e = 13.10 \times 10^{28}$, 18.06×10^{28}, 8.45×10^{28}, 17.0×10^{28}, 22.64×10^{28}, and 24.99×10^{28} m^{-3} (Ref. 3). The valve retains in the crater exactly that amount of energy ε required for the arc to burn for the time t. After depletion of the crater mass, switching of the cathode spot within the hot circle R is initiated (see Ref. 1).

The valve is not ideal and a fraction of the arc power $f = Q_w/IV$ escapes to the cathode, where Q_w is the heat transferred by the cooling water. This fraction is $f = 0.033$, 0.182, 0.266, 0.412, 0.283, and 0.271 for Zn, Al, Cu, Fe, Ti, and Cr cathodes, respectively.

Changes in D, t, and R are caused by the thermal conductivity λ and T_b (see Ref. 1). With decreasing λ or T_b, less heat escapes to the cathode and $f_{Zn} < f_{Al} < f_{Cu}$. As q decreases, the heat density j_e which can be retained in the crater decreases and the diameter D is larger for low-melting metals $D_{Zn} > D_{Al} > D_{Cu}$. Growth of the crater to large D requires a long time (recall that $t_{2Al} > t_{2Ti}$, and also the series for t_3). Over the time t a large area R^2 is heated around the crater and a new crater appears at a larger distance R, being located on the cold metal where σ has a maximum (see Fig. 2 in Ref. 1). For Fe, Ti, and Cr these changes depend on λ/σ.

The existence of a thermionic valve is limited by the time t during which the crater mass $M = \rho V$ can accumulate thermal energy ε which is transferred by the current j to the crater volume V together with the electrical power Q. The condition for the existence of a crater $Q \geq \varepsilon/t$ is then rewritten as $j_e EV \geq \rho VC(1-f)/t$. We take $E = j_e/\sigma$, $\rho = nAm_p$, $j_e = en_e v_{ec}$; for a Ti cathode we have $C = C_1(T_f - T_c) + C_f + C_2(T_b - T_f)$, where $C_1 = 515$ J kg^{-1} K^{-1} and $C_2 \simeq 700$ J kg^{-1} K^{-1} are the specific heats of the solid and liquid Ti, $C_f = 314\,000$ J/kg is the specific heat of fusion of Ti, $T_c = 300$ K, $T_f = 1881$ K, and T

=3560 K are the temperature of the cold cathode, the melting point, and the boiling point of Ti, respectively, $\sigma \approx 3.05 \times 10^5 \ \Omega^{-1} \, m^{-1}$ at $T \approx T_f$, $A = 48$ u, $t = (t_1 + t_2 + t_3)/3 = (6 + 1.4 + 2.5) \times 10^{-4}/3 = 3.3 \times 10^{-4}$ s. We rewrite this last inequality and we estimate the value of j_e for a titanium cathode

$$j_e \geqslant \frac{m_p}{e} \frac{\sigma}{V_{ec}} \frac{A}{t} C(1 - f)$$

$$= 10^{-8} \frac{3.05 \times 10^5}{0.092} \frac{48}{3.3 \times 10^{-4}}$$

$$\times [515 \times (1881 - 300) + 314\,000$$

$$+ 700(3560 - 1881)](1 - 0.283)$$

$$= 7.96 \times 10^9 \ A/m^2.$$

The density j_e obtained as a result of this estimate is close to the experimental value $j = 3.33 \times 10^9 \ Am^{-2}$ for Ti (Ref. 1), which suggests that a thermionic valve does exist, determining the rhythm t in a low-voltage cold-cathode vacuum arc. The physical quantities used here were taken from Ref. 5.

[1] M. K. Marakhtanov and A. M. Marakhtanov, Pis'ma Zh. Tekh. Fiz. **24**(13), 14 (1998) [Tech. Phys. Lett. **24**, 504 (1998)].

[2] I. G. Kesaev, *Cathode Processes in an Electric Arc* [in Russian], Nauka, Moscow p. 6.

[3] C. Kittel, *Introduction to Solid State Physics*, 5th edition (Wiley, New York, 1976; Nauka, Moscow, 1978, 791 pp.).

[4] V. E. Mikryukov, *Thermal Conductivity and Electrical Conductivity of Metals and Alloys* [in Russian], Metallurgizdat, Moscow (1959), 260 pp.

[5] A. P. Babichev, N. A. Babushkina, A. M. Bratkovskiǐ *et al.*, in *Handbook of Physical Quantities*, edited by I. S. Grigor'ev and E. Z. Meǐlikhov [in Russian], Énergoatomizdat, Moscow (1991), 1232 pp.

Translated by R. M. Durham

Investigation of the influence of the thermal prehistory of zinc and cadmium melts on their crystallization

V. D. Aleksandrov and A. A. Barannikov

Donbass State Academy of Building and Architecture
(Submitted January 15, 1998)
Pis'ma Zh. Tekh. Fiz. **24**, 73–78 (July 26, 1998)

Methods of thermal analysis were used to study how the temperature and hold time of zinc and cadmium melts and their rate of cooling influence their crystallization. It was established that zinc and cadmium melts exhibit no precrystallization supercooling. It was confirmed that neither cooling at a rate between 0.001 and 8 K/s, nor heating Zn and Cd melts to temperatures 200 K above the appropriate melting point, nor isothermal ''annealing'' for up to 4 h, nor using a mass between 50 mg and 50 g resulted in supercooling during crystallization. The results are analyzed using a cluster model of the crystallization of Zn and Cd melts based on the similarity between the crystal-chemical parameters of the solid and liquid phases of these substances. © *1998 American Institute of Physics.*
[S1063-7850(98)03207-8]

Almost all simple substances show a tendency toward precrystallization supercooling[1–7] when their melts are cooled below the melting point T_L. However, no supercooling, ΔT^-, during crystallization of solid zinc and cadmium samples has been reported in the literature. Data presented in Ref. 8 on the supercooling of Cd particles of between 4 and 44 nm in aluminum alloys up to ~ 60 K have no relevance to solid materials, since particles of this size are a completely different substance and form the subject of special investigations in small-particle physics.[9]

The lack of publications on supercooling in solid Zn and Cd is fairly surprising, considering the ready availability of these elements, their relatively low melting points (692.75 K for Zn and 594.26 K for Cd) (Ref. 10), and their noncorrosive properties under normal conditions.

Here we describe the results of a study of the influence of the thermal prehistory of zinc and cadmium on their crystallization using methods of ballistic thermal analysis.[3–7]

The samples were high-purity zinc and cadmium weighing 50 mg, 0.1, 1.0, 2.0, 6.0, and 50 g with 5 or 6 test being made for each weight. The crucibles were made of alundum and quartz. The tests were carried out in air, in a rare-gas atmosphere (argon), in a vacuum of up to $\sim 10^{-5}$ Torr under conditions of dynamic pumping in a vacuum station, and in a ''static'' vacuum ($\sim 10^{-3}$ Torr) using a Stepanov ampoule. Different rates of cooling were used: 0.001, 0.02, 0.3, 1.0, and 8.0 K/s.

Thermal cycling was carried out in a specially prepared ''gradient-free'' resistance furnace over a temperature range covering the melting and crystallization range. A programmable controller allowed the thermal heating and cooling cycles to be carried out in a particular regime. The lower limit of the thermal cycles was kept constant (at 50 K below T_L) while the upper limit was varied at two degree intervals between T_L and superheating by 200 K above T_L. The temperature of the samples was mainly measured using a shielded XA thermocouple and was recorded on chart paper

using a KSP-4 potentiometer with a 1 mV scale. In some cases, unshielded XA thermocouples inserted directly in the sample were used.

Between 50 and 100 heating and cooling cycles were carried out on the same sample under the same experimental conditions (at the same rate of cooling, for the same mass, and so on).

The reliability of the results was confirmed by repeating a series of experiments many times for each sample. The error of the temperature measurements was 0.15–0.20 K/s.

It was established that under all these experimental conditions, for all Zn and Cd samples, no precrystallization supercooling was observed regardless of mass, rate of cooling, crucible material, atmosphere, temperature, and isothermal hold time. The crystallization process exhibited equilibrium behavior and took place at a crystallization temperature corresponding to the melting point of the material and the supercooling ($\Delta T^- = T_L - T$) was zero.

By way of examples, Figs. 1 and 2 show cooling thermograms for 1 g zinc and cadmium samples, respectively, at rates of 0.3 K/s in air. In both cases, the preheating of the melt was ~ 35 K above the melting point of the appropriate material. It can be seen that at temperatures T_L a crystallization plateau is observed without any initial supercooling.

Preliminary isothermal holding of the melt for between 1 min and 4 h at temperatures 10, 20, 50, and 100 K above the melting point did not cause any supercooling.

However, other substances (such as Bi, Sb, Sn, Se, Te, InSb, $PbCl_2$, H_2O, and In–Sb alloys) always exhibited precrystallization supercooling in our systems.[3–7] For comparison Fig. 3 shows crystallization isotherms for bismuth (1 g) recorded by us under similar crystallization conditions. It can be seen that bismuth exhibits the supercooling $\Delta T^- = 21.4$ K at a heating and cooling rate of ~ 0.25 K/s.

An analysis of the crystallographic table of chemical elements[11] shows that zinc and cadmium stand alone among the transition metals, and in fact among all the elements of
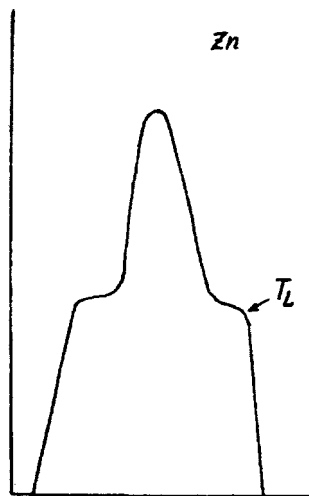
FIG. 1. Crystallization thermogram for zinc showing no precrystallization supercooling.

the Periodic Table. First, Zn and Cd are at the end of this series and have completely filled $3d$ and $4d$ electron shells. Second, they are isomorphous and the only hcp modification with an anomalously high lattice parameter ratio ($c/a = 1.8869$ for Zn and 1.8859 for Cd) melts with the conservation of short-range order. Zinc and cadmium possess the characteristics of covalent crystals which are formed by the sharing of six outer electrons with their six nearest neighbors in the layer. As a result of melting, the weaker bonds between the layers are broken and these become structural units of the liquid phase in the form of flexible cluster conformations. The strong covalent bonds between the atoms in these clusters are not broken at high temperatures, as is evidenced by x-ray structural analyses,[12] which indicate that when Zn and Cd melts are superheated to 100–120 K above T_L, the structure of the liquid phase becomes close-packed with the first coordination number ~ 11.0– 11.5 and does not undergo structural rearrangement.

Thus, the cluster structure of the liquid phase of Zn and Cd is similar to the structure of the solid phase, and during
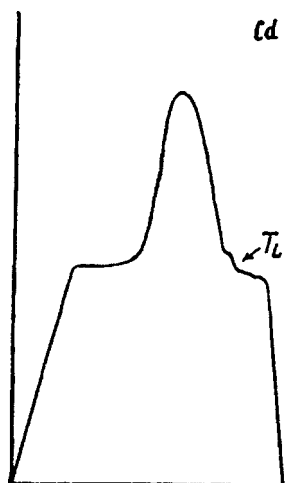

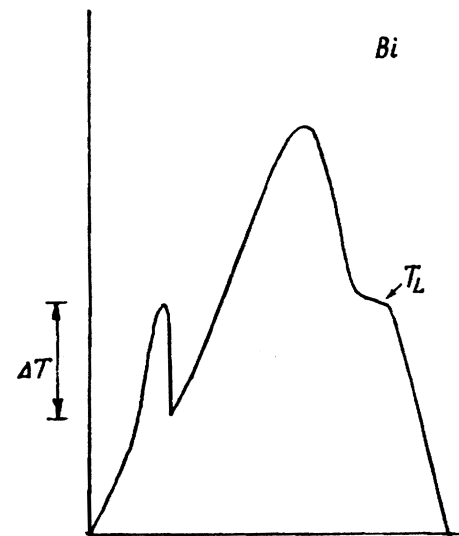FIG. 2. Crystallization thermogram for cadmium showing no precrystallization supercooling.

FIG. 3. Crystallization thermogram for bismuth showing precrystallization supercooling.

solidification the clusters readily combine to form a crystal so that crystallization takes place in equilibrium without supercooling. That is to say, the crystallization of Zn and Cd takes place, as it were, at its own ''seeds'' (clusters) without a specific incubation period. Substances which undergo structural rearrangement in the liquid state (such as Sb, Bi, Sn, H_2O, and so on) and possess configurations of atoms in clusters, unlike crystals,[12] exhibit hysteresis effects. Rearrangement of the atoms back into a crystal as a result of cooling below T_L requires an incubation period in a metastable supercooled region. This is why the crystallization of these substances involves supercooling.

To conclude, we postulate that the absence of supercooling for Zn and Cd was probably well known to researchers. The results were not published possibly for two reasons: it was either assumed that the absence of supercooling for these substances was not particularly noteworthy, i.e., a null result, or no explanation could be provided, particularly in terms of the classical theories of nucleation and crystallization.

[1] V. I. Danilov, *Liquid Metals and Their Solidification* [in Russian], State Scientific-Technical Publishers of Literature on Ferrous and Non-Ferrous Metallurgy, Moscow (1962), 434 pp.

[2] B. Chalmers, *Solidification Theory* [in Russian], Metallurgiya, Moscow (1968), 288 pp.

[3] V. I. Petrenko and V. D. Aleksandrov, Pis'ma Zh. Tekh. Fiz. **9**(22), 1354 (1983) [Tech. Phys. Lett. **9**, 582 (1983)].

[4] V. D. Aleksandrov and V. I. Petrenko, Rasplavy **2**(5), 29 (1988).

[5] V. D. Aleksandrov and V. I. Petrenko, Rasplavy No. 3, 83 (1992).

[6] V. D. Aleksandrov, Neorg. Mater. **28**, 709 (1992).

[7] V. D. Aleksandrov and V. I. Petrenko, Rasplavy No. 3, 85 (1993).

[8] B. A. Muller and J. H. Perepezko, Metall. Trans. A **18**, 1143 (1987).

[9] Yu. I. Petrov, *Physics of Small Particles* [in Russian], Nauka, Moscow (1982) 360 pp.

[10] *Properties of Elements, Handbook Edition*, edited by M. E. Drits [in Russian], Metallurgiya, Moscow (1985), 672 pp.

[11] V. D. Aleksandrov, Fiz. Met. Metalloved. **67**, 1219 (1989).

[12] B. I. Khrushchev, *Structure of Liquid Metals* [in Russian], FAN, Tashkent (1970), 112 pp.

Translated by R. M. Durham

Qualitative analysis of the behavior of a Lorenz dynamic system based on geometric concepts

V. V. Afanas'ev, Yu. E. Pol'skiĭ, and V. S. Chernyavskiĭ

A. N. Tupolev State Technical University, Kazan

The behavior of a Lorenz dynamic system is analyzed qualitatively using geometric concepts. This analytic approach can be applied to analyze a broad class of systems with dynamic chaos. © *1998 American Institute of Physics.* [S1063-7850(98)03307-2]

At present, the main method of studying complex nonlinear dynamic systems with strange attractors is mathematical computer modeling. It is interesting to search for methods which could yield qualitative conclusions as to the behavior of a dynamic system without knowing its solution and which could predict the time when the system becomes stochastic. One such method is the Mel'nikov method of separatrix splitting, but this can only be applied to a limited class of dynamic systems.[1] We propose an analytic approach which can be used to analyze the behavior of a wide range of systems with dynamic chaos.

Our proposed approach involves representing a system of n differential equations describing a nonlinear dynamic system in the form of a differential equation

$$\Phi_1'(x,a) = -\Phi_2(x,a), \tag{1}$$

where $x = (x_1, x_2, \ldots, x_n)$ is the vector of the phase variables of the system and $a = (a_1, a_2, \ldots, a_N)$ is the vector of the system parameters. The functions $\Phi_{1,2}$ determine the surfaces $\Phi_1 = A$ and $\Phi_2 = B$ in the phase space of the system. The sign of B can be used to determine how the mapping point of the dynamic system moves relative to the family of surfaces $\Phi_1 = \text{const}$ (in the direction corresponding to increasing or decreasing A). A set of different functions $\Phi_{1,2}$ can be obtained for the same dynamic system, which means that the motion of the trajectory in the phase space of the system as a whole can be assessed by means of a suitable choice of $\Phi_{1,2}$.

We shall illustrate the proposed approach to investigate a Lorenz system:

$$\dot{x} = -\sigma x + \sigma y; \quad \dot{y} = -y + rx - xz; \quad \dot{z} = -bz + xy, \tag{2}$$

where r, σ, and b are the parameters of the system. Equation (1) can be obtained for system (2) as the sum of a linear combination of equations (2) with a linear combination of Eqs. (2) multiplied by x, y, and z, respectively, as was done in Ref. 2, p. 92:

$$\{(k_1 x^2 + k_2 y^2 + k_3 z^2)/2 + k_4 x + k_5 y + k_6 z + k_7\}'$$
$$= -\{\sigma k_1 x^2 + k_2 y^2 + bk_3 z^2 - xyz(k_3 - k_2)$$
$$- xy(\sigma k_1 + rk_2 + k_6) + k_5 xz + x(\sigma k_4 - k_5 r)$$
$$+ y(k_5 - \sigma k_4) + k_6 bz\}, \tag{3}$$

where k_1, k_2, k_3, k_4, k_5, k_6, and k_7 are constant coefficients. Depending on whether the mapping point lies inside or outside the surface

$$\sigma k_1 x^2 + k_2 y^2 + bk_3 z^2 - xyz(k_3 - k_2) - xy(\sigma k_1 + rk_2 + k_6)$$
$$+ k_5 xz + x(\sigma k_4 - k_5 r) + y(k_5 - \sigma k_4) + k_6 bz = B$$

(where B is a certain constant determined by the instantaneous values of x, y, and z), the motion of the mapping point in the phase space relative to the family of surfaces

$$(k_1 x^2 + k_2 y^2 + k_3 z^2)/2 + k_4 x + k_5 y + k_6 z + k_7 = A = \text{const}$$

varies qualitatively, moving in the direction of increasing A ($B < 0$) or decreasing A ($B > 0$). The intersections of these surfaces with the plane perpendicular to the X axis, projected onto the YZ plane, have the form of quadratic curves. If we choose the coefficients to be $k_1 = 1/\sigma$, $k_2 = k_3 = 1/r$, $k_4 = k_5 = k_7 = 0$, and $k_6 = -2$, Eq. (1) for the Lorenz system (2) becomes simplified and has the form

$$(x^2/\sigma + y^2/r + (z-2r)^2/r)' = -2br(x^2/br + y^2/br^2$$
$$+ (z-r)^2/r^2 - 1). \tag{4}$$

Equation (4) is valid for the Lorenz system (2) and for other types of nonlinear dynamic systems which can be reduced to the form of Eq. (1) for the given choice of $\Phi_{1,2}$, but with a different set of coefficients $k_1, k_2, \ldots, k_7$.

It is known from the theory of differential equations that a relation of the type (4) determines the region of asymptotic motion of the phase trajectory of a dynamic system.[3] The function Φ_1 in Eq. (4) is the generalized distance ρ between the mapping point with the instantaneous coordinates (x, y, z) and the point with the coordinates $(0, 0, 2r)$. The function $\Phi_2 = 0$ in Eq. (4) is an ellipsoid. Inside the ellipsoid ($\Phi_2 < 0$) ρ increases while outside ($\Phi_2 > 0$) ρ decreases. This implies that for any initial conditions, the asymptotic motion of the phase trajectory, including that in the presence of strange attractors, will take place in a bounded region of phase space. We shall estimate the boundaries of this region. From Eq. (4) we obtain the maximum $\rho_{max} = b^2 r^2/(b-1)$. For $b > 1$ the region is an ellipsoid of the form

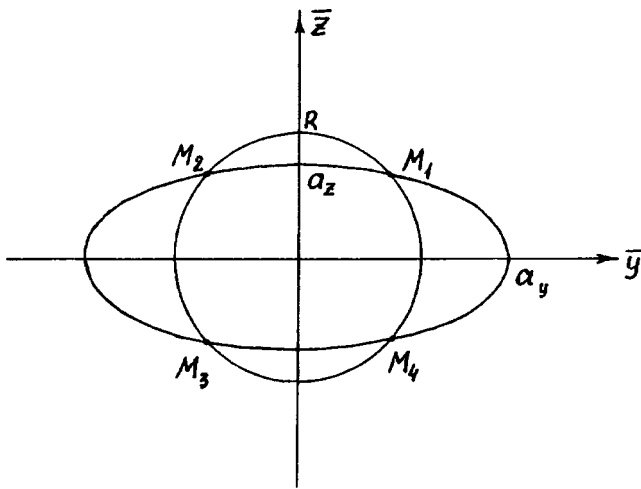$$x^2/(\sqrt{\rho_{max}}\,\sigma/r)^2 + y^2/(\sqrt{\rho_{max}})^2 + (z-2r)^2/(\sqrt{\rho_{max}})^2 = 1 \tag{5}$$

FIG. 1.

with its center at the point having the coordinates $(0,0,2r)$. It follows from Eq. (5) that if strange attractors appear in the Lorenz system, the values of the instantaneous phase coordinates lie within boundaries defined by the inequalities

$$-b\sqrt{\sigma r/(b-1)} \leqslant x \leqslant b\sqrt{\sigma r/(b-1)},$$

$$-br\sqrt{1/(b-1)} \leqslant y \leqslant br\sqrt{1/(b-1)},$$

$$2r - br\sqrt{1/(b-1)} \leqslant z \leqslant 2r + br\sqrt{1/(b-1)}. \tag{6}$$

If we choose the coefficients $k_1 = r/\sigma$, $k_2 = k_3 = -1$, $k_4 = k_5 = k_6 = k_7 = 0$, $\Phi_{1,2}$ has the following form:

$$\Phi_1(x,y,z) = x^2 r/\sigma - y^2 - z^2, \tag{7}$$

$$\Phi_2(x,y,z) = x^2 r - y^2 - bz^2. \tag{8}$$

A change in the sign of $\Phi_{1,2}$ determined by the instantaneous coordinates x,y,z changes the form of the $\Phi_{1,2}$ surfaces. For $\Phi_{1,2} > 0$ the surfaces are parted hyperboloids, for $\Phi_{1,2} = 0$ they are cones, and for $\Phi_{1,2} < 0$ they are unparted hyperboloids. For the instantaneous coordinates x,y,z the surfaces of constant $\Phi_1 = A$ and $\Phi_2 = B$ in the plane $x = \bar{x} = \text{const}$ correspond to the cross sections

$$(\bar{y}^2 + \bar{z}^2)/(\bar{x}^2 r/\sigma - A) = 1 \quad \text{—circle},$$

$$\bar{y}^2/(\bar{x}^2 r - B) + \bar{z}^2/(\bar{x}^2 r/b - B/b) = 1 \quad \text{—ellipse}.$$

When the instantaneous coordinates x,y,z vary, A and B vary as do the sizes of the circle and the ellipse, and their relative position. For $\bar{x} = x$ we obtain a circle of radius $R|_{\bar{x}=x} = \sqrt{y^2 + z^2}$ and an ellipse with the semiaxes $a_y|_{\bar{x}=x} = \sqrt{y^2 + bz^2}$ and $a_z|_{\bar{x}=x} = \sqrt{y^2/b + z^2}$ (see Fig. 1). The point M_i $(i = \overline{1,4})$ corresponds to the instantaneous value of the

phase coordinates x,y,z. Since the value of the phase coordinate z for a Lorenz system is positive because of the inequalities (6), the position of the mapping point of the system corresponds to the points M_1 and M_2. For $a_z = R$ ($y = 0$) the points M_1 and M_2 are the same. From the time ($y = 0$), the phase trajectory must undergo a transition from one state of unstable equilibrium to another over the time $\Delta t \leqslant T$ (where $T = 4\pi/\sqrt{8\sigma(r-1) - (\sigma+r)^2}$ is the oscillation period of the system which is determined in accordance with Ref. 4). Thus, the proposed approach allows us to determine analytically the onset of qualitative changes in the behavior of a dynamic system and specifically shows that as the system changes between unstable equilibrium states, the sign of the y coordinate changes first, followed by that of the x coordinate. This sequence of change in the signs of the x and y coordinates is confirmed by the experimental results.[2]

The possibility of determining the instant that qualitative changes take place in the behavior of the system, allows us to find the specific time intervals for efficient application of external controlling influences to the parameters of a Lorenz dynamic system[4] to ensure the desired behavior.

The representation (1) can also be used to analyze the behavior of other types of nonlinear dynamic systems with strange attractors (Rössler system, Ruelle–Takens system, and so on) although this is outside the scope of the present paper.

From this analysis, we can draw the following conclusions:

1. The differential representation (1) is an effective method of studying the behavior of dynamic systems with strange attractors.

2. An analysis of the functions $\Phi_{1,2}$ (4) allows us to determine the bounded volume of phase space in which the phase trajectory of a Lorenz dynamic system undergoes asymptotic motion.

3. An analysis of the intersections of the $\Phi_{1,2}$ surfaces (7) and (8) of the Lorenz system can provide an analytic substantiation of the condition ($y = 0$) for the onset of a transition between regions of unstable equilibrium states and allows us to determine the boundaries of the times intervals for these transitions in a dynamic system.

[1] V. V. Afanas'ev, Yu. E. Pol'skiĭ, and V. S. Chernyavskiĭ, Pis'ma Zh. Tekh. Fiz. **23**(23), 40 (1997) [Tech. Phys. Lett. **23**, 917 (1997)].

[2] *Strange Attractors*, edited by Ya. G. Sinai and L. P. Shil'nikov [in Russian], Mir, Moscow (1988).

[3] V. V. Nemytskii and V. V. Stepanov, *Qualitative Theory of Differential Equations* (Princeton University Press, Princeton, N.J., 1960) [Russ. original, Gostekhizdat, Moscow, 1947]

[4] V. V. Afanas'ev and Yu. E. Pol'skiĭ, Pis'ma Zh. Tekh. Fiz. **15**(18), 86 (1989) [Sov. Tech. Phys. Lett. **15**, 741 (1989)].

Translated by R. M. Durham

Electrodynamic acceleration of ultraheavy molecular ions

S. K. Sekatskiĭ

Institute of Spectroscopy, Russian Academy of Sciences, Troitsk, Moscow Province

The design of an ''electrodynamic accelerator'' for ultraheavy molecular ions with masses of order 10^6 Da is analyzed. It is shown that these ions can be efficiently accelerated to energies of hundreds of kilo-electronvolts over lengths no greater than 20 cm by using a sequence of voltage pulses with amplitudes of several kilovolts and microsecond durations. This acceleration allows ultraheavy molecular ions to be efficiently recorded using conventional secondary electron multipliers or multichannel plates. © *1998 American Institute of Physics.* [S1063-7850(98)03407-7]

Time-of-flight mass spectrometry is now being successfully used in biochemical and medical research as a highly sensitive, reliable, and relatively simple method of detecting biological molecules and their fragments. This particularly applies to mass-spectrometric time-of-flight methods using pulsed laser desorption/ionization of complex molecules in specially selected matrixes (described in the English literature as matrix-assisted laser desorption/ionization, or MALDI)[1] which can reliably detect relatively small fragments of protein molecules and oligonucleotides[2] as well as very heavy molecules with masses up to 150 000 Da (Ref. 3). It has been suggested that this method will be also be very useful for solving fundamental problems such as unraveling the nucleotide sequence of DNA (Ref. 4) which requires, as do many other applications, the reliable detection of molecules and their fragments with extremely high masses, up to 10^6 Da and higher.[5]

However, studies of such heavy molecules present appreciable difficulties, since the velocity they acquire at the potentials of a few or even tens of kilovolts used in typical time-of-flight mass spectrometers is inadequate for detection using conventional secondary electron multipliers and multichannel plates.[6] The efficiency of detection of high-mass ions increases as their energy increases (i.e., the accelerating potential of the mass spectrometer).[7,8] However, increasing this potential even to values of 30–50 kV, not to mention higher values, presents major problems for compact laboratory systems. It would seem that the types of detectors other than secondary electron multipliers or multichannel plates, now being actively discussed and investigated to solve this problem, such as cryogenic detectors operating at 0.4 K and calorimetric particle detectors (see Ref. 9 and the literature cited therein) cannot completely solve this problem because they are expensive and difficult to operate.

The present note is intended to draw attention to the fact that ions of such high mass can easily be accelerated ''electrodynamically'' by passing them through a set of accelerating gaps having typical lengths l of the order of a few millimeters to which are applied high-voltage pulses having amplitudes U of a few kilovolts and durations t between one and a few microseconds. This is attributable to the low velocity of such heavy ions; for example, the velocity of an ion of mass $M = 10^6$ Da, accelerated to 10 kV, is only 1.4×10^3 m/s, i.e., in 1 μs this ion only covers a distance of 1.4 mm. The system required to implement this principle of electrodynamic acceleration is very compact and inexpensive, allowing heavy ions to be accelerated to potentials of hundreds of kilovolts over a length of 10–20 cm.

The principle of electrodynamic acceleration is illustrated in Fig. 1, where the parameters are as follows: the first two accelerating gaps have length $l = 3$ mm, the next five $l = 5$ mm, the following eight $l = 7$ mm, and the next eight $l = 9$ mm. A sequence of rectangular pulses of amplitude $U = 10$ kV and duration $t = 1$ μs are applied to the even electrodes, as shown in Fig. 1 ($+U$ for time t, then 0 for time t, and $-U$ for time t, and so on). The odd electrodes are grounded. It is suggested that either diaphragms or grid electrodes highly permeable to ions may be used. The corresponding ion-optical effects of ion beam focusing and defocusing are not considered (these clearly cannot be of any significance because the ions pass through the grids at times when the electrode potentials are zero). The operation of the accelerating system is analyzed for a pulsed source of heavy ions similar to that described in Refs. 2 and 3.

During the voltage pulse the ion is uniformly accelerated from the initial velocity v_i to $v_{i+1} = v_i + eUt/lM$, covering a distance $s_i = v_i t + eUt^2/2lM$. A successful acceleration cycle requires the condition $l_i + s_i < l$ to be satisfied, where l_i is the distance between the ion and the first electrode at the instant of application of the voltage pulse. Then, during the time t the ion propagates in the absence of the field, covering the distance $s_0 = v_{i+1}t$. If the gap length satisfies $l < l_i + s_i + s_0 < 2l$, then after the application of a voltage pulse of opposite polarity, the ion again begins to be accelerated and we have $l_{i+1} = l_i + s_i + s_0 - l$.

The calculations show that ions of mass $M_0 = 10^6$ Da, entering this system with an initial energy of 10 kV, are accelerated to a potential of 127.3 kV at the exit if l_0 (the distance between the ion entering the accelerator and the input electrode at the instant of application of the first voltage pulse) is between 0 and 0.85 mm, which corresponds to a time width δt of the order of 0.6 μs for the initial ion
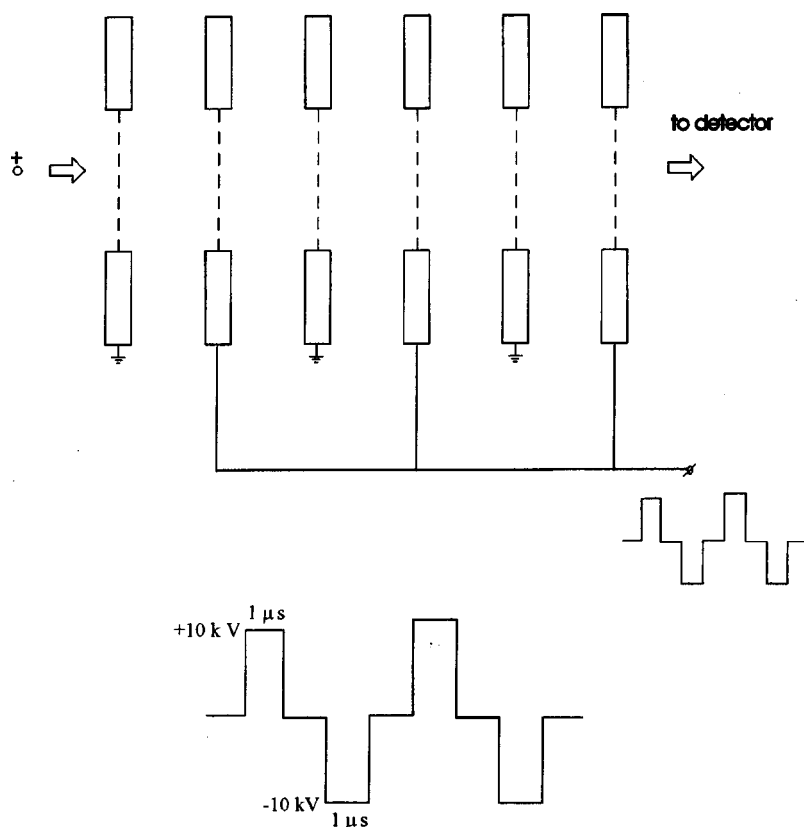
FIG. 1. Diagram illustrating the concept of an electrodynamic accelerator for heavy molecular ions.

packet. In this case, there is a large margin for possible variation of the initial ion energy δU and its mass δM; both these parameters can vary within a percentage of the initial value and despite this, the incoming ion will still be accelerated after passing through the accelerator. The energy acquired by the ion depends on its mass but these variations are small and are not significant. For this accelerator, for example, the energy varies between 126.6 keV for $M = 1.007 M_0$ and 127.9 keV for $M = 0.993 M_0$. Note that if the probability P of detection of such an ion is estimated using the empirical formula derived by Geno and MacFarlane[8] (since this formula was obtained for ions of far lower mass than the case $M = 10^6$ Da considered here, its validity must be checked experimentally): $P = 1 - \exp(-\gamma)$, with $\gamma = 2.58 \times 10^{-7} m \times \exp(2.31 \times 10^{-4} v)$, where m is the ion mass in daltons and its velocity v is in meters per second, we obtain the completely satisfactory value $P = 0.56$.

The proposed design was not specially optimized to obtain the highest possible values of δt, δU, and δM but these parameters may nevertheless be considered to be quite satisfactory. The results of a more detailed analysis of the operation of an electrodynamic accelerator, its optimization, and also its possible usage as a mass spectrometer and mass filter will be published separately. Depending on the acceleration required, the system can either be terminated after any number of accelerating gaps or the structure could be extended.

Thus, there is no doubt that the electrodynamic acceleration of very heavy molecular ions is possible in principle.

[1] M. Karas, D. Backmann, U. Bahr, and F. Hillenkampf, Int. J. Mass Spectrom. Ion Processes **78**, 53 (1987).

[2] K. Tang, S. L. Allman, and C. H. Chen, Rapid Commun. Mass Spectrom. **6**, 365 (1992).

[3] K. Tang, N. I. Taranenko, S. L. Allman *et al.*, Rapid Commun. Mass Spectrom. **8**, 727 (1994).

[4] R. C. Beavis and B. T. Chait, US Patent No. 5. 228, 644.

[5] C. H. Chen and PerSeptive Biosystems Inc., Framingham, MA (private communication).

[6] M. R. Aïnbund and B. V. Polenov, *Open Secondary Electron Multipliers and Their Application* [in Russian], Énergoatomizdat, Moscow (1981), 140 pp.

[7] R. J. Beuhler and L. Friedman, Int. J. Mass Spectrom. Ion Phys. **23**, 81 (1977).

[8] P. W. Geno and R. D. MacFarlane, Int. J. Mass Spectrom. Ion Processes **92**, 195 (1989).

[9] D. Twerenbold, J. L. Vuilleumier, D. Gerber *et al.*, Appl. Phys. Lett. **68**, 3503 (1996).

Induced of Zeeman coherence in an ensemble of cesium atoms interacting with a two-frequency (microwave+rf) magnetic field

N. A. Dovator

A. F. Ioffe Physicotechnical Institute, Russian Academy of Sciences, St. Petersburg
(Submitted December 30, 1997)
Pis'ma Zh. Tekh. Fiz. **24**, 89–93 (July 26, 1998)

Interference between Zeeman states corresponding to the forbidden magnetic-dipole transition $\Delta F=0$, $\Delta m_F=2$ is reported in connection with the simultaneous interaction of $6^2S_{1/2}$ cesium atoms with a resonant microwave field and an rf field which varies at twice the Larmor frequency and is directed perpendicular to a static magnetic field $H_0=0.2$ Oe.
© *1998 American Institute of Physics.* [S1063-7850(98)03507-1]

Studies of coherence effects in the interaction between radiation and matter are now attracting increased interest, mainly because the coherent coupling of atomic states leads to substantial changes in the macroscopic characteristics of a material. Such effects include ''coherent population trapping'' [1] and ''electromagnetically induced transparency.'' [2] It should be noted that in these studies and in others concerned with interference effects in ensembles with optically oriented atoms,[3–5] the coherent coupling of the atomic states took place as a result of a two-photon process in a three-level quantum system. In this case, each pair of interfering states (between which no direct transition took place) was coupled with a third state by interaction with one of two resonant electromagnetic fields belonging to the same frequency range (optical or microwave).

Here an experiment is described to observe coherence between the (4.4) and (4.2) Zeeman levels of $6^2S_{1/2}$ cesium atoms (between which the direct magnetic-dipole transition $\Delta F=0$, $\Delta m_F=2$ is forbidden) under conditions of a three-photon coherent process induced using two variable magnetic fields whose frequencies differ substantially (microwave and rf).

Figure 1a shows some of the ground-state levels of the cesium atoms which are coherently coupled as a result of the interaction of the microwave and rf magnetic fields with the ensemble of atoms. The apparatus is shown schematically in Fig. 1b.

The experiment was carried out as follows. Resonant, circularly polarized pump radiation directed parallel to a static magnetic field $H_0\simeq0.2$ Oe creates a nonequilibrium population of $6^2S_{1/2}$-cesium atomic levels. Microwave radiation from a 3 cm range microwave oscillator is passed through a waveguide and a rectangular horn antenna to a glass cell containing cesium vapor (at room temperature) and neon buffer gas. The orientation of the horn antenna is selected so that the direction of the magnetic induction vector of the microwave field forms an angle of 45° with that of the H_0 field.

As a result, the microwave field had magnetic field strength components with the polarizations σ (H_1^{σ}) and π (H_1^{π}). The frequency of the microwave field was tuned to the frequency of the $(4.4)\leftrightarrow(3.3)$ hyperfine structure transition which was monitored using the S_z signal for the optically oriented atoms.[6] The σ-polarized rf magnetic field (H_2^{σ}) was generated using a Helmholtz coil whose axis was perpendicular to H_0. The frequency of the rf generator used to supply the coil was close to twice the Larmor frequency $f_{\rm rf}=2f_0\equiv2\gamma/2\pi H_0$ ($\gamma/2\pi=350$ kHz/Oe). A transverse (to H_0) probe beam, linearly polarized in the direction orthogonal to H_0, was used to record the coherent superposition of (4.4) and (4.2) states which occurred in the experiments. The modulation of the absorption of the transverse light beam, which occurs at the frequency of the rf field under conditions
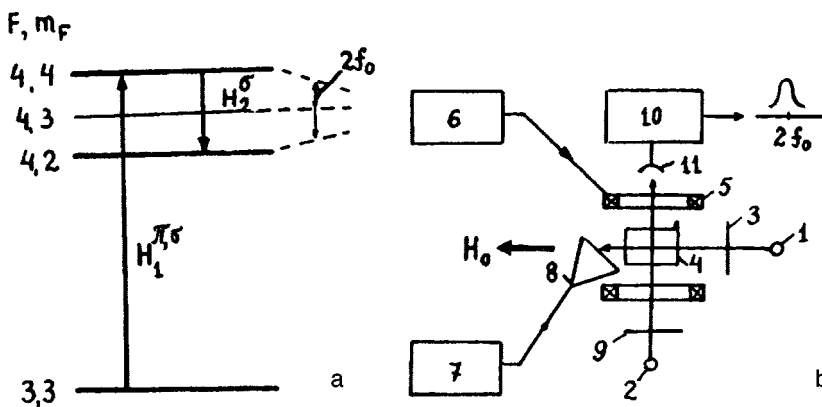

FIG. 1. a—Diagram of ground-state levels of cesium atoms assumed in the analysis of interaction between these atoms and a two-frequency (microwave+rf) magnetic field; b—block diagram of apparatus: *1,2*—cesium spectral lamp, *3*—circular polarizer, *4*—working cell, *5*—Helmholtz coil, *6*—rf generator, *7*—microwave generator, *8*—horn antenna, *9*—linear polarizer, *10*—band-pass amplifier, and *11*—photodiode.
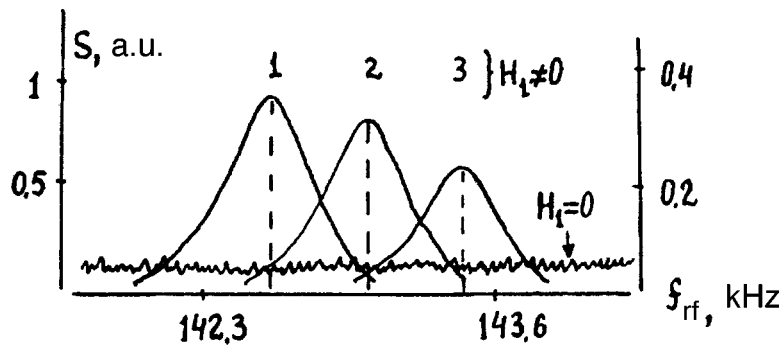
FIG. 2. Output voltage traces from band-pass amplifier obtained by sweeping the rf field frequency with the microwave field switched on ($H_1 \neq 0$, $P_{mw} \sim 10^{-1}$ W) and off ($H_1 = 0$). The scale on the right-hand ordinate refers to the case $H_1 = 0$. Curves *1–3* were obtained for $U = 20$, 15, and 8 V, respectively, where U is the output voltage of the rf generator.

of a three-photon coherent process and evidences the required Zeeman coherence, was detected using a photodiode positioned at the exit window of the cell (see Fig. 1b). The signal from the photodiode was then fed to a band-pass amplifier ($f_{bpa} = 2 f_0$, $\delta_{bpa} = 10$ kHz) and after amplitude detection, was recorded by an automatic plotter.

The Zeeman coherence signal was recorded as a resonant variation in the modulated absorption of cesium vapor as the frequency of the rf field was swept. Figure 2 shows traces of this signal obtained for different rf magnetic fields (the coil constant is $K = 2.5 \times 10^{-3}$ Oe/V).

The appearance of a coherence signal between the (4.4) and (4.2) Zeeman levels may be explained using the model of a three-level quantum system interacting with two monochromatic electromagnetic fields of different frequency (Fig. 1a). According to this model, the (4.4) level is coherently coupled with the (4.2) level via the third (3.3) level as a result of one-photon excitation of the $(3.3) \leftrightarrow (4.4)$ hyperfine structure transition using the H_1^{σ} component of the microwave field and two-photon excitation of the $(3.3) \leftrightarrow (4.2)$ neighboring hyperfine-structure transition by absorption of a π-polarized microwave quantum (H_1^{π}) and the simultaneous emission of a σ-polarized rf quantum (H_2^{σ}). In this case, the conditions for excitation of the magnetic-dipole transitions are satisfied ($\Delta F = 1$, $\Delta m_F = |1|$) both in terms of energy and magnetic quantum number.

Among the characteristic features of the observed Zeeman coherence signal we must include the drop in its resonance frequency when we increased the amplitude of the rf field. This frequency shift may arise because the σ-polarized rf magnetic field used experimentally, whose frequency was close to twice the Larmor frequency, is a nonresonant perturbation for each pair of neighboring Zeeman levels (with $\Delta F = 0$, $\Delta m_F = 1$). It was shown in Ref. 7 that such a perturbation should reduce the magnetic resonance frequency which can be seen clearly as the ''collapse'' of the Zeeman levels (dashed lines in Fig. 1a). As a result, the resonant frequency of the coherence signal $f_{res} = 2 f_0$ should also decrease, as was observed in these experiments.

[1] B. D. Agap'ev, M. B. Gornyĭ, B. G. Matisov *et al.*, Usp. Fiz. Nauk **163**, 1 (1993) [Phys. Usp. **36**, 763 (1993)].

[2] S. E. Harris, Phys. Today **50(7)**, 36 (1997).

[3] O. S. Vasyutinskiĭ, N. A. Dovator, and R. A. Zhitnikov, Zh. Éksp. Teor. Fiz. **72**, 928 (1977) [Sov. Phys. JETP **45**, 484 (1977)].

[4] N. A. Dovator and R. A. Zhitnikov, Zh. Éksp. Teor. Fiz. **77**, 505 (1979) [Sov. Phys. JETP **50**, 257 (1979)].

[5] E. B. Aleksandrov, A. B. Mamyrin, and Yu. S. Chidson, Zh. Éksp. Teor. Fiz. **72**(4), 1568 (1977) [Sov. Phys. JETP **45**, 823 (1977)].

[6] N. M. Pomerantsev, V. M. Ryzhkov, and G. V. Skrotskiĭ, *Physical Principles of Quantum Magnetometry* [in Russian], Nauka, Moscow (1972), 448 pp.

[7] L. N. Novikov and A. G. Malyshev, JETP Lett. **15**, 89 (1972).

Translated by R. M. Durham